SIMULATING VORTEX RING DYNAMICS FOR UAVS LANDING ON MOBILE PLATFORMS: A CFD APPROACH

by

Cortney Hahn

A thesis submitted to the faculty of
The University of North Carolina at Charlotte
in partial fulfillment of the requirements
for the degree of Master of Science in
Mechanical Engineering

Charlotte

2024

Approved by:

_____
Dr. Mesbah Uddin

_____
Dr. Artur Wolek

_____
Dr. Adit Misar

ABSTRACT

CORTNEY HAHN. Simulating Vortex Ring Dynamics for UAVs Landing on Mobile Platforms: A CFD Approach. (Under the direction of DR. MESBAH UDDIN)

The aerodynamic properties of unmanned aerial vehicles (UAVs) have become a central area of research for both civilian and military applications. Extensive data has been gathered on UAV systems and control mechanisms, particularly in relation to autonomous takeoff and landing operations involving ground vehicles (GVs). However, despite the development of advanced UAV systems and control strategies to ensure successful maneuvers, significant challenges persist due to the complex aerodynamic interactions that occur during a UAV's landing on a GV. One critical issue is the formation of the vortex ring state (VRS), which result from the interplay between three factors (i) rotor-induced airflow, (ii) the downwash from the UAV's main body, and (iii) its descent rate. These interactions generate large vortices that can cause turbulence and instability during landing. Current research on the VRS does not sufficiently address how these structures interact with GVs to create instability during landing operations. To address this gap, this study will conduct five UAV simulations at varying descent speeds, focusing on the aerodynamic behavior of the VRS during UAV landings on a GV. The objective is to analyze the characteristics of the VRS under different conditions, offering insights to enhance the precision and safety of UAV landing maneuvers.

DEDICATION

This work is dedicated to my incredible parents, Mark and Carda Hahn. Your unwavering support, boundless encouragement, and unconditional love have been the foundation of my strength and inspiration. Mom and Dad, your countless sacrifices and steadfast belief in me helped me chase my dreams with courage and determination. I am forever grateful for everything you have done to make this journey possible. For my beloved cat Cheetah, you were my constant motivation, inspiring me to give you the best life I possibly could for 19 wonderful years. To my friends, thank you for your constant encouragement, support, and companionship throughout this journey. I am truly blessed to have such remarkable people by my side, sharing in both the challenges and the triumphs.

ACKNOWLEDGEMENTS

I would like to express my deepest gratitude to my advisor, Dr. Uddin, for his invaluable guidance, unwavering support, and insightful expertise throughout the course of my Master's research. His mentorship has been instrumental in shaping my academic journey and helping me achieve this milestone. I am also sincerely thankful to Dr. Wolek and Dr. Misar for their assistance, constructive feedback, and encouragement during this process. Additionally, I would like to acknowledge Spencer Nichols, Collin Hague, Vincent Lee, Shishir Desai, Spencer Matthews, and Josh Cox for their help and contribution in brainstorming ideas and providing assistance throughout my thesis. Finally, I extend my heartfelt appreciation to the University of North Carolina at Charlotte for providing me with the resources, opportunities, and supportive academic environment that made this research possible.

TABLE OF CONTENTS

LIST OF TABLES

LIST OF FIGURES

LIST OF SYMBOLS

CFD An acronym for Computational Fluid Dynamics

A	Planiform area of the rotor hub
$C_{(.)}$	Coefficient of pressure, force and moment
C_{PM}	Pitch moment coefficients
C_{RM}	Roll moment coefficients
C_{YM}	Yaw moment coefficients
d and r	UAV rotor hub diameter and radius
H, L, W	Height, Length, and the Width the Ahmed body, respectively
i, and j	Indexing variables
k	Turbulence Kinetic Energy (TKE)
h^*	Distance of the UAV from GV top z_1 normalized by d;
p and P	Instantaneous and mean pressure, respectively
$Re_{.}$	Reynolds number; subscripts denote the length-scale used
s_{ij}, S_{ij}, s'_{ij}	Rate of strain tensor
T	Thrust
t	Time
u_i, U_i, u'_i	Velocity in the i direction
$V^*_{(.)}$	Normalized mean velocity in direction $_{(.)}$; also expressed as $VR_{(.)}$
v_d	Vertical descent velocity
v_h	Induced velocity generated by the rotor at hover
x, y, and z	Stream-wise, lateral and vertical directions
z_1	Distance of the UAV from the GV top or ground
Δt	Time step
δ_{ij}	Kronecker delta
ρ, μ	Fluid Dynamic Viscosity, and Density

ω	vorticity, and specific dissipation in SST Turbulence model
Ω	Rate of rotation tensor
σ_{ij}	Viscous stress tensor
ν_t	Turbulent Eddy Viscosity
Upper-case	Mean quantity
Lower-case	Instantaneous quantity
Subscripts:	
x, y, and z	Components in x, y and z, respectively
p, D, L, S	Pressure, drag, lift, and side-force coefficients, respectively
Superscripts:	
Prime ($'$)	Fluctuating quantity
$\overline{(.)}$	Time-averaged value of (.)

CHAPTER 1: INTRODUCTION

The interaction of unmanned aerial vehicles (UAVs) with ground vehicles (GVs) represents a critical and complex area of research, particularly in military applications where repeated UAV operations are essential. This collaboration can potentially revolutionize autonomous operations in defense and logistics, but it also introduces substantial technical challenges, especially during key maneuvers such as takeoff, landing, and hovering. A pivotal aspect of this integration is the autonomous takeoff and landing of UAVs on moving GVs, vital for tasks like docking onto recharging stations mounted on GVs. These maneuvers demand solutions to two primary challenges: the aerodynamic complexities of UAV-GV interactions and the precise detection of landing zones.

Aerodynamically, the landing process involves intricate flow interactions between the UAV and GV, which are further complicated by ground effects and variations in ambient wind conditions. These factors significantly influence lift, drag, and stability, making the maneuver inherently complex. While operating close to the ground can improve energy efficiency by reducing induced drag and enhancing lift-to-drag ratios, it can also destabilize multi-rotor UAVs, increasing the risk of accidents during landing. The dynamic environment created by a moving GV exacerbates these difficulties, introducing disturbances such as wind gusts. Furthermore, phenomena like the vortex ring state (VRS) present additional risks to UAV stability and control during these operations.

Vortex rings, or toroidal vortices, are fluid structures characterized by a closed loop of circulating fluid that form under specific conditions, such as when a fluid or gas is ejected through an orifice or interacts with another medium at a differing

Figure 1.1: Illustration of the Vortex Ring State around a helicopter [3].

velocity. A vortex ring's formation begins with the detachment of the boundary layer at the orifice edge, which rolls into a circular vortex due to shear forces and concentrated vorticity as shown in Figure 1.1. These phenomena are observed in both natural and experimental contexts, including smoke rings, volcanic eruptions, and laboratory setups using pistons or nozzles. The dynamics of vortex ring formation depend on factors such as the Reynolds number, stroke-to-diameter ratio, and velocity profile of the emitted fluid [9]. Experimental studies have shown that vortex rings achieve maximum circulation and energy efficiency at an optimal stroke ratio before separating from trailing jets. These self-sustaining structures exhibit poloidal motion, enabling them to travel long distances with minimal energy loss, making them a vital topic in fluid dynamics research and applications.

In rotorcraft aerodynamics, vortex ring dynamics play a critical role in the phenomenon known as the VRS. The VRS occurs when rotor airflow interacts with the surrounding air during descent, creating turbulent conditions that compromise lift and control effectiveness. This phenomenon has been implicated in numerous UAV and helicopter crashes, as documented by reports from the Federal Aviation Administration (FAA) [10] and military statistics. By understanding the underlying principles

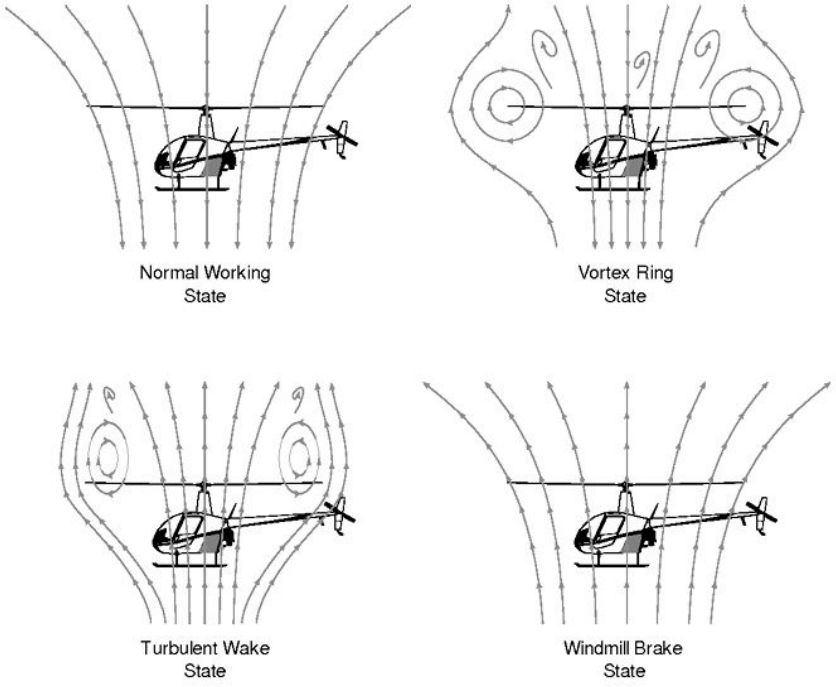

Figure 1.2: Streamline patterns of helicopter aerodynamics across four axial configurations [4]; reproduced from the Master's thesis of H. Van Vyve [5].

of vortex rings, researchers can better analyze and mitigate the risks posed by the VRS in UAV operations.

When operating a rotorcraft, the thrust produces a downward airflow known as downwash. When the rotor descends in alignment with this induced flow, the downwash interacts with the upward flow created by the descent motion. As described by Mullen and Bernini [11], near the rotor disk, the flow is dominated by rotor-induced velocity, while the surrounding flow moves upward. The VRS occurs when the magnitude of this upward flow becomes comparable to that of the rotor-induced velocity. In such conditions, wake vorticity accumulates near the rotor plane instead of being dispersed, forming a toroidal, doughnut-shaped ring of recirculating airflow as shown in Figure 1.2. This results in turbulent and unsteady flow dynamics characterized by thrust fluctuation, torque oscillation, increased vibration, and reduced control effectiveness.

Entry into the VRS can have severe consequences, including an increased rate of descent and changes in the rolling moments. As noted by Mullen and Bernini [11], these effects may also result in aerodynamic losses, necessitating greater power to sustain flight. Most helicopters lack sufficient power reserves at low airspeeds, even with maximum rotor output, to respond to entering the VRS. As a result, helicopters continue descending rapidly a phenomenon commonly referred to as "settling with power." For an in-depth exploration of VRS dynamics and mitigation strategies, see the comprehensive analyses provided in [12] and [13]. Hoffmann et al. [1] further investigated quadrotor dynamics and control under external disturbances. Their study identified three primary fluid flow regimes around unmanned aerial vehicles (UAVs) operating near vertical descent conditions: Normal Working State (NWS), Vortex Ring State (VRS), and Windmill Brake State (WBS). Expanding on this work, Bangura and Mahony [2] developed a hybrid dynamic model based on momentum theory to address transitions between normal flight and VRS. Using velocity ratios, their model incorporated additional aerodynamic phenomena, such as the Turbulent Wake State (TWS) and Ground Effect State (GES).

1.1 Motivation

The motivation for this research arises from the pressing need to deepen our understanding of and develop strategies to mitigate the aerodynamic complexities associated with the VRS during UAV operations near GVs. The VRS has been a persistent and well-documented challenge in rotorcraft engineering since its first identification by George de Bothezat in 1922. Despite significant advancements in UAV design and control the subtle onset of VRS and its rapid destabilizing effects continues to pose challenges. This issue becomes particularly critical during landing maneuvers, where the interaction between UAV-induced downwash and the surfaces of GVs can intensify turbulence and exacerbate the instability created by the VRS. While computational fluid dynamics (CFD) has been widely applied to study hovering, ascending, and de-

scending flight scenarios, research addressing the aerodynamic interactions between UAVs and GVs during landing remains scarce. The lack of comprehensive studies on these interactions not only limits our ability to understand the formation of the VRS in such contexts but also hinders efforts to generate sufficient data for creating predictive models. Current research predominantly emphasizes systems-level control and stabilization approaches, often overlooking the intricate fluid dynamics underlying these phenomena. This study seeks to address these gaps by investigating how UAV descent speed influences the formation of the VRS during landings onto stationary GVs. By focusing on the interplay between UAV aerodynamics and GV surfaces, this research aims to provide valuable insights into both the behavior of the VRS and its mitigation contributing to safer and more reliable UAV operations in complex environments.

1.2 Objective

This research focuses on understanding the aerodynamic interactions between unmanned aerial vehicles (UAVs) and ground vehicles (GVs) during constant-speed descents. The study emphasizes the impact of landing speed on the formation and behavior of the vortex ring state (VRS) and explores how these dynamics influence UAV stability, wake behavior, and overall aerodynamic performance. The findings aim to inform future UAV design and operational improvements, especially in scenarios involving proximity to GVs.

The objectives of this thesis are:

- Conduct computational simulations at descent speeds of 2, 4, 6, 8, and 10 m/s.
- Examine effects on UAV stability, wake dynamics, and aerodynamic performance.
- Observe the impact of varying descent velocities on VRS onset and severity.

- Examine the aerodynamic interactions between UAV downwash and GV surfaces.

1.3 Layout and Organization

This thesis is structured to address the research objectives, providing a comprehensive investigation into the aerodynamic interactions between UAVs and GVs during constant-speed descents, focusing on the formation of the VRS and its implications. The introduction outlines the importance of studying these interactions, emphasizing the critical role of the VRS on the stability and performance of a UAV during landing phases. This thesis highlights the broader significance of addressing the aerodynamic challenges for advancing UAV-GV integration in military and logistical applications, where operational safety and efficiency are paramount. The research objectives and scope are clearly defined to frame the study.

The literature review delves into existing research on the VRS and UAV aerodynamics. It begins by defining the VRS, discussing its characteristics, onset conditions, and mitigation strategies as explored in prior studies. The review also examines UAV performance during descent scenarios, focusing on isolated UAV behavior and flow dynamics in proximity to ground vehicles. Additionally, it surveys studies on wake dynamics, turbulence, and aerodynamic coupling between UAVs and GVs, identifying key gaps in the current body of knowledge regarding UAV-GV interactions at varying descent speeds.

The methodology section details the computational approach used to investigate these aerodynamic interactions. The study employs Computational Fluid Dynamics (CFD) simulations based on the Navier-Stokes equations to model fluid flow dynamics, capturing critical aspects such as the pressure distribution, velocity fields, and turbulence effects. Improved Delayed Detached Eddy Simulation (IDDES) is used to resolve turbulence scales in wake regions with high accuracy. The geometry of the UAV and GV is described in detail, along with the computational domain dimensions

designed to effectively capture downwash effects and ground interactions. To capture the fluid flow a mesh is generated, with a combination of structured and unstructured grids, with refinement zones near UAV rotors and GV surfaces to ensure accurate resolution of flow features. A grid independence study validates mesh quality for reliable results. The simulations are conducted at descent speeds of 2, 4, 6, 8, and 10 m/s across varying non-dimensional height parameters ($h^* = z_1/d$, where z_1 is the distance from the bottom of the UAV to the top of the GV, and d is the diameter of the rotor) to evaluate the effects at different relative altitudes.

The results section presents a detailed analysis of the VRS formation across different descent speeds, highlighting onset conditions and severity at each speed. It examines how variations in h^* influence the behavior and wake dynamics of the VRS. Furthermore, the section explores aerodynamic interactions between UAV-induced downwash and GV surfaces, analyzing their impact on the GV flow field characteristics and UAV stability during landing phases. These findings provide valuable insights into the interplay between descent velocity, relative altitude, and aerodynamic performance.

The discussion interprets these results within the broader context of UAV-GV aerodynamic integration. It evaluates how descent speed affects operational safety and efficiency while drawing implications for rotorcraft design optimizations such as rotor configurations. Recommendations are made for improving control algorithms to mitigate turbulence effects during landing operations. The discussion also emphasizes the potential for these findings to inform future design strategies aimed at enhancing stability and minimizing turbulence during critical phases of UAV operation.

The conclusion summarizes the key findings regarding the VRS behavior and UAV-GV interactions while highlighting the contributions of this research to advancing UAV design and operational strategies for autonomous systems. Suggestions for future research include experimental validation of simulation results and exploration

of additional operational scenarios involving complex terrains or multi-UAV systems. Addressing these aerodynamic challenges is essential for enhancing UAV-GV integration while ensuring safety and efficiency. By overcoming these obstacles, this work aims to unlock new capabilities in autonomous operations for military logistics and other applications, paving the way for more reliable UAV systems through improved designs, control strategies, and operational guidelines.

CHAPTER 2: LITERATURE REVIEW

The integration of unmanned aerial vehicles (UAVs) with ground vehicles (GVs) presents significant potential for advancing autonomous operations in defense and logistics. However, this collaboration introduces substantial technical challenges, particularly during critical maneuvers such as takeoff and landing. A key issue lies in the aerodynamic complexities of UAV-GV interactions, which are further complicated by phenomena like the vortex ring state (VRS). The VRS destabilizes rotorcraft during descent by creating turbulent airflow conditions that compromise lift and control effectiveness. This challenge is exacerbated during UAV landings on GVs due to intensified turbulence caused by UAV downwash interacting with GV surfaces. Despite advancements in UAV design and control systems, the subtle onset and rapid destabilizing effects of the VRS remain a persistent obstacle, particularly in dynamic environments. Addressing these aerodynamic challenges is critical for enhancing the reliability and safety of UAV operations [14].

2.1 Vortex Ring State (VRS)

The vortex ring state was first observed in 1922 during test flights of an innovative rotorcraft known as the *flying octopus*. This phenomenon occurs when a rotor descends into its own downwash, creating a doughnut-shaped ring of recirculating airflow near the rotor plane. As described by Mullen and Bernini [11], the VRS leads to highly turbulent conditions characterized by thrust fluctuations, torque oscillations, increased vibrations, and loss of control effectiveness. The upward flow caused by descent motion interacts with the rotor-induced downward flow, resulting in wake vorticity accumulation near the rotor disk. This interaction can cause rapid

descent rates and instability when helicopters lack sufficient power to counteract the aerodynamic losses.

2.2 Aerodynamic Challenges in UAV Descent

McQuaid et al. [14] conducted a study using computational fluid dynamics (CFD) simulations with OpenFOAM to identify early signs of the VRS in quadrotor drones. Their findings highlighted thrust degradation, wake breakdown, and oscillations at specific descent velocities as indicators of the VRS's onset. They proposed a novel detection method using differential pressure measurements around the quadrotor fuselage, offering potential for early warning systems.

Similarly, Rimša and Liugas [15] investigated the VRS's formation around helicopter main rotors using CFD simulations with Ansys CFX software. Their research provided insights into critical velocity combinations and descent angles conducive to the VRS's onset. Wang et al. [16] further explored VRS dynamics in quadcopters, revealing that these vehicles enter the VRS at lower descent speeds compared to single rotors but experience less severe lift loss due to aerodynamic interference between rotors.

Throneberry et al. [17] analyzed wake characteristics of multi-rotor UAVs using wind tunnel experiments and particle image velocimetry (PIV). Their study identified critical transition points in descending flight where wake behavior shifts significantly, providing valuable data for optimizing sensor placement to minimize disturbances.

2.3 Coaxial Rotor Systems

Coaxial rotor systems have been proposed as a solution to enhance UAV performance under challenging conditions such as high-altitude descents. Sun et al. [18] developed a novel power management pipeline for coaxial rotor UAVs that enabled controlled vertical descent speeds up to 8 m/s surpassing the typical 3 m/s limit constrained by the VRS.

Marshall et al. [19] investigated NASA's Dragonfly rotorcraft lander designed for Titan exploration under the VRS conditions. They demonstrated that coaxial rotors are more resistant to the VRS onset compared to single rotors but experience larger thrust reductions once in the VRS due to rotor-rotor interactions.

Cornelius et al. [20, 21] presented efficient CFD methodologies for analyzing coaxial rotor systems in hover and descent scenarios. Their hybrid Blade Element Momentum Theory Unsteady Reynolds Averaged Navier-Stokes (BEMT-URANS) method provided accurate performance predictions at lower computational costs compared to high-fidelity CFD methods.

2.4 CFD Methodologies for UAV Analysis

CFD methodologies have been instrumental in advancing our understanding of UAV aerodynamics under various flight conditions. Paz et al. [22] evaluated two CFD approaches: Multiple Reference Frames (MRF) and sliding mesh-for simulating quadcopter aerodynamics in ground effect scenarios. While the MRF model was computationally less expensive, it underestimated thrust magnitude compared to the sliding mesh method, which provided more accurate results for detailed analyses.

Cornelius et al.'s work on coaxial rotors also highlighted the advantages of hybrid CFD approaches for performance prediction across diverse flight regimes [21]. These methodologies enable efficient analysis while maintaining high fidelity, making them suitable for engineering applications in urban air mobility and other multirotor configurations.

Hoffmann et al. [1] conducted a comprehensive study on quadrotor dynamics and control mechanisms under external disturbances, identifying three primary fluid flow modes around UAVs operating near vertical attack regions: Normal Working State (NWS), Vortex Ring State (VRS), and Windmill Brake State (WBS). These modes are summarized in Table 2.1. Building on this foundational research, Bangura and Mahony [2] addressed key challenges in modeling transitions between normal flight

and the VRS. They developed a hybrid dynamic model based on momentum theory, which computed both static and translational lift for each rotor. This model extended Hoffmann's framework by incorporating additional aerodynamic phenomena, including the Turbulent Wake State (TWS) and Ground Effect State (GES). The phases of these states are also detailed in Table 2.1 in which v_d represents the vertical descent velocity and v_h is the induced velocity generated by the rotor at hover conditions, and r is the radiaus of the rotor ($r \equiv 0.5d$)

Table 2.1: Five Distinct Fluid Flow Modes Around UAVs [1, 2].

Descent Phases	Equations
Normal Working State (NWS)	$\frac{r}{z} > 0.1,\ -v_d < \frac{1}{2}v_h$
Vortex Ring State (VRS)	$-\frac{1}{2} \leq -v_d < v_h$
Turbulent Wake State (TWS)	$-v_h \leq -v_d < 2v_h$
Windmill Brake State (WBS)	$-v_d \geq 2v_h$
Ground Effect State (GES)	$\frac{r}{z} \leq 0.1$

Bangura and Mahony [2] introduced velocity ratio ranges, v_d/v_h, to define the various aerodynamic states in an alternative way. By developing a hybrid dynamic model that accounts for diverse rotor operating states particularly emphasizing transitions between normal flight and the VRS they expanded Hoffmann's original framework to include additional states such as TWS and GES. These states are mathematically expressed as functions of rotor radius (r) and vertical distance from the ground (z).

In both Hoffmann's [1] and Bangura and Mahony's [2] studies, the induced velocity (v_h) was calculated using empirical relationships derived from momentum integral theory. With T_h representing thrust during hover and A denoting the planiform area of the rotor hub, this relationship can be expressed as:

$$v_h = \sqrt{\frac{T_h}{2\rho A}} \tag{2.1}$$

Simulations incorporating both Hoffmann's and Bangura-Mahony's methodologies were conducted to evaluate the induced velocities of UAV rotors positioned above

ground vehicles (GVs). These simulations provided critical insights into mass flow rates during the initialization phases before reaching steady-state conditions. To further investigate these dynamics, computational fluid dynamics (CFD) frameworks were employed to analyze UAV-GV interactions in greater detail.

Building on this foundation, Talaeizadeh [6] explored fluid flow phenomena such as the Vortex Ring State (VRS) and Windmill-Brake State (WBS) in quadcopters, which are crucial for ensuring safe descent trajectories. The VRS is marked by significant thrust fluctuations that lead to instability, while WBS involves high fluctuations caused by airflow-induced autorotation. Unlike helicopters, quadcopters must avoid both regions due to their rigid blade mechanisms and lack of pitch control, making these phenomena particularly hazardous.

To address these challenges, the study combined theoretical modeling with wind tunnel experiments to identify unstable regions in velocity space. A simplified velocity constraint model was proposed to define safe operational boundaries for quadcopters. Using this model, time-optimal descent trajectories were designed to avoid the VRS and WBS while maximizing descent speed, as illustrated in Figure 2.1. Numerical methods such as GPOPS-II were applied to compute these trajectories in both 2D and 3D spaces, resulting in maneuvers like oblique paths, zigzag patterns, and helix-type trajectories.

CFD applications have been extensively employed to address vortex ring structures, beginning with foundational studies of the phenomenon and advancing toward innovative mitigation techniques. Among these methods, wind tunnel testing and CFD simulations have become prominent tools for investigating such aerodynamic challenges. While significant progress has been made in developing systems and control strategies for UAV maneuvers, fluid dynamics aspects such as evaluating the VRS through wind tunnel experiments or CFD simulations remain relatively underexplored by manufacturers. Current CFD studies predominantly focus on isolated

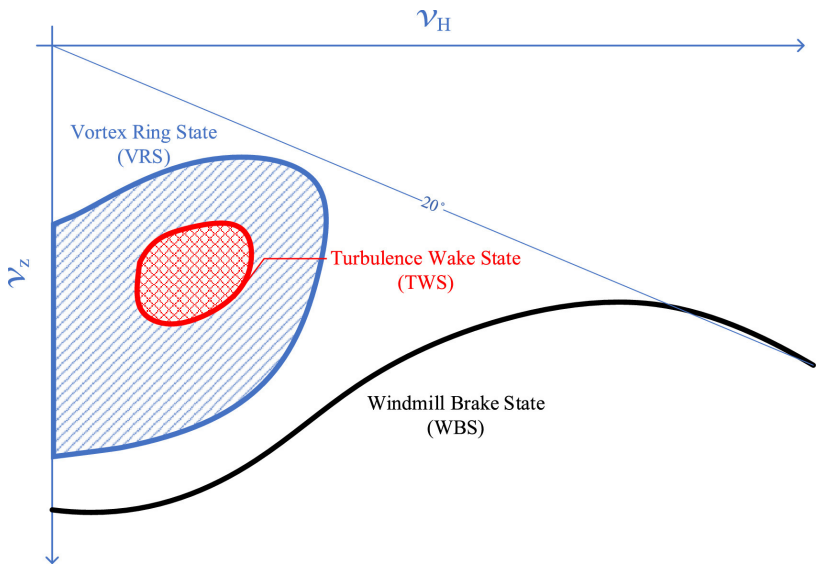

Figure 2.1: Velocity of Descent vs the non-dimensional height [6].

UAVs in hover or near-ground stability scenarios [23, 22, 24, 25]. Similarly, while there is substantial research on GV fluid flow interactions [26, 27, 28], investigations into UAV GV aerodynamic interactions are limited. Recent efforts have sought to validate findings from individual UAV and GV studies against emerging data on UAV GV interactions, highlighting the need for further research in this domain [29].

CHAPTER 3: METHODOLOGY

Computational Fluid Dynamics has become an indispensable tool in the design and optimization of UAVs and GVs, offering numerous benefits that enhance their aerodynamic performance, reduce costs, and accelerate development timelines. For UAVs, CFD enables designers to simulate and analyze complex aerodynamic phenomena such as lift, drag, and flow separation, which are critical for optimizing flight efficiency, stability, and maneuverability. By using CFD, engineers can explore a wide range of design configurations in a virtual environment, reducing the reliance on costly and time-intensive physical prototypes. For instance, CFD simulations allow UAV developers to refine wing profiles, adjust propulsion system placements, and minimize drag to improve fuel efficiency and extend flight range. Similarly, for GVs, CFD has revolutionized how vehicles are designed by enabling precise analysis of aerodynamic properties such as drag reduction and airflow management. By simulating airflow around vehicle components like wheels, mirrors, and underbodies, engineers can identify areas of high drag and implement design changes to improve fuel efficiency and overall performance. CFD is especially valuable for optimizing the external aerodynamics of ground vehicles to reduce energy consumption and environmental impact.

However, it is important to recognize that no single approach can fully capture all the physical phenomena involved in aerodynamic analysis. For instance, Direct Numerical Simulation (DNS), which resolves all turbulence scales without modeling assumptions, is not a viable option due to its immense computational demands. Consequently, alternative turbulence modeling techniques are employed. These methods range from Reynolds-Averaged Navier-Stokes (RANS) models, which are computationally efficient but rely on significant turbulence closure approximations, to Large

Eddy Simulation (LES), which offers higher fidelity by resolving larger turbulent structures at the expense of substantially increased computational cost. Building on this foundation, the pre-processing phase for Computational Fluid Dynamics (CFD) simulations involves formulating the governing equations for fluid flow. These equations are the Navier-Stokes equations, which are expressed in equations (3.1) and (3.2). The variables t represent time while u_i, p, ρ, and σ_{ij} stand for the instantaneous (time-variant) values of the velocity in the x_i direction, pressure, fluid density, and fluid viscous stress tensor, respectively.

$$\frac{\partial u_i}{\partial x_i} = 0 \tag{3.1}$$

$$\frac{\partial u_i}{\partial t} + u_j \frac{\partial u_i}{\partial x_j} = -\frac{1}{\rho}\frac{\partial p}{\partial x_i} + \frac{\partial \sigma_{ij}}{\partial x_j} \tag{3.2}$$

The viscous stress tensor, as referenced in equation (3.2), necessitates the use of the instantaneous rate of strain, which is defined as:

$$s_{ij} = \frac{1}{2}\left(\frac{\partial u_i}{\partial x_j} + \frac{\partial u_j}{\partial x_i}\right) \tag{3.3}$$

The RANS approach is one of the most widely used methods for this purpose, as it simplifies the problem by averaging the flow variables over time, thereby modeling all turbulence scales. However, while RANS is computationally efficient and effective for steady-state flows, it struggles to accurately capture unsteady and transient phenomena, such as vortex shedding and wake interactions, which are critical in UAV-GV aerodynamic studies. To address these limitations, Unsteady Reynolds-Averaged Navier-Stokes (URANS) was developed as an extension of RANS. Unlike RANS, URANS incorporates time-dependent terms into the equations, allowing it to capture unsteady flow features with greater fidelity. This makes URANS particularly advantageous for simulating boundary layer dynamics and transient flow structures

in CFD scenarios involving UAVs interacting with GVs. In such cases, where complex flow separations and wake interactions occur near surfaces like the Ahmed body or UAV components, URANS provides a more accurate representation of the evolving boundary layer behavior compared to traditional RANS. By resolving larger-scale unsteady motions while maintaining computational efficiency, URANS serves as a bridge between RANS and higher-fidelity methods like Large Eddy Simulation (LES), offering a practical balance for capturing critical aerodynamic phenomena in UAV-GV interaction studies.

The Unsteady Reynolds-Averaged Navier-Stokes (URANS) equations are derived by applying Reynolds decomposition to the time-dependent velocity field, u_i. This process involves separating u_i into its mean component, U_i, and a fluctuating component, u_i', such that $u_i = U_i + u_i'$. Subsequently, ensemble averaging is performed on the original Navier-Stokes equations, as outlined in Equations (3.1) and (3.2).

The resulting URANS equations, presented in Equations (3.4), and (3.5), provide a statistical description of turbulent flow. Instead of relying on the instantaneous velocity field, $u_i(x,t)$, and instantaneous strain rate field, $s_{ij}(x,t)$, the URANS formulation characterizes the flow in terms of the mean velocity field, $U_i(x,t)$, and the mean strain rate field, $S_{ij}(x,t)$.

$$\frac{\partial U_i}{\partial x_i} = 0 \tag{3.4}$$

$$\frac{\partial U_i}{\partial t} + \frac{\partial U_j U_i}{\partial x_j} = -\frac{1}{\rho}\frac{\partial P}{\partial x_i} + \frac{\partial}{\partial x_j}\left(2\mu S_{ij} - \rho\overline{u_i' u_j'}\right) \tag{3.5}$$

The momentum equation for URANS is given in Equation (3.5). It illustrates the turbulence closure problem, where four equations must be solved for ten unknowns. These unknowns include pressure, three velocity components, and six independent components of the variance tensor $\overline{u_i' u_j'}$, referred to as the Reynolds stress tensor.

This tensor emerges from the Reynolds averaging process applied to the non-linear term $u_i U_j$ in the Navier-Stokes momentum equation. A common approach to address this is the Boussinesq eddy viscosity hypothesis, which relates turbulent stresses to the mean rate of strain using the viscous stress analogy and through a flow variable known as turbulent eddy viscosity (v_t). This relationship is expressed as:

$$\overline{u_i' u_j'} = \frac{2}{3} k \delta_{ij} - 2\nu_t S_{ij} \tag{3.6}$$

In this context, k represents the turbulence kinetic energy per unit mass, defined as $k \equiv \frac{1}{2}\overline{u_i' u_i'}$, while δ_{ij} denotes the Kronecker delta, where $\delta_{ij} = 1$ for $i = j$, and $\delta_{ij} = 0$ for $i \neq j$. Turbulence models differ primarily in how the eddy viscosity (ν_t) is formulated, how turbulence quantities are linked to the eddy viscosity, and the specific transport equations and constitutive relations used to determine ν_t.

For this study, the Shear Stress Transport (SST) k-ω turbulence model, referred to as SST hereafter, is utilized. This approach is described below; however, readers seeking a detailed analysis of alternative modeling techniques for ground vehicle external aerodynamics are encouraged to refer to Zhang et al. [30]. The SST model incorporates two additional transport equations: one for turbulence kinetic energy (k) and another for the specific turbulent dissipation rate (ω).

The SST model was developed by Menter [31, 32] to address the well-documented sensitivity of the standard k-ω model by Wilcox [33, 34] to free-stream or inlet conditions. This limitation is mitigated by blending the k-ε model proposed by Launder et al. [35] in the far-field with the k-ω model in near-wall regions. The governing transport equations and constitutive algebraic relations for the SST model are presented below.

$$\nu_t = \frac{a_1 k}{\max\left(a_1\omega, SF_2\right)} \tag{3.7}$$

$$U_j\frac{\partial k}{\partial x_j} = P_k - \beta^* k\omega + \frac{\partial}{\partial x_j}\left[\left(\nu + \sigma_k\nu_t\right)\frac{\partial k}{\partial x_j}\right] \tag{3.8}$$

$$U_j\frac{\partial \omega}{\partial x_j} = \gamma S^2 - \beta\omega^2 + \frac{\partial}{\partial x_j}\left[\left(\nu + \sigma_\omega\nu_t\right)\frac{\partial \omega}{\partial x_j}\right] + 2\left(1-F_1\right)\sigma_{\omega 2}\frac{1}{\omega}\frac{\partial k}{\partial x_i}\frac{\partial \omega}{\partial x_i} \tag{3.9}$$

$$F_1 = \tanh\left\{\left\{\min\left[\max\left(\frac{\sqrt{k}}{0.09\omega d}, \frac{500\nu}{d^2\omega}\right), \frac{2k}{CD_{k\omega}d^2}\right]\right\}^4\right\} \tag{3.10}$$

$$F_2 = \tanh\left[\left\{\max\left(\frac{2\sqrt{k}}{\beta^*\omega d}, \frac{500\nu}{d^2\omega}\right)\right\}^2\right] \tag{3.11}$$

$$CD_{k\omega} = \max\left(\frac{1}{\omega}\frac{\partial k}{\partial x_i}\frac{\partial \omega}{\partial x_i}, 10^{-20}\right) \tag{3.12}$$

$$\gamma = F_1\gamma_1 + \left(1-F_1\right)\gamma_2 \tag{3.13}$$

$$\gamma_1 = \frac{\beta_1}{\beta^*} - \sigma_{\omega 1}\frac{\kappa^2}{\sqrt{\beta^*}} \tag{3.14}$$

$$\gamma_2 = \frac{\beta_2}{\beta^*} - \sigma_{\omega 2}\frac{\kappa^2}{\sqrt{\beta^*}} \tag{3.15}$$

In the equations above, α, β, β^*, σ_k, σ_ω, and $\sigma_{\omega 2}$ represent turbulence model closure coefficients. The blending functions F_1 and F_2 are used to transition between the near-wall region and the far-field. Specifically, F_1 blends the near-wall closure coefficient, associated with the k-ω model, with its far-field counterpart from the k-ε model. This blending process determines a closure coefficient, denoted as ϕ, by combining its k-ω value (ϕ_1) and its k-ε value (ϕ_2) using the relation: $\phi = F_1\phi_1 + (1-F_1)\phi_2$.

Existing studies highlight that the Reynolds-Averaged Navier-Stokes (RANS) approach often struggles to accurately predict separated flows dominated by a wide range of turbulent scales. This limitation has led to the increasing preference for scale-resolving simulation (SRS) techniques, such as Large Eddy Simulation (LES). LES resolves the larger turbulent scales directly while modeling only the smaller, sub-

grid scale (SGS) motions. The methodology is based on the premise that small-scale turbulence contributes less significantly to Reynolds stresses compared to large-scale eddies. These smaller scales are typically assumed to be isotropic, allowing them to be modeled with minimal loss of accuracy. As a result, LES separates turbulence into resolved large scales and modeled SGS components.

However, despite its advantages, LES remains computationally prohibitive for most automotive external aerodynamics applications. A more feasible alternative is the Detached Eddy Simulation (DES), introduced by Spalart and colleagues [36]. DES is a hybrid approach that combines RANS and LES methodologies: RANS is applied within boundary layers, while LES is used in regions of unsteady separated flow. This hybridization significantly reduces computational costs since RANS does not require the fine isotropic mesh resolution needed by LES in boundary layers.

The transition between RANS and LES regions in DES is determined for each computational cell by comparing the effective turbulent length scale, l_T ($l_T \equiv \sqrt{k}/\omega$), with the local finite-difference cell size, l_{LES} ($l_{\text{LES}} \equiv C_{\text{DES}}\Delta_{\text{DES}}$). Here, C_{DES} is a constant, and Δ_{DES} represents the filter width based on local mesh resolution. RANS is applied wherever $l_T < l_{\text{LES}}$.

One drawback of DES is the occurrence of artificial separations, known as Grid-Induced Separation (GIS). GIS arises when the cell edge length within the boundary layer falls below a critical threshold. To address this issue, a shielding mechanism can be introduced to protect the RANS model from DES activation near wall boundary layers. This shielding involves a parameter that depends on eddy viscosity and wall distance [41]. The resulting modified approach is called Delayed Detached Eddy Simulation (DDES).

The Improved Delayed Detached Eddy Simulation (IDDES) bridges the gap between RANS and DES by offering a hybrid approach that leverages the strengths of both methods. IDDES applies Unsteady Reynolds-Averaged Navier-Stokes (URANS)

in regions of attached boundary-layer flow to minimize computational costs, while transitioning to Large Eddy Simulation (LES) in areas of separated or highly turbulent flows where greater accuracy is essential. This adaptability makes IDDES particularly well-suited for complex aerodynamic problems, such as those encountered in ground vehicles or unmanned aerial vehicles (UAVs), where flow characteristics can vary significantly across the geometry.

In this study, IDDES is utilized due to its enhanced capabilities over Delayed Detached Eddy Simulation (DDES). Key improvements include: (1) reducing excessive dissipation caused by premature switching from RANS to LES, and (2) enabling Wall-Modeled LES (WMLES) for efficient resolution of wall-bounded flows [42, 43]. While these enhancements introduce additional complexity into the IDDES formulation, they significantly improve its versatility and applicability for high Reynolds number flows across a wide range of aerodynamic scenarios.

For brevity, this paper includes only the equations relevant to calculating the specific dissipation rate and C_{DES}. By leveraging the efficiency of RANS and the detailed resolution of LES, IDDES provides a balanced and practical method for simulating turbulent flows with improved accuracy compared to traditional RANS models and reduced computational cost compared to full LES. As shown on Equation (3.16) and (3.17) is the IDDES-SST model for the specific dissipation rate.

$$\widetilde{\omega} = \frac{\sqrt{k}}{l_{\mathrm{Hybrid}}\ \beta^{*};\ f_{\beta^{*}}} \tag{3.16}$$

$$C_{\mathrm{DES}} = C_{\mathrm{DES},k-\omega}\ F_1 \quad + \quad C_{\mathrm{DES},k-\varepsilon}\ (1 - F_1) \tag{3.17}$$

In the equations above, $f_{\beta^{*}}$ and l_{Hybrid} represent the free-shear modification factor and the hybrid length scale, respectively. These quantities are calculated using the effective turbulent length scale and local grid size, incorporating a blending function

and an elevating function to ensure smooth transitions between regions. The constants $C_{\mathrm{DES},k\text{-}\varepsilon} = 0.61$ and $C_{\mathrm{DES},k\text{-}\omega} = 0.78$ correspond to the values of C_{DES} in the k-ε and k-ω regions of the SST-RANS model, respectively.

3.1 Geometry and Domain

Given the lack of access to a digital model commonly referred to as the CAD geometry or design data and experimental aerodynamic test results for an actual military vehicle, an idealized vehicle geometry was selected for this research. Specifically, the Ahmed body was chosen as the GV model. This decision is supported by the extensive availability of computational and experimental data on the Ahmed body in existing literature, which spans multiple studies. The Ahmed body is a simplified representation of a ground vehicle that has become a standard reference geometry in external aerodynamics research. It is widely utilized for validating and calibrating both wind tunnel experiments and CFD methodologies due to its well documented aerodynamic characteristics.

In studies related to ground vehicle aerodynamics, the Ahmed body serves as an effective surrogate for real-world vehicles and in such cases for military applications would be a Fed Alpha 3.1. This would enable researchers to explore fundamental flow behaviors such as separation, wake dynamics, and drag prediction under controlled conditions.

Its geometric simplicity facilitates CFD modeling while still capturing key aerodynamic phenomena relevant to practical applications. Thus, its adoption in this study ensures that the validation process is robust and grounded in established benchmarks from prior research. The dimensions of the Ahmed body are as follows: 1044 mm in length (streamwise or forward-motion direction), 389 mm in width (lateral or spanwise direction), and 288 mm in height (vertical or ground-normal direction). Its geometry is typically classified based on the rear slant angle, with experimental and computational data available for angles of 15°, 20°, 25°, 30°, 35°, and 40°[26, 27, 28].

Figure 3.1: Army Fed Alpha Vehicle [7]. Image Credit: MOTORTREND, (`https://www.motortrend.com/news/163-news0603-fed-alpha/`), accessed on: 5 December, 2024.

For this study, a 35°slant angle Ahmed body was selected due to its geometric similarity to the High Mobility Multipurpose Wheeled Vehicle (HMMWV, commonly known as the Humvee), which is extensively used by military forces. However, since the dimensions of a Humvee are approximately 4.4 times larger than those of an Ahmed body, a scaled-up version of the Ahmed body enlarged by a factor of 4.4 was utilized as the representative GV model for this analysis. Figure 3.2 illustrates this scaled-up geometry.

In the absence of CAD geometry data or experimental test data for a military UAV, alternative approaches must be adopted for aerodynamic analysis. To address this limitation, a drone model with readily available CAD and aerodynamic data from prior research was utilized. This model, referred to as the *Hobby Model UAV*, represents a design commonly found in the hobbyist UAV market 3.3. By leveraging this model, CFD simulations can be employed to analyze and optimize aerodynamic performance. CFD has become an indispensable tool in UAV design, enabling detailed examinations of complex flow phenomena and providing insights into lift, drag, and stability characteristics under various flight conditions.

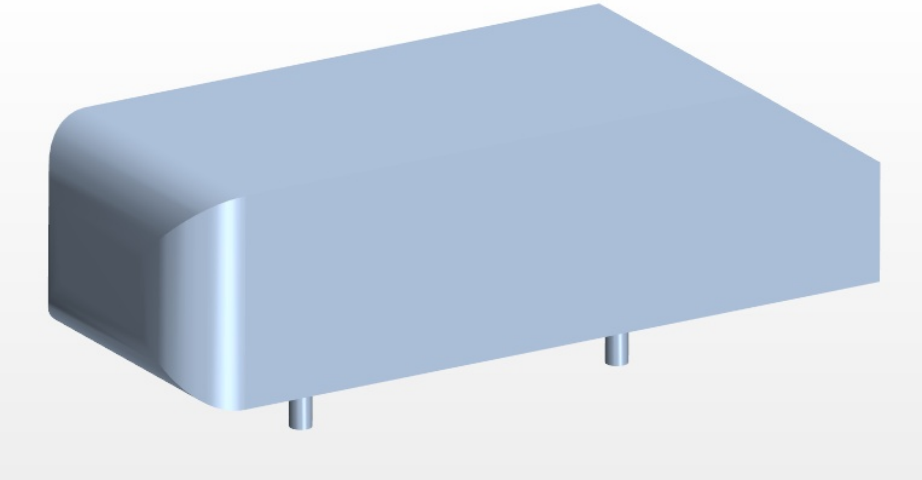

Figure 3.2: A 35-degree Ahmed body model [8].

Figure 3.3: Standardized MAV 'Hobby Model' UAV used in this thesis. Image Credit: Holybro (`https://holybro.com/collections/x500-kits/products/px4-development-kit-x500-v2`), Accessed on: 5 December, 2024.

The Hobby Model UAV serves as a practical and effective surrogate for military-grade drones due to its aerodynamic configuration, which closely resembles that of operational UAVs, and the availability of comprehensive CAD and aerodynamic data. Utilizing this model enables the derivation of aerodynamic coefficients through high-fidelity CFD simulations, providing a robust foundation for analyzing and optimizing its performance. Furthermore, the influence of design modifications on critical performance metrics, such as drag reduction and stability enhancement, can be system-

atically assessed. The insights obtained from these analyses are not only valuable for improving the Hobby Model UAV itself but also offer broader applicability to both military and civilian UAV designs.

As illustrated in Figure 3.4, the CAD geometry of the Hobby Model UAV is presented, which serves as the basis for the computational simulations.

Figure 3.4: Simplified UAV geometry used in the simulations. Left: Isometric view; Right: Top view.

To provide a clearer understanding of the combined aerodynamic configuration, the integration of the Ahmed body and the UAV is visually represented in Figure . This representation highlights the overall geometry and interaction between the two components, offering a comprehensive view of their spatial arrangement.

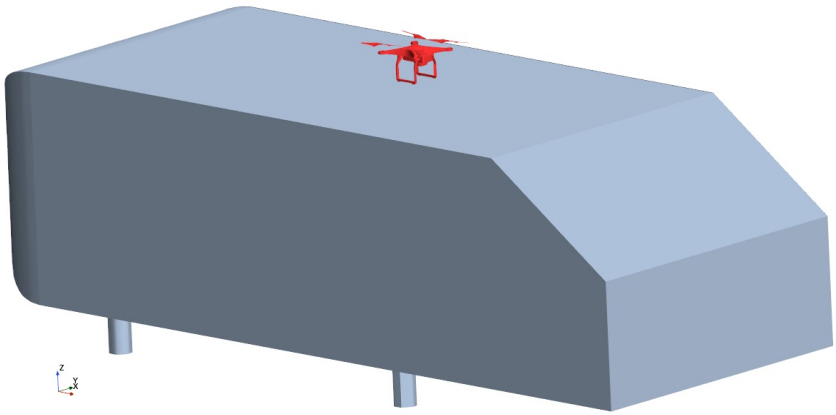

Figure 3.5: A depiction of the UAV's landing maneuver on the Ahmed body.

This research focuses on a comprehensive set of computational simulations per-

formed within distinct domains to investigate various aerodynamic phenomena. The scenarios examined include: (a) a full-scale Ahmed body positioned within a controlled wind tunnel environment, (b) an Ahmed body exposed to open-air conditions, (c) a UAV executing a hovering maneuver, and (d) a UAV performing a landing operation on the Ahmed body in an open-air setting. Each simulation domain is tailored to fulfill specific research goals. Simulations in domains (a) and (c) are primarily conducted to validate the accuracy and reliability of the CFD techniques by comparing results with experimental data. The open-air configuration in domain (b) is used to confirm that the validated methodology from domain (a) remains effective when applied outside the constraints of a wind tunnel. Lastly, domain (d) integrates aspects of both domains (b) and (c), enabling a detailed investigation of the aerodynamic interactions during the UAV's landing process on the Ahmed body under realistic open-air conditions.

For the wind tunnel simulation (domain a), the dimensions were set to $8L \times 5H \times 5W$, where L, H, and W represent the length, height, and width of the full-scale Ahmed body, respectively. These dimensions were derived from prior experimental studies [8] and CFD investigations [28]. The inlet and outlet boundaries were positioned at $2L$ upstream and $5L$ downstream of the Ahmed body, with the inlet treated as a velocity inlet and the outlet as a pressure outlet. To simulate crosswind effects, the front and back faces of the tunnel were also assigned velocity inlet and pressure outlet boundary conditions. The ground surface was modeled with a tangential velocity equal to the free-stream velocity to account for relative motion between the vehicle and ground. The top surface of the domain was treated as a gradient-free boundary condition.

The open-air simulation (domain b) adopted a similar configuration to that of domain (a) but with significantly larger dimensions ($31L \times 29H \times 40W$) to minimize blockage effects. In this setup, the inlet was located $10L$ upstream of the Ahmed

body, while the outlet was positioned $20L$ downstream. These extended boundaries ensured negligible interference from domain walls, closely approximating real world open-air conditions.

For simulations involving an isolated UAV (domain c), a bullet shaped axisymmetric computational domain was employed. The bottom surface of this domain was modeled as a no-slip wall to represent ground effects, while all other surfaces were assigned pressure outlet boundary conditions except for the hemispherical top surface, which was defined as a zero-velocity inlet. To simulate hovering maneuvers and rotor dynamics, an overset mesh approach was utilized. The UAV was placed within a translating overset region, accompanied by four additional overset sub regions around its rotors. These sub-regions moved synchronously with the main overset region to accurately capture rotor-induced flow characteristics during motion.

The primary domain of interest, referred to as domain (d), integrates both the UAV and GV. This domain shares similar dimensions with domain (b) but incorporates boundary conditions adapted from domain (c). Specifically, four vertical sides were treated as pressure outlets, while the top surface was defined as a zero-velocity inlet and the bottom surface as a no-slip wall. Overset regions surrounding the UAV were included in this domain to facilitate simulations involving rotor dynamics during landing maneuvers. Figure 3.5 illustrates the relative sizes and spatial arrangement of both the UAV and GV within this combined simulation setup.

These carefully designed simulation domains ensure robust validation of CFD methodologies while enabling detailed analysis of aerodynamic interactions between UAVs and ground vehicles under various operating conditions.

3.2 Meshing Methodology

The pre-processing phase for any CFD simulation utilizing the finite volume method involves discretizing the computational domain into a network of cells. This process encompasses geometry preparation, surface meshing, and volume meshing. In this

study, geometry preparation and surface meshing were carried out using ANSA Version 15.02. During this stage, non-essential UAV components and minor gaps were removed to streamline the computational model, thereby reducing simulation time while preserving the accuracy of flow predictions. Once the geometries were refined, they were imported into Siemens STAR-CCM+ 2310.0001 for further processing and simulation.

The Ahmed body geometry, being relatively simple, did not require any modifications and was directly meshed for external aerodynamic analysis. The meshing process underwent multiple iterations to achieve a balance between computational efficiency and accuracy. Mesh independence was ensured by correlating results with experimental data. For volume meshing, the "Trimmed Cell" mesher was employed, which primarily generated hexahedral cells. To enhance resolution in critical areas, several volume refinement zones were applied around key regions of the models, including eight refinement zones for the Ahmed body simulations. Prism layers were incorporated along solid surfaces to accurately capture boundary layer effects.

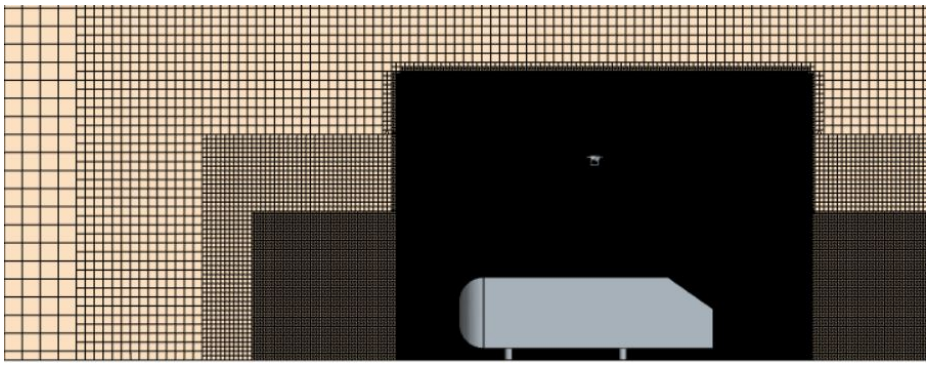

Figure 3.6: Ahmed body and UAV mesh.

The final cell count ranged from 68 million to 95 million cells for the descent speeds of 2, 4, 6, 8, and 10 m/s. The final mesh sizes varied depending on the specific simulation scenario, ranging from 16 million cells for the full-scale Ahmed body in a wind tunnel to 25 million cells for the Ahmed body in open-air conditions, 39 million cells for a scaled-up Ahmed body in open-air, and 24 million cells for the UAV in

hover. While these base meshes provided sufficient resolution for most flow features, additional refinement was necessary in regions with high flow gradients, such as rotor wakes and UAV-induced vortices.

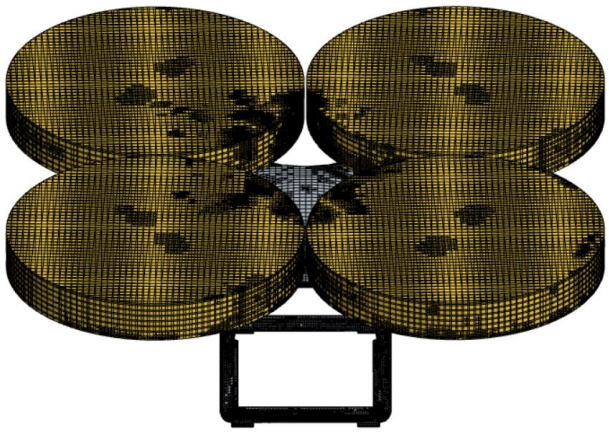

Figure 3.7: Mesh around the UAV rotors.

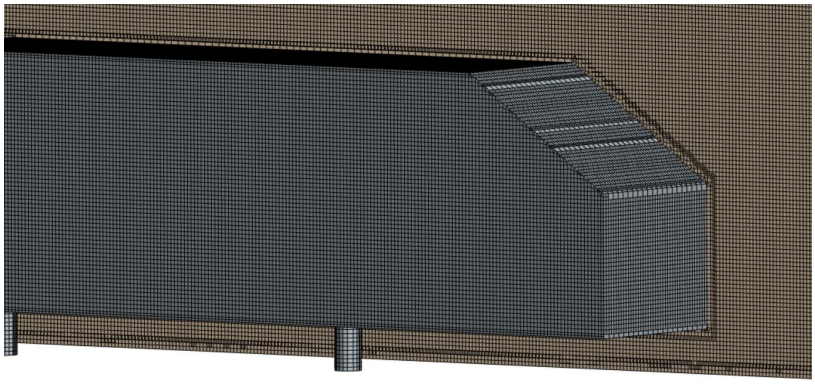

Figure 3.8: Ahmed body mesh scene on $y = 0$ plane.

To address this, an Adaptive Mesh Refinement (AMR) strategy was employed, leveraging the Q-criterion to dynamically refine the mesh in areas of interest. The Q-criterion is a well-established metric used to identify vortex-dominated regions within a flow field. It is mathematically expressed as: $Q = \frac{1}{2}\left(\|\Omega\|^2 - \|S\|^2\right)$, where S and Ω represent the strain-rate tensor and the rate-of-rotation tensor, respectively. In regions where rotational effects dominate over strain, $\|\Omega\|^2 > \|S\|^2$, resulting in a positive Q-value. This makes the Q-criterion an effective tool for identifying vortex-

dominated zones, which are critical to accurately resolving flow structures in this study.

Given that this research focuses on the interaction between the UAV wake and the flow field around the GV, achieving a well-resolved UAV wake is essential. The AMR process was specifically designed to refine the mesh in areas of high Q-criterion values, ensuring that key flow features such as rotor-induced vortices and wake interactions were captured with high fidelity. To evaluate the performance of the AMR approach,

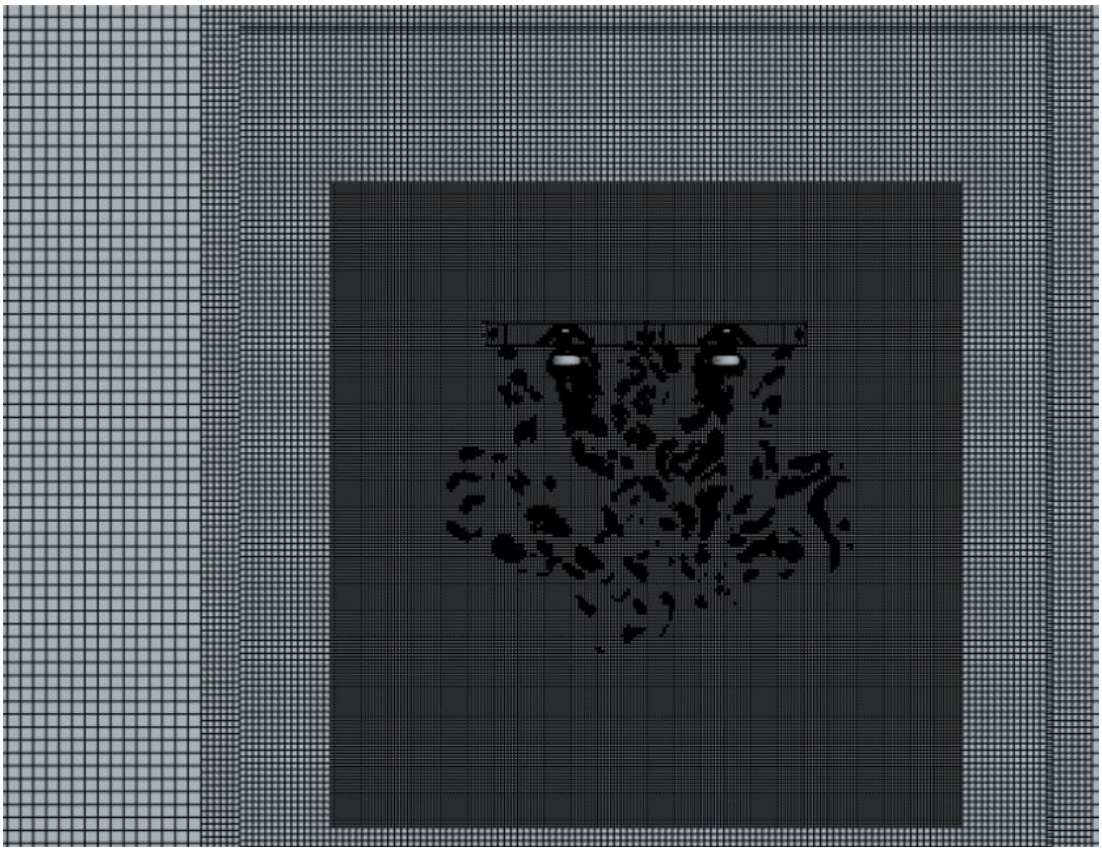

Figure 3.9: Mesh around the whole UAV.

the predicted wake field from this study, using a mesh consisting of 26 million cells, was compared against a highly detailed CFD simulation with 100 million cells conducted by Timms [25].

3.3 Solvers

The CFD simulations conducted in this study utilized the Improved Delayed Detached Eddy Simulation (IDDES) model with the Shear Stress Transport (SST) formulation, as implemented in the commercial finite volume CFD software Star-CCM+ by Siemens. The SST-based IDDES approach is widely recognized for its effectiveness in external aerodynamic studies of road vehicles due to its balance between computational efficiency and accuracy. This method provides high-fidelity flow predictions and is capable of capturing most of the dominant flow structures, making it particularly suitable for complex aerodynamic scenarios.

The IDDES framework integrates two modeling approaches: the Unsteady Reynolds-Averaged Navier-Stokes (URANS) model for resolving boundary layer flows and the Large Eddy Simulation (LES) approach for capturing unsteady flow structures in the wake region. This hybrid methodology is especially advantageous for studying regions of interest, such as wake dynamics, where significant turbulent scales are present. By combining the strengths of URANS and LES, the IDDES model ensures accurate representation of both near-wall and far-field flow phenomena.

Previous research by Bounds et al. [37] has demonstrated that the IDDES methodology is particularly well-suited for investigating fluid flow problems involving intricate aerodynamic interactions, such as those observed in ground vehicle platooning. These findings are directly relevant to the current study, which focuses on similar complex interactions between a UAV and a ground vehicle.

CHAPTER 4: RESULTS AND DISCUSSION

In this section, we will first discuss about the validation of our CFD process first. in the absence of experimental data pertaining to the landing maneuver of an unmanned aerial vehicle (UAV) onto a ground vehicle (GV) hereafter referred to as LMUAGV we have chosen to validate our computational fluid dynamics (CFD) methodology by correlating the results of our simulations with both experimental and CFD data available for isolated UAV and GV cases.

The next step is running the CFD simulations of the LMUAVGV cases with the five chosen descent velocities, which is the primary objective of this thesis. The results demonstrated significant variations across the different descent velocities. The analyses process involves collection of extensive data sets, which included UAV descent speeds and various scalars. These data sets were analyzed by selecting a subset of representative cases for comparative evaluation.

4.1 Validation of UAV and GV CFD Methodology

For the purpose of validating the CFD simulation methodology for the generic vehicle (GV), three distinct scenarios were considered. The first two simulations were designed to enable direct comparisons with both existing experimental data and previously published CFD results [28, 8]. These simulations specifically investigated the effects of different simulation environments, namely wind tunnel and open-air settings.

Wind-tunnel-based CFD simulations are widely regarded as highly effective for validation purposes due to their controlled conditions. However, they inherently lack a critical aspect of real-world scenarios: in practical applications, the vehicle

moves relative to an unbounded environment, whereas in a wind tunnel, the air flows relative to a stationary vehicle within a confined domain. This fundamental difference significantly influences the ability to capture aerodynamic interactions under realistic operational conditions.

A comparative analysis between these two cases revealed slight variations in the vorticity distribution between the wind tunnel (WT) and open-air domains. Notably, the open air domain exhibited a lower pressure region extending beyond the vehicle compared to its wind tunnel counterpart. These differences underscore the importance of considering open air conditions when simulating real world aerodynamic behavior.

The third and final simulation focused on an isolated GV model to validate its scaled-up version based on the Ahmed body geometry. This step ensured consistent results when transitioning to full-scale simulations. These results are presented in Table 4.1. A comparison of the results from the wind tunnel-based cases demonstrated that our CFD methodology achieved predictions with less than 1% deviation from the published experimental data, highlighting its accuracy and reliability. For brevity, we are omitting the detailed analyses of this validation process as it is presented in detail in our earlier publication which also including mesh and time-step independence studies; see Uddin et al. [29]. Though only a summary comparison of the headline coefficient data is presented in Table 4.1, Uddin et al. [29] also contains a comparison of the flow-fields between CFD and experiment. This comparison demonstrates a very high degree of correlation between CFD predictions and experimental measurements, particularly in terms of pressure and velocity distributions in the wake region.

Table 4.1: Ahmed Body Validation Results

Case	C_D	Std Dev.
Experiment, Ahmed et al. [8]	0.258	0.003
CFD: Wind-Tunnel Domain	0.255	0.004
CFD: Open-Air Domain	0.239	0.003
CFD: Scaled Up Ahmed body Open-Air Domain	0.241	0.004
CFD: WT Domain, Guillmineau [28]	0.345	0.009

For the UAV CFD validation, we benchmarked the results of our simulations against those reported by Timms [25], while for the GV, we compared our findings with the experimental data provided by Ahmed et al. [8] as well as the CFD predictions from Guilmineau et al. [28].

It is worth noting that Timms's [25] CFD methodology was itself validated using experimental data from Zhou et al. [30] and CFD results from Schenk [38]. However, Timms's study focused solely on an isolated UAV and required a simulation domain comprising approximately 100 million computational cells. Extending this simulation to include a ground vehicle (GV) within the computational domain would necessitate over 300 million cells, which exceeds the computational resources available to our research group.

To address these limitations, we employed an adaptive mesh refinement (AMR) technique, which significantly reduced the computational cost while maintaining high accuracy. Specifically, this approach allowed us to achieve a 75% reduction in total cell count, resulting in a simulation comprising approximately 26 million cells. Despite this reduction, our CFD results demonstrated excellent agreement with those of Timms [25], achieving a correlation within 3%, as shown in Table 4.2.

Table 4.2: UAV Validation Results

Case	Thrust (N)
Timms CFD [25]	3.169
Isolated UAV in Hover [29]	3.271

Building on this validation, further analysis was conducted to investigate the onset of the Vortex Ring State (VRS) during UAV descent. Through detailed simulations, it was observed that the VRS begins to develop at descent rates approaching 6 m/s. To numerically confirm this finding, a controlled hovering test was performed to measure the vertical induced velocity (v_h) generated by each rotor of the UAV. The results indicated a vertical velocity of $v_h = 5.82\,\mathrm{m/s}$ as shown on Figures 4.1b, and 4.1a.

This implies that a descent velocity of 6 m/s corresponds to a ratio $-v_d$ to v_h of 1.03. As can be seen later that the UAV transitions into the VRS regime at descent rates around 6 m/s. This observation is consistent with the findings of Bangura et al. [2].

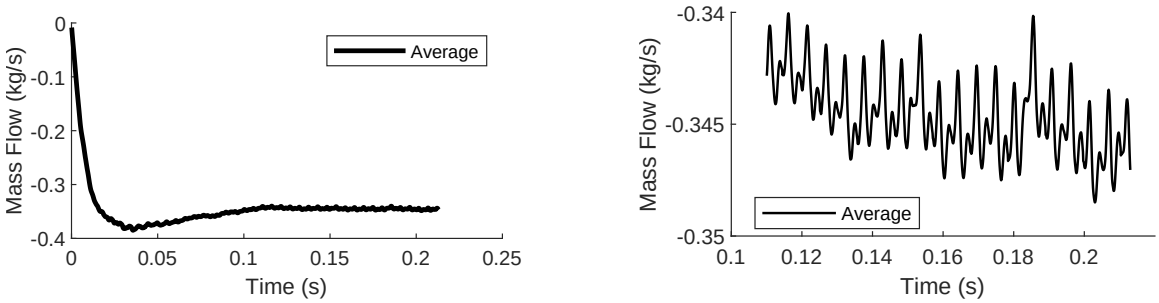

(a) (b)

Figure 4.1: (a) Mass flow rate through the rotors, averaged over all four rotors, plotted as a function of real time; (b) A magnified view of a selected segment from (a).

4.2 Flow Evolution During UAV Descent at Different Speeds

To comprehensively address the research objectives, a series of computational simulations were performed at descent speeds of 2, 4, 6, 8, and 10 m/s. These simulations were designed to investigate the effects of varying descent velocities on UAV stability, wake dynamics, and overall aerodynamic performance. Particular emphasis was placed on examining the onset and severity of the VRS under different descent conditions. Furthermore, the study aimed to analyze the aerodynamic interactions between the UAV's downwash and the surfaces of the GV, offering valuable insights into the coupled dynamics of the UAV-GV system.

Building on these objectives, the evolution of flow during UAV descent is analyzed in detail at three representative velocities: 2 m/s, 6 m/s, and 10 m/s. These velocities correspond to three aerodynamic states as defined in Bangura et al. [2]:

- **Normal Working State (NWS)**: This state occurs at lower descent velocities, such as 2 m/s, where the rotor-induced flow remains stable and well organized.
- **Vortex Ring State (VRS)**: Observed at intermediate descent velocities, such

as 6 m/s, this state is characterized by the formation of a vortex ring structure around the rotor system, leading to significant flow recirculation and instability.

- **Intermediate State Between Turbulent Wake State (TWS) and Windmill Brake State (WBS)**: At higher descent velocities, such as 10 m/s, the flow transitions into a regime where elements of both TWS and WBS are observed. This state involves complex interactions between wake turbulence and aerodynamic braking effects.

To further investigate these states, we compare the flow interactions at three relative positions of the UAV with respect to the upper surface of a ground vehicle (GV). These positions are defined by the dimensionless height parameter $h^* = h/d$, where h represents the vertical distance from the bottom of the UAV to the top surface of the GV, and d denotes the rotor diameter. The analysis considers all five descent velocities studied in this research.

A detailed side-by-side comparison is performed for key flow characteristics as the UAV descends from $h^* = 7.55$ to positions near landing. This comparison focuses on three representative descent velocities: 2 m/s, 6 m/s, and 10 m/s. These velocities highlight critical transitions in aerodynamic behavior during descent.

To evaluate the impact of descent velocity on aerodynamic interactions between the UAV wake and the GV, several scalar quantities are analyzed in detail:

- **Normalized Vertical Velocity (V_z^*)**: This parameter provides insight into vertical flow dynamics relative to rotor-induced wake effects.

- **Pressure Coefficient (C_p)**: The distribution of pressure on surfaces is examined to understand aerodynamic loading variations.

- **Q-Criterion Iso-Surfaces**: These iso-surfaces are used to visualize coherent vortex structures within the wake region.

- **Vorticity Fields** (ω_k): The vorticity distribution is analyzed to characterize rotational flow features and turbulence levels.

While this thesis focuses on these primary aerodynamic quantities, additional metrics related to moments and forces are deferred for future work. These include:

- **Yawing Moment Coefficient** (C_{YM}): Quantifies rotational moments about the vertical axis due to asymmetric wake interactions.
- **Pitching Moment Coefficient** (C_{PM}): Represents moments about the lateral axis caused by variations in downwash and pressure distribution.
- **Drag Coefficient** (C_D): Provides insights into overall resistance forces acting on both UAV and GV during descent.

These additional metrics will be critical for understanding why specific descent speeds were selected for analysis and how they correlate with oscillatory behaviors observed in simulations. The current study lays a foundation for exploring these phenomena by focusing on key flow characteristics during UAV descent.

4.3 Descent Velocity of UAV at 2 m/s

The CFD results for the UAV descending onto the GV at a vertical velocity of 2 m/s are illustrated in Figure 4.2. These results provide a detailed visualization of the scalar fields associated with various flow parameters. Specifically, the velocity components (V_x, V_y, and V_z) are presented in Figures 4.2, 4.3, and 4.4, respectively. Additionally, Figures 4.5, 4.6, and 4.7 depict scalar fields for the pressure coefficient (C_p), vorticity magnitude, and Q-criterion, respectively. Each subfigure corresponds to a non-dimensional height, h^*, of the UAV during its descent. The specific values of h^* are: (Top row, left to right) h^*= 7.55, 5.87, and 4.87, and (Bottom row, left to right) h^*= 3.36, 1.26, and 0.42. The same convention of figure ordering is followed for the other descent rates of 4, 6, 8, and 10 m/s.

The results highlight a distinct interaction between the aerodynamic fields of the UAV and the GV as the UAV descends. Initially, the UAV's pressure field begins to interact with the GV at a relatively large separation distance, becoming evident in the V_x scalar field at approximately $h^* = 5.87$. At this stage, the influence of the UAV's downwash velocity on the GV is minimal. As the UAV continues its descent, further interactions occur when its wake begins to impinge on the GV at around $h^* = 4.87$. This marks a transition where both pressure and velocity effects become more pronounced.

A unique feature of this descent rate is observed as the UAV approaches closer to the GV surface. Unlike other descent rates, where concentrated wake regions or strong vorticity fields may persist near the UAV, this case demonstrates significant wake dispersion across the GV surface as the UAV nears $h^* = 0.42$. This dispersion effectively minimizes concentrated vorticity regions or localized aerodynamic disturbances near the UAV, suggesting a smoother interaction between the UAV's wake and the GV at lower altitudes.

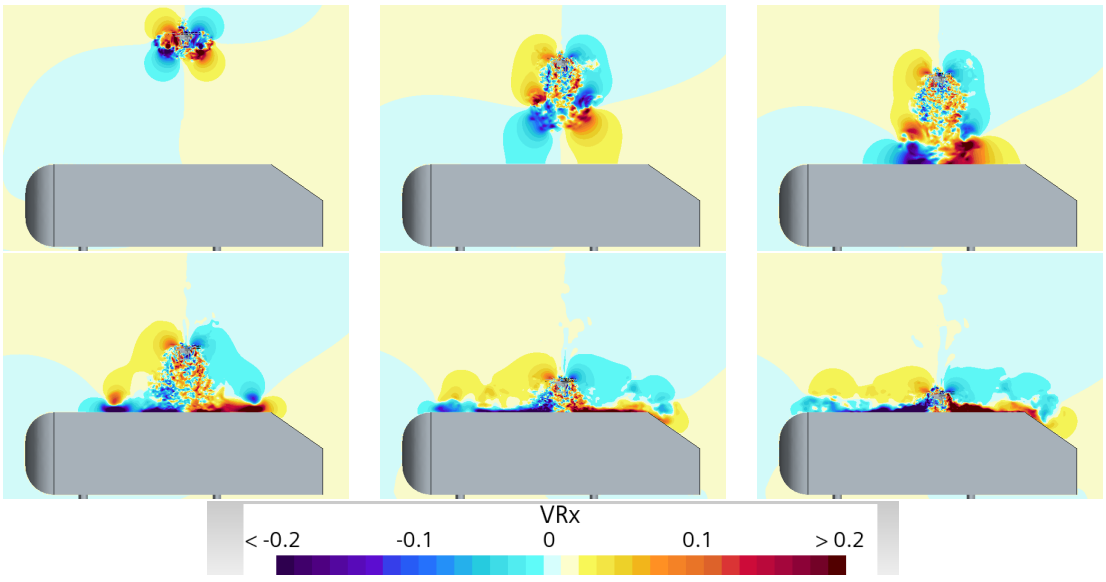

Figure 4.2: Contours of V_x for $v_d = -2$ m/s. Top row (left to right): h^*= 7.55, 5.87, and 4.87; Bottom row (left to right): h^*= 3.36, 1.26, and 0.42.

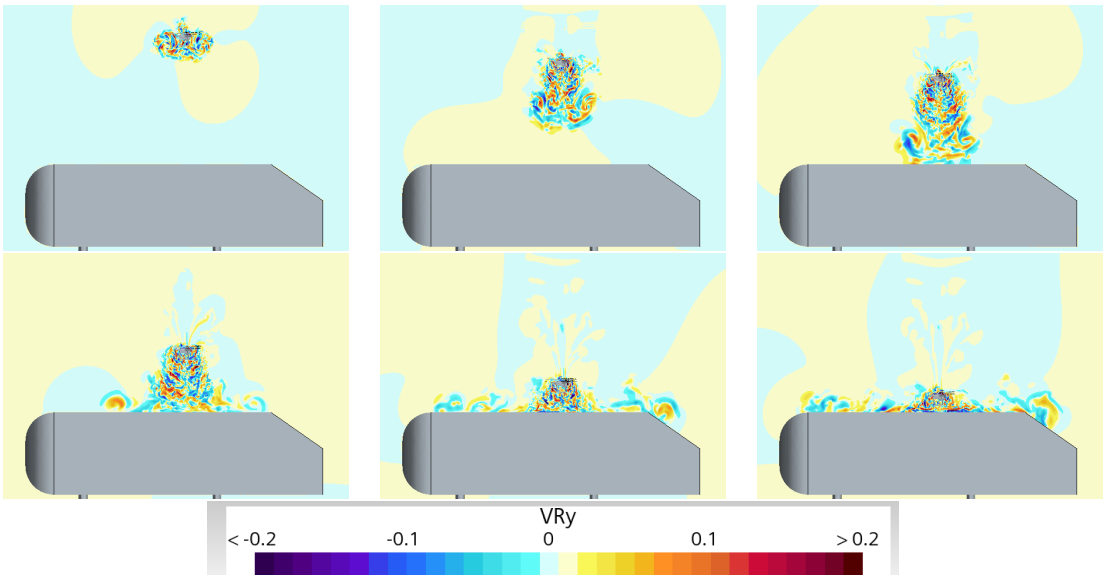

Figure 4.3: Contours of V_y for $v_d = -2$ m/s. Top row (left to right): h^*= 7.55, 5.87, and 4.87; Bottom row (left to right): h^*= 3.36, 1.26, and 0.42.

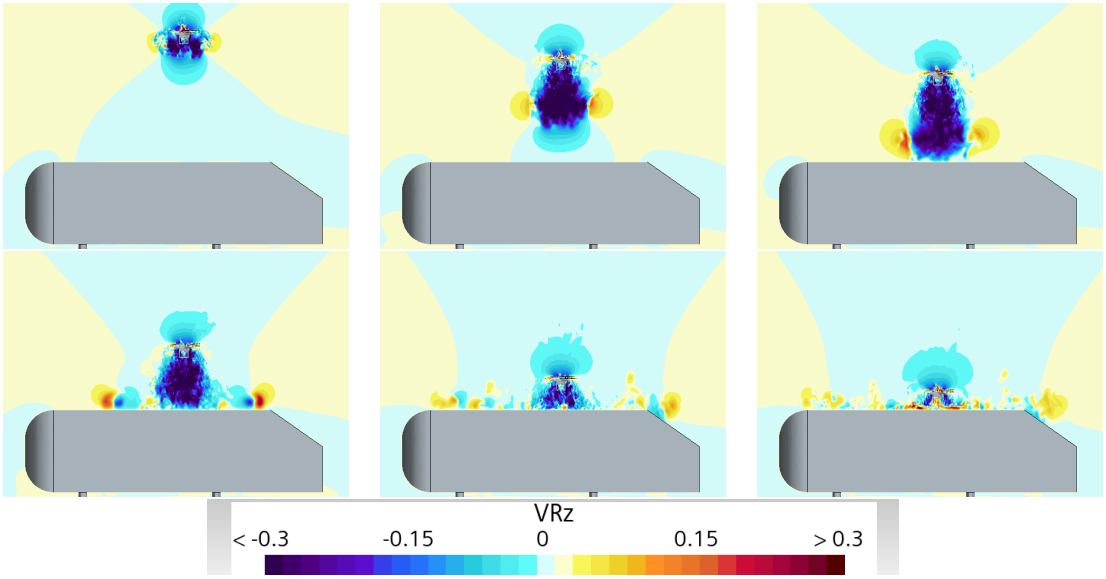

Figure 4.4: Contours of V_z for $v_d = -2$ m/s. Top row (left to right): h^*= 7.55, 5.87, and 4.87; Bottom row (left to right): h^*= 3.36, 1.26, and 0.42.

4.4 Descent Velocity of UAV at 4 m/s

The descent of the UAV at a velocity of 4 m/s presents several intriguing observations throughout the simulation. Notably, the velocity field and wake remain predominantly ahead of the UAV, effectively preventing the formation of the VRS.

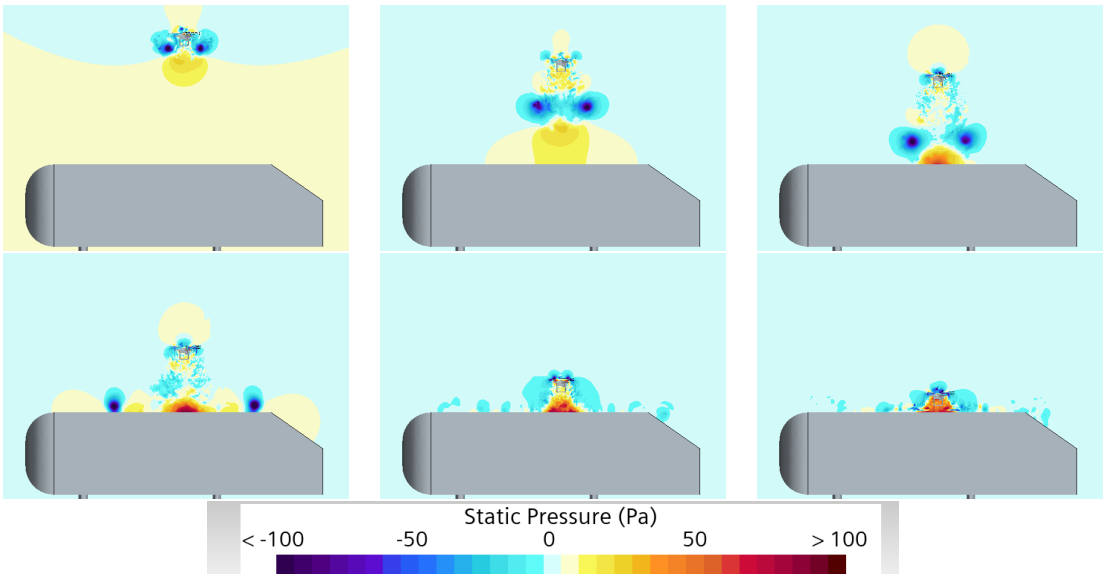

Figure 4.5: Contours of C_p for $v_d = -2$ m/s. (Top row (left to right): h^*= 7.55, 5.87, and 4.87; Bottom row (left to right): h^*= 3.36, 1.26, and 0.42.

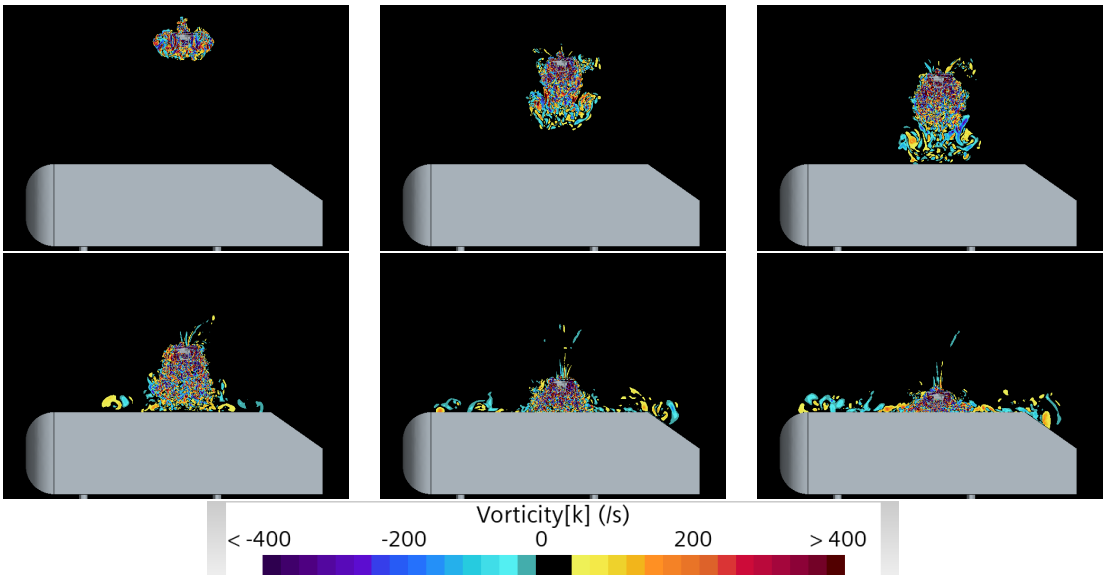

Figure 4.6: Contours of Ω for $v_d = -2$ m/s. Top row (left to right): h^*= 7.55, 5.87, and 4.87; Bottom row (left to right): h^*= 3.36, 1.26, and 0.42.

However, it is important to highlight that, compared to a descent velocity of 2 m/s, the velocity field and wake are positioned significantly further behind the UAV. This phenomenon is particularly evident in Figures 4.8, 4.9, and 4.12, which illustrate the wake's spatial dynamics and its relationship with the UAV's motion.

While these scalar fields emphasize that the wake remains ahead of the UAV, ad-

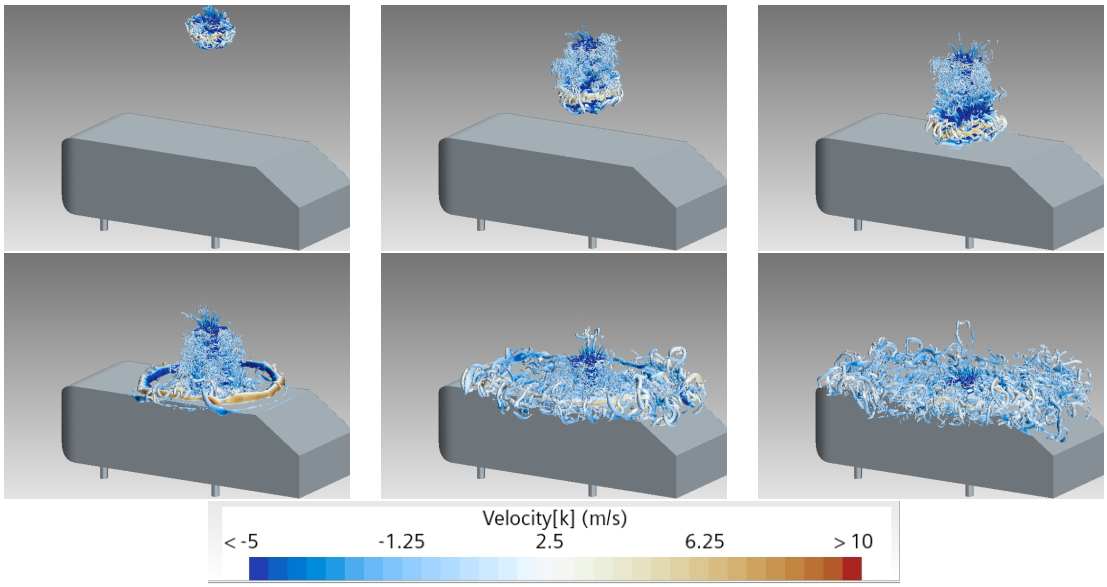

Figure 4.7: Contours of $Q-$criteria for $v_d = -2$ m/s. Top row (left to right): h^*= 7.55, 5.87, and 4.87; Bottom row (left to right): h^*= 3.36, 1.26, and 0.42.

ditional scalar visualizations in Figures 4.11 and 4.13 provide insights into the wake's distribution across the Ahmed body. These figures reveal patterns of wake disruption that, while not definitively indicative of VRS, suggest that the system may be approaching this aerodynamic regime. This observation aligns with theoretical insights provided by Mullen [11] and Bangura et al. [2], who describe similar transitional behaviors leading up to VRS conditions.

In summary, while the descent at 4 m/s does not exhibit clear evidence of VRS formation, the observed wake dynamics and their distribution suggest that the system may be nearing this critical aerodynamic state. These findings underscore the importance of further investigation into the interplay between descent velocity, wake behavior, and VRS onset to better understand these complex aerodynamic phenomena.

4.5 Descent Velocity of UAV at 6 m/s

To further investigate the aerodynamic behavior at critical descent rates, scaled numerical simulations were performed specifically at a descent rate of 6 m/s. These

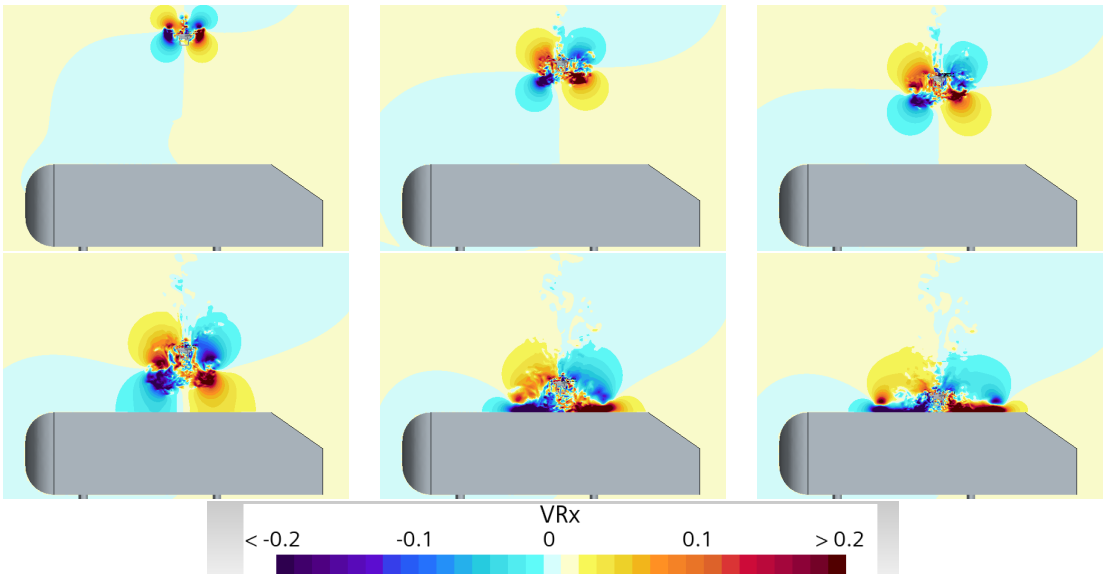

Figure 4.8: Contours of V_x for $v_d = -4$ m/s. Top row (left to right): h^*= 7.55, 5.87, and 4.87; Bottom row (left to right): h^*= 3.36, 1.26, and 0.42.

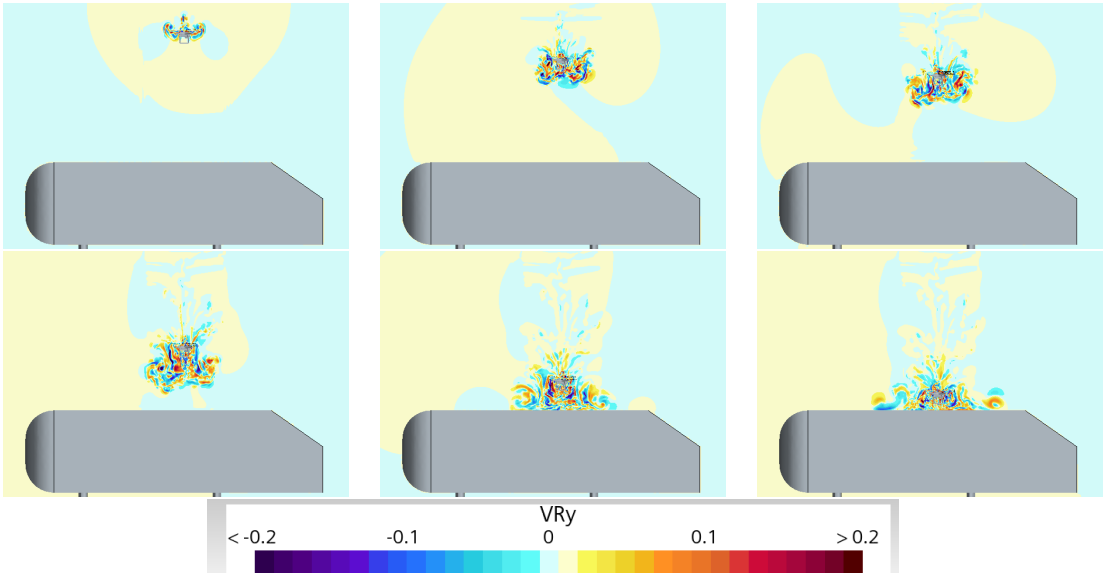

Figure 4.9: Contours of V_y for $v_d = -4$ m/s. Top row (left to right): h^*= 7.55, 5.87, and 4.87; Bottom row (left to right): h^*= 3.36, 1.26, and 0.42.

simulations were designed to analyze key scalar fields, including the non-dimensional velocity components (V_x^*, V_y^*, and V_z^*), coefficient of pressure (C_p), velocity magnitude, and Q-criteria. The results, presented in Figures 4.14, 4.15, and 4.16, reveal that at this descent rate, the wake and vorticity fields exhibit consistent patterns and sustained interaction between the UAV and GV effects.

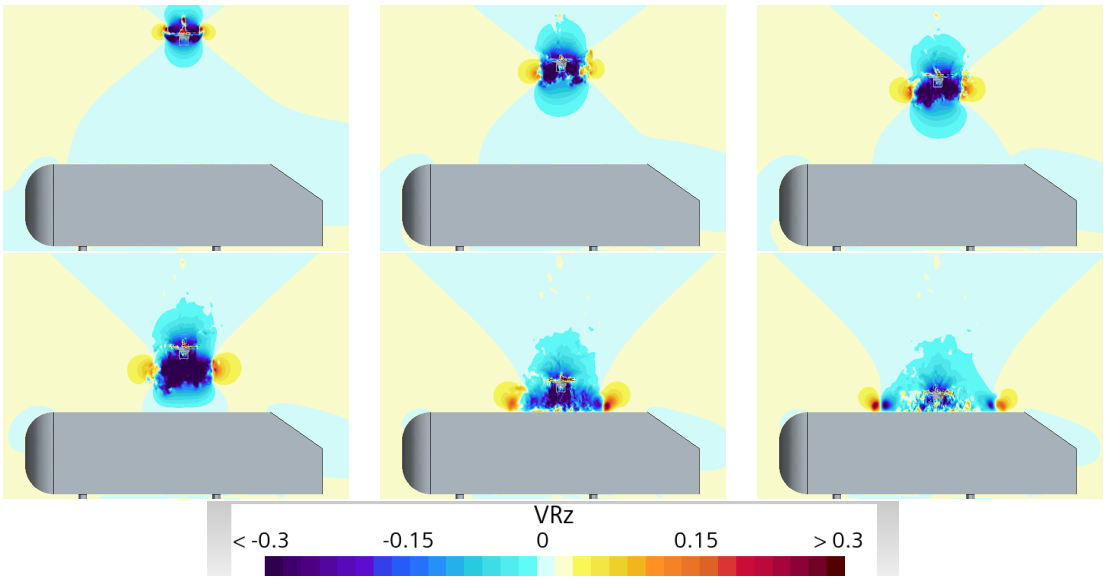

Figure 4.10: Contours of V_z for $v_d = -4$ m/s. Top row (left to right): h^*= 7.55, 5.87, and 4.87; Bottom row (left to right): h^*= 3.36, 1.26, and 0.42.

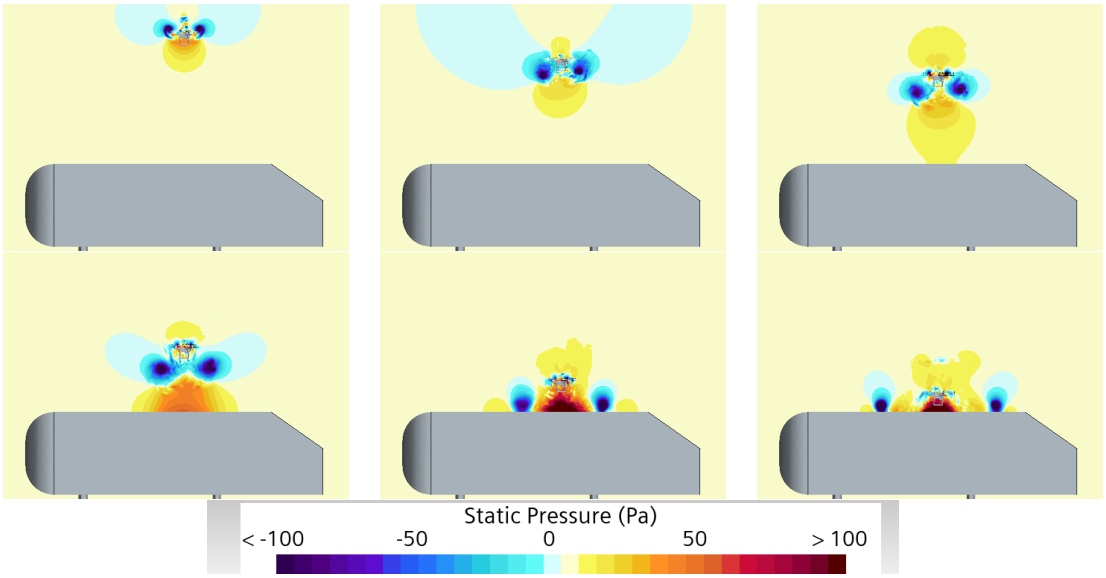

Figure 4.11: Contours of C_p for $v_d = -4$ m/s. (Top row (left to right): h^*= 7.55, 5.87, and 4.87; Bottom row (left to right): h^*= 3.36, 1.26, and 0.42.

This persistent interaction underscores the distinct flow dynamics associated with a descent rate of 6 m/s, which is particularly significant due to its proximity to the onset of the VRS. Additionally, these findings are closely tied to the rotor mass flow characteristics, as shown in Figures 4.1b and 4.1a. The analysis of mass flow rates further highlights the influence of rotor-induced flows on the overall aerodynamic

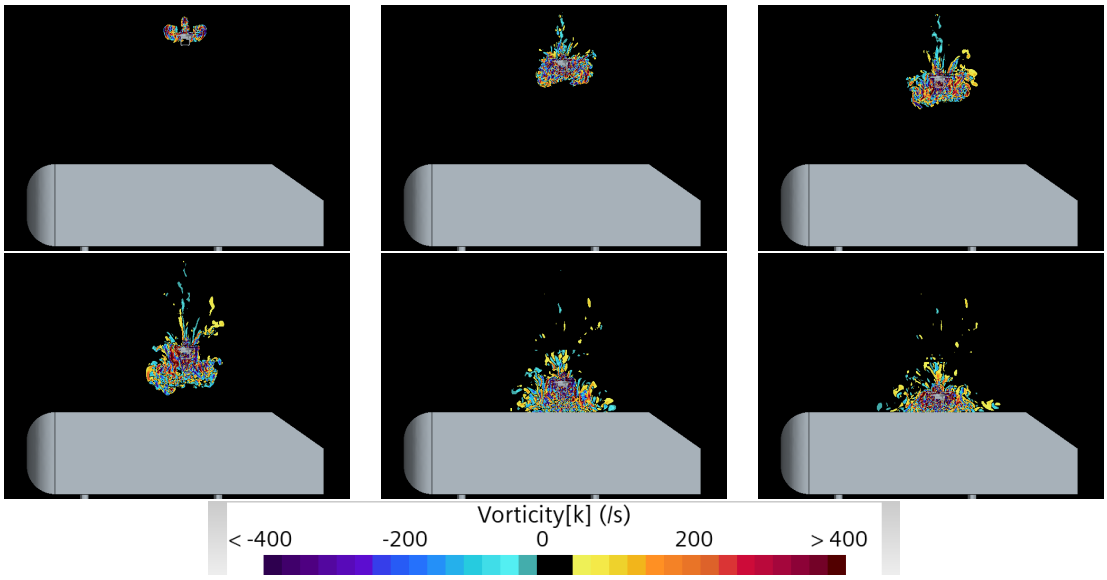

Figure 4.12: Contours of Ω for $v_d = -4$ m/s. Top row (left to right): h^*= 7.55, 5.87, and 4.87; Bottom row (left to right): h^*= 3.36, 1.26, and 0.42.

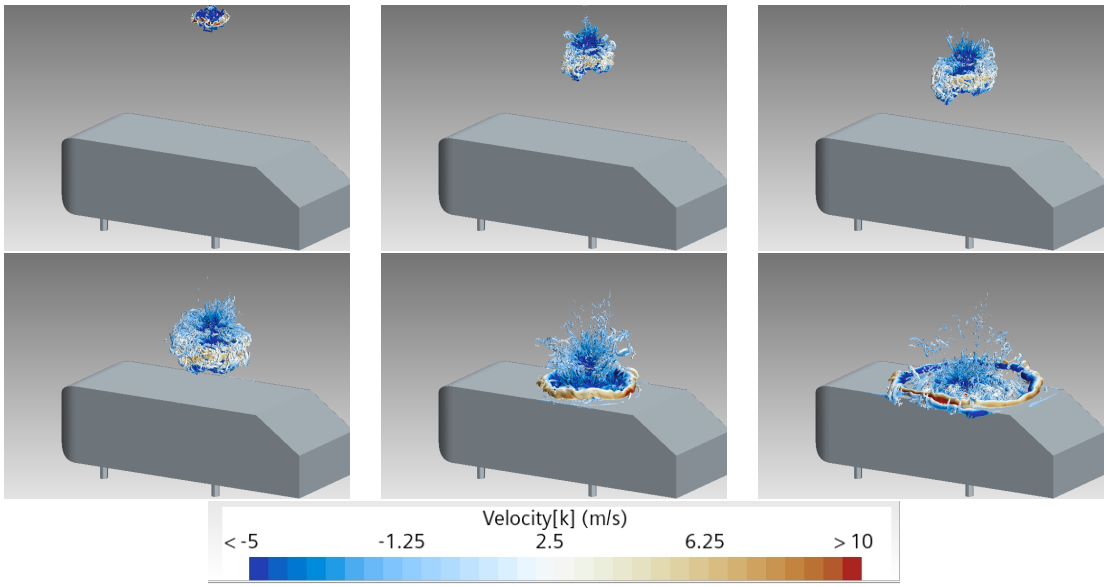

Figure 4.13: Contours of $Q-$criteria for $v_d = -4$ m/s. Top row (left to right): h^*= 7.55, 5.87, and 4.87; Bottom row (left to right): h^*= 3.36, 1.26, and 0.42.

performance during descent, providing deeper insight into the complex interactions at this critical operating condition.

Based on the calculated vertical velocity ($V_z = 5.82\,\text{m/s}$) and corroborating findings from Hoffmann and Bangura [1, 2], it can be inferred that at a descent rate of

6 m/s, the UAV is entering the VRS. This regime is characterized by complex wake interactions that lead to increased instability in flight dynamics. Furthermore, it can be hypothesized that at higher velocities such as 8 m/s and 10 m/s, the UAV transitions into a turbulent wake state where aerodynamic disturbances become even more pronounced. However, additional data processing and further analysis are required to confirm this hypothesis with greater certainty.

What sets the 6 m/s descent rate apart from lower velocities such as 2 m/s and 4 m/s is the behavior of the wake generated during the interaction between the UAV and GV. At 6 m/s, the wake remains tightly confined within a cohesive, bubble-like structure that does not dissipate or expand as observed at lower velocities. This distinct bubble-like structure is indicative of strong aerodynamic coupling between the UAV's downwash and its surrounding flow field.

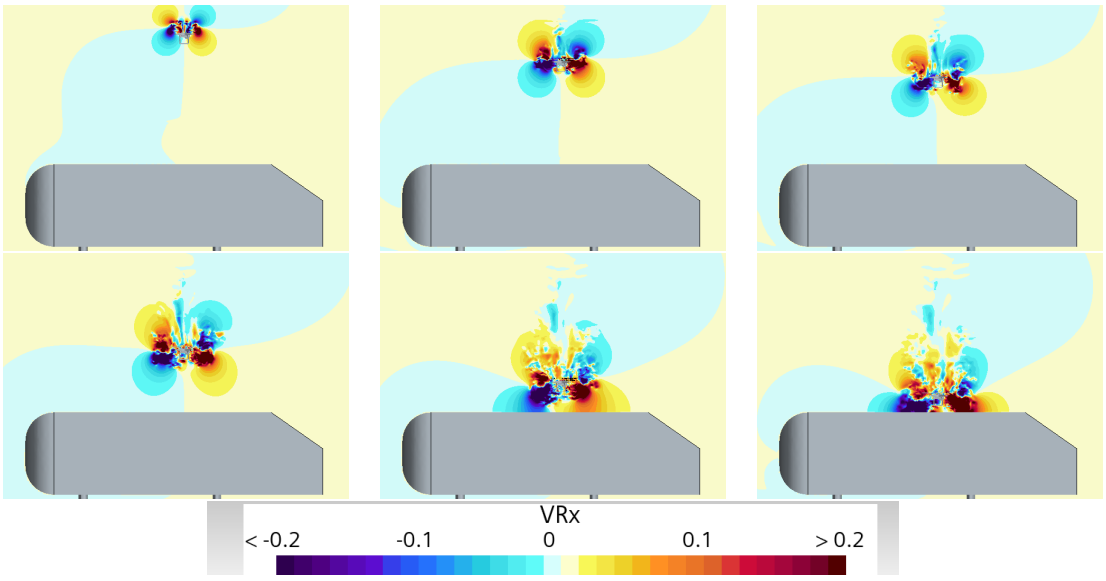

Figure 4.14: Contours of V_x for $v_d = -6$ m/s. Top row (left to right): h^*= 7.55, 5.87, and 4.87; Bottom row (left to right): h^*= 3.36, 1.26, and 0.42.

4.6 Descent Velocity of UAV at 8 m/s

The descent of the UAV at a velocity of 8 m/s reveals aerodynamic characteristics that suggest a transitional state nearing the vortex ring state (VRS). Building upon

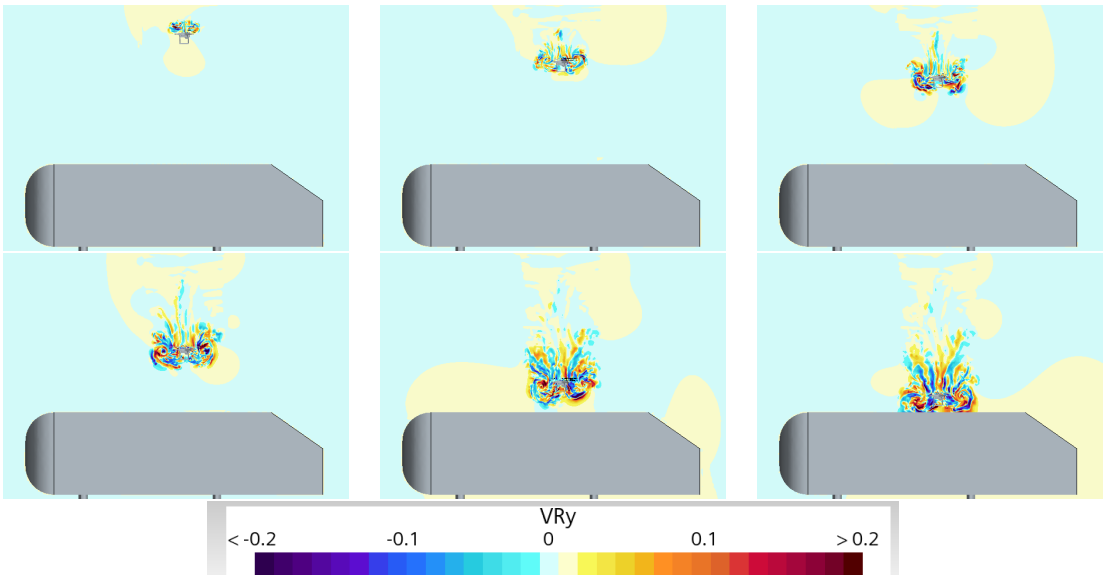

Figure 4.15: Contours of V_y for $v_d = -6$ m/s. Top row (left to right): h^*= 7.55, 5.87, and 4.87; Bottom row (left to right): h^*= 3.36, 1.26, and 0.42.

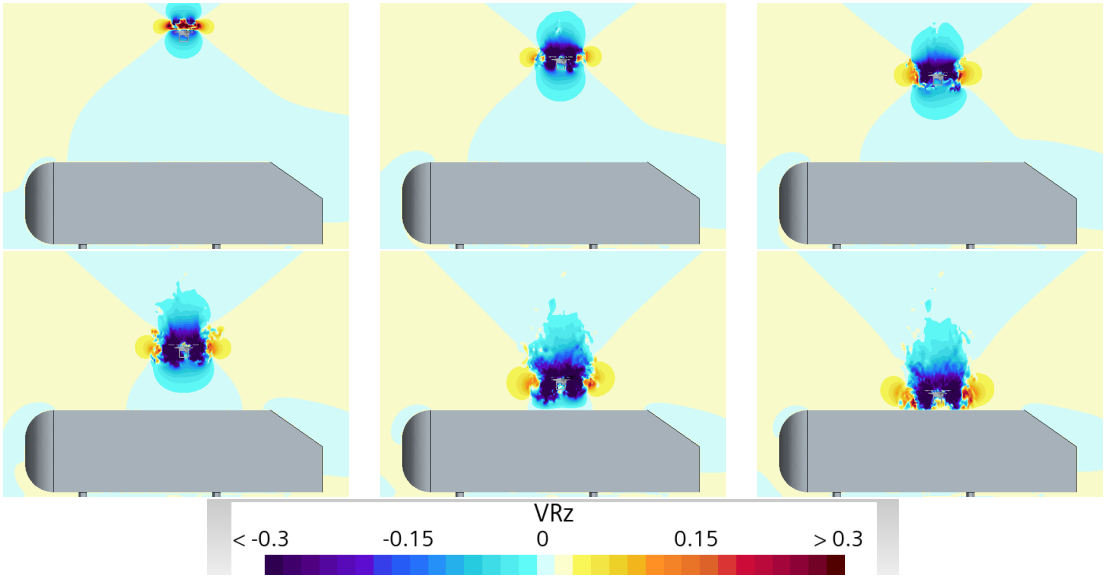

Figure 4.16: Contours of V_z for $v_d = -6$ m/s. Top row (left to right): h^*= 7.55, 5.87, and 4.87; Bottom row (left to right): h^*= 3.36, 1.26, and 0.42.

observations from the 4 m/s descent, the wake dynamics at this higher velocity provide further insights into the complex behavior of the system. During the 8 m/s descent, the wake remains confined within the rotor region of the UAV, which strongly implies that VRS conditions may be forming. However, an alternative hypothesis is that the system has transitioned into a turbulent wake state. This interpretation is supported

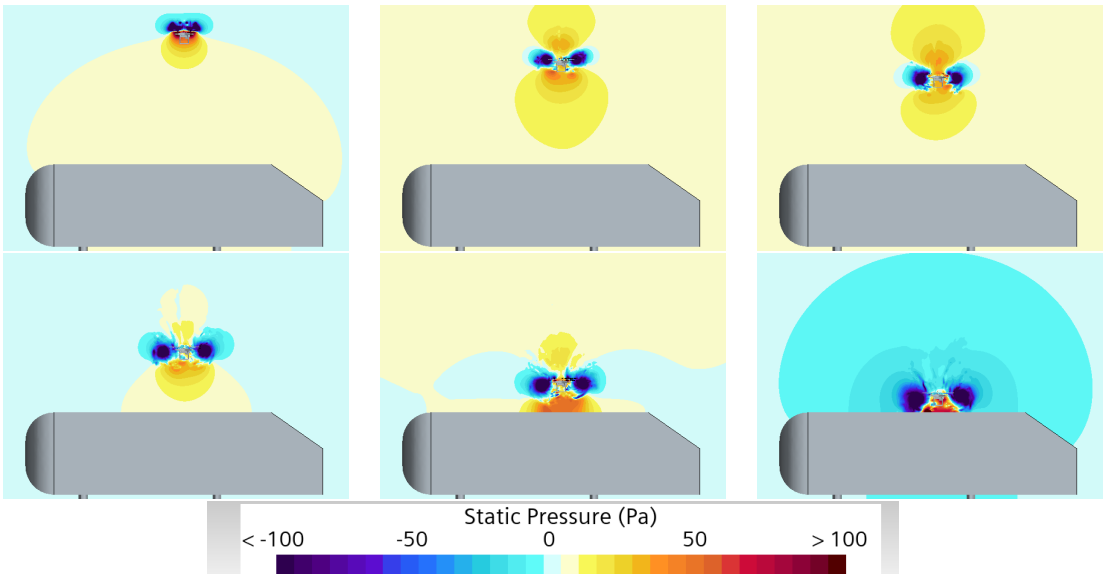

Figure 4.17: Contours of C_p for $v_d = -6$ m/s. Top row (left to right): h^*= 7.55, 5.87, and 4.87; Bottom row (left to right): h^*= 3.36, 1.26, and 0.42.

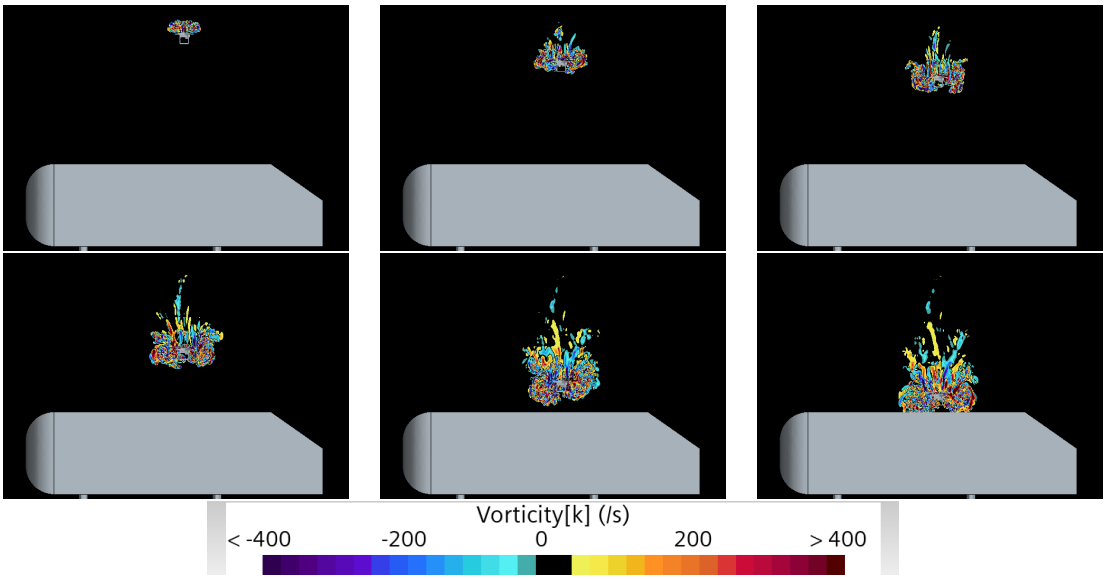

Figure 4.18: Contours of Ω for $v_d = -6$ m/s. Top row (left to right): h^*= 7.55, 5.87, and 4.87; Bottom row (left to right): h^*= 3.36, 1.26, and 0.42.

by the velocity and wake patterns trailing behind the UAV, as illustrated through scalar field visualizations in Figures 4.21, 4.22, and 4.23.

A detailed analysis of these scalar fields reveals significant turbulence and disruption in wake behavior. Of particular note is the static pressure distribution, as shown in Figure 4.23, which demonstrates a pronounced shift in wake dynamics compared to

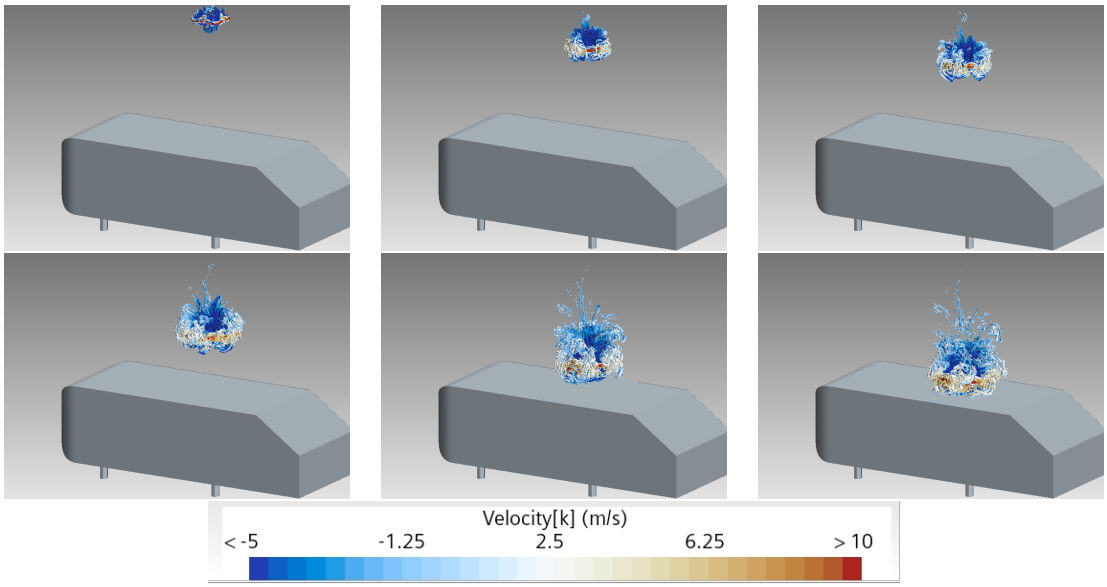

Figure 4.19: Contours of $Q-$criteria for $v_d = -6$ m/s. Top row (left to right): h^*= 7.55, 5.87, and 4.87; Bottom row (left to right): h^*= 3.36, 1.26, and 0.42.

lower descent velocities. In contrast to the 6 m/s descent case, where the main wake remains predominantly below or behind the rotors, at 8 m/s, the wake has moved to a position directly over the rotor region. This change signifies a critical alteration in aerodynamic behavior that could correspond to either VRS onset or a fully developed turbulent wake state.

Another noteworthy observation concerns the evolution of Q-Criteria visualizations with increasing descent velocities. As shown in Figure 4.25, the bubble-like formations associated with Q-Criteria become more encapsulated at 8 m/s compared to their expansive nature at lower velocities, such as in the 2 m/s descent depicted in Figure 4.7. This encapsulation suggests reduced wake distribution, providing evidence that aerodynamic impacts on the Ahmed body are less steady at higher descent velocities. The contraction of Q-Criteria structures may also indicate a more localized concentration of vortical activity near critical regions of the UAV.

These findings highlight the intricate nature of aerodynamic transitions as descent velocity increases. While there is compelling evidence to support VRS formation at 8 m/s, the turbulent characteristics of the wake introduce ambiguity in definitively

identifying this state. The interplay between VRS and turbulent wake dynamics underscores the need for further investigation to clarify these phenomena and assess their implications for UAV performance, stability, and control during high-speed descents.

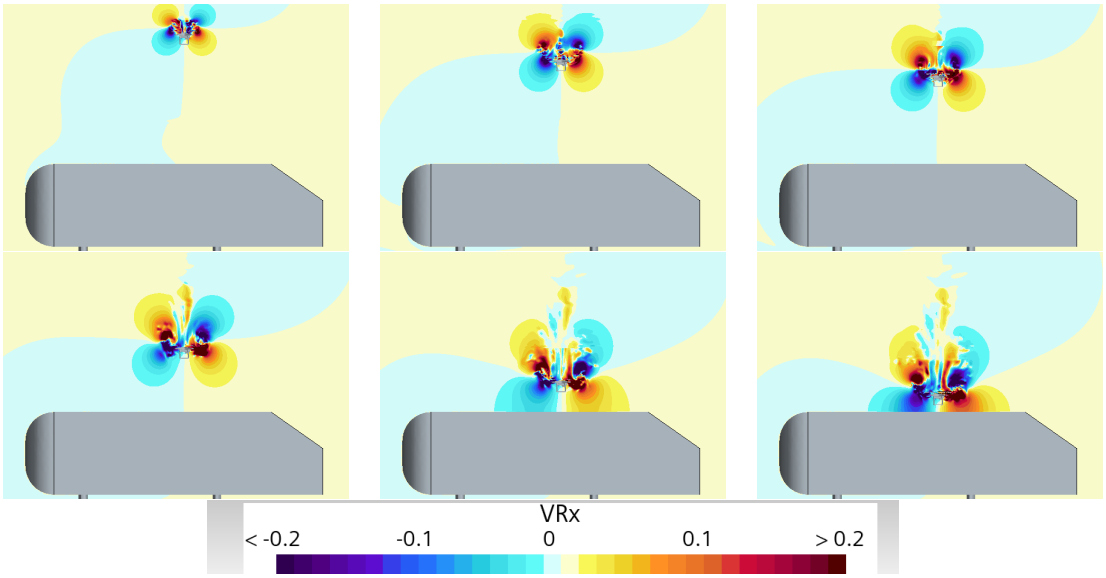

Figure 4.20: Contours of V_x for $v_d = -8$ m/s. Top row (left to right): h^*= 7.55, 5.87, and 4.87; Bottom row (left to right): h^*= 3.36, 1.26, and 0.42.

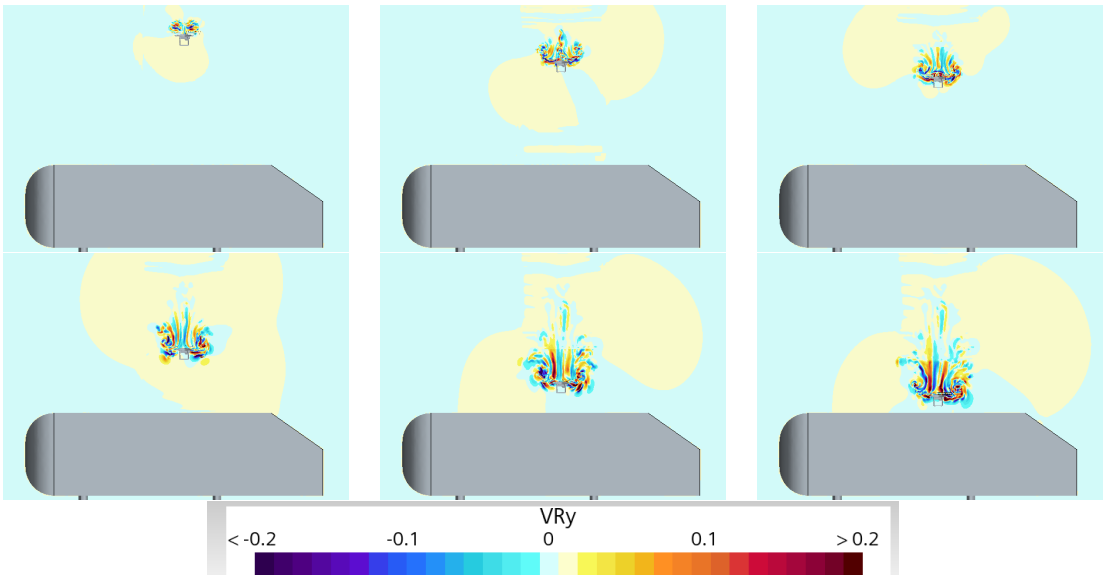

Figure 4.21: Contours of V_y for $v_d = -8$ m/s. Top row (left to right): h^*= 7.55, 5.87, and 4.87; Bottom row (left to right): h^*= 3.36, 1.26, and 0.42.

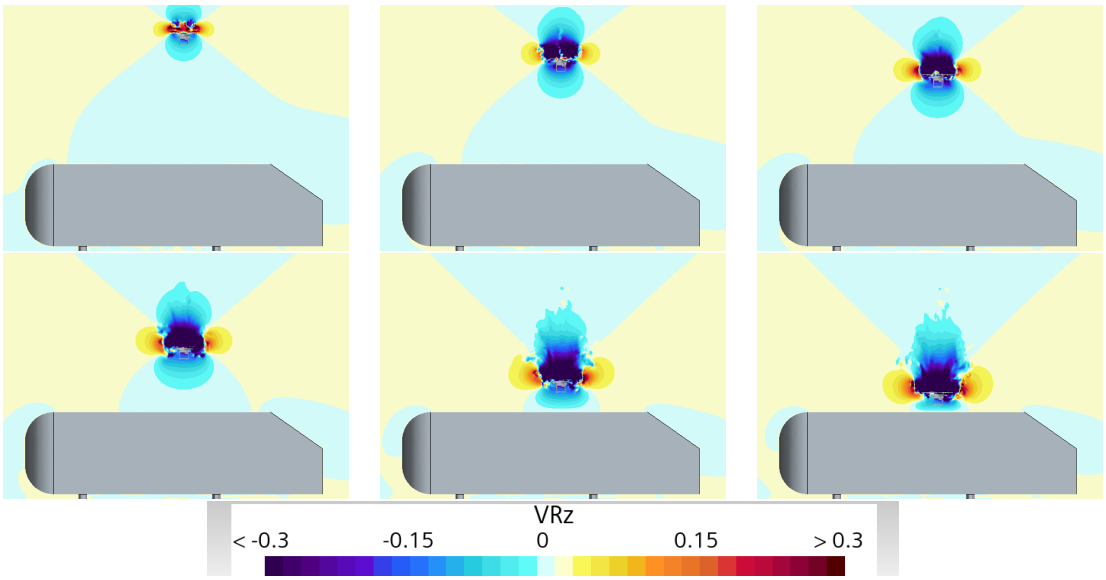

Figure 4.22: Contours of V_z for $v_d = -8$ m/s.Top row (left to right): h^*= 7.55, 5.87, and 4.87; Bottom row (left to right): h^*= 3.36, 1.26, and 0.42.

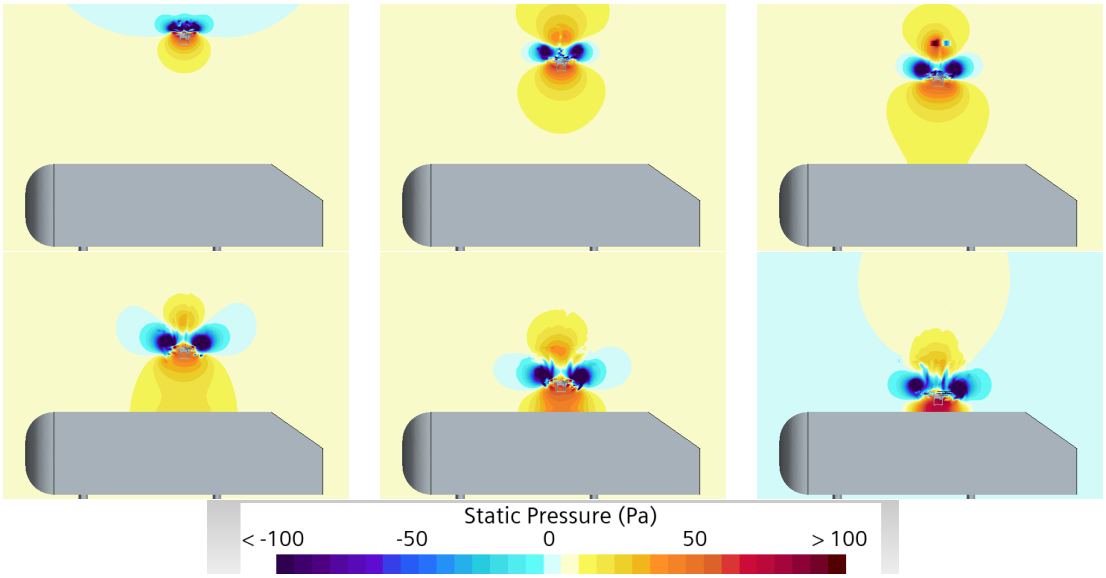

Figure 4.23: Contours of C_p for $v_d = -8$ m/s. Top row (left to right): h^*= 7.55, 5.87, and 4.87; Bottom row (left to right): h^*= 3.36, 1.26, and 0.42.

4.7 Descent Velocity of UAV at 10 m/s

A descent velocity of 10 m/s presents a markedly different aerodynamic behavior compared to lower descent velocities, such as 2 m/s and 6 m/s. At this higher velocity, unique interactions between the UAV's wake and the surrounding flow field

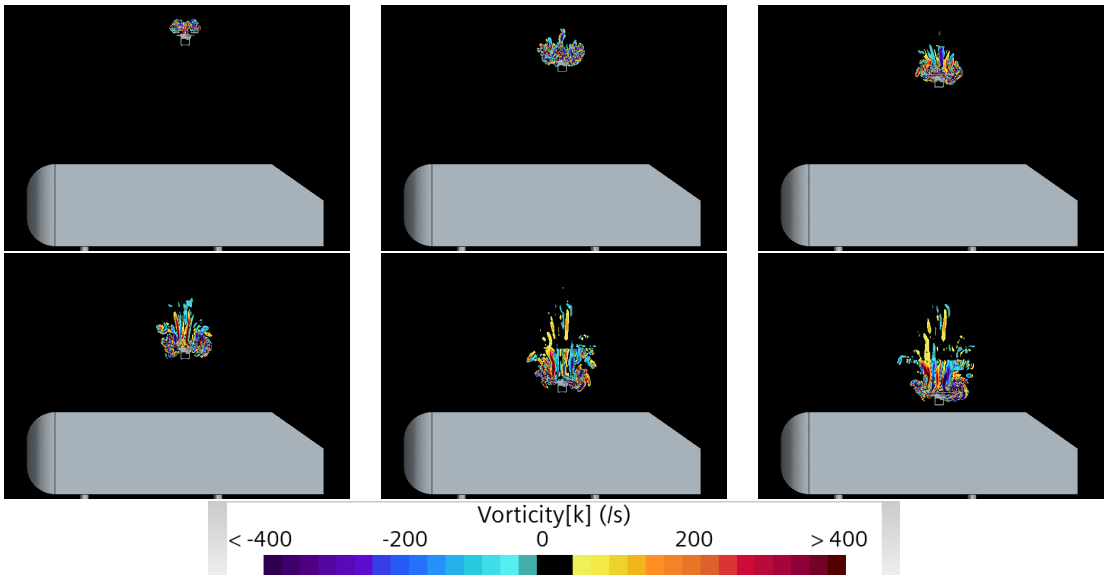

Figure 4.24: Contours of Ω for $v_d = -8$ m/s. Top row (left to right): h^*= 7.55, 5.87, and 4.87; Bottom row (left to right): h^*= 3.36, 1.26, and 0.42.

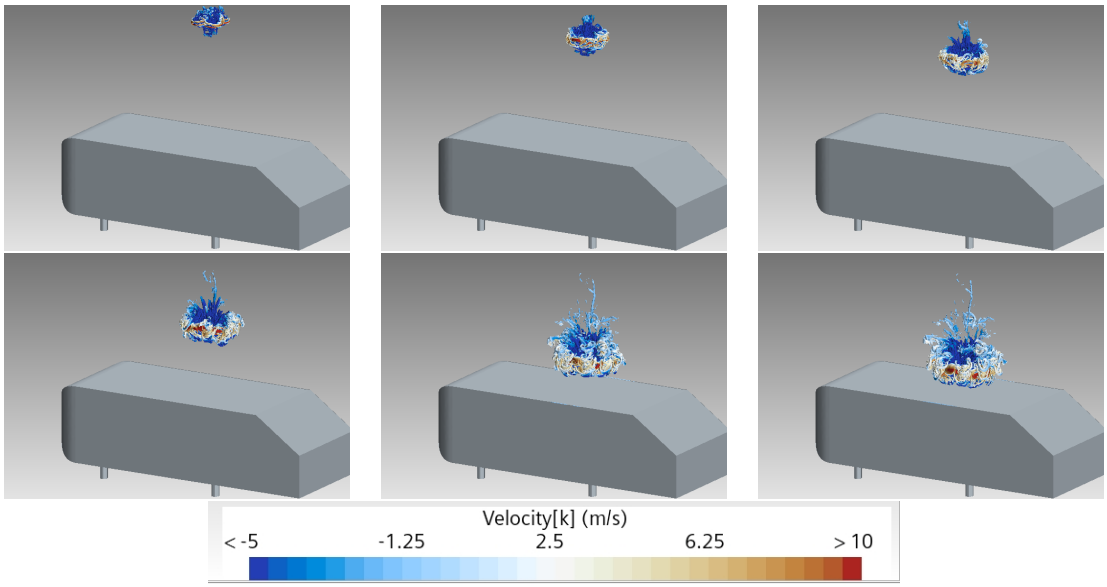

Figure 4.25: Contours of $Q-$criteria for $v_d = -8$ m/s. Top row (left to right): h^*= 7.55, 5.87, and 4.87; Bottom row (left to right): h^*= 3.36, 1.26, and 0.42.

are observed. Specifically, the wake and associated vorticity flows descend at a significantly slower rate relative to the UAV itself. This lag in aerodynamic structure descent prevents the full formation of the vortex ring state, which can contribute to UAV stability under certain conditions, as evidenced at a descent velocity of 2 m/s.

The absence of a fully developed vortex ring state at 10 m/s is particularly notable and is illustrated in subsequent figures. This phenomenon can be characterized as a "windmill brake" state. In this state, the rapid descent velocity disrupts coherent vortex structure development that typically supports stabilization mechanisms. Instead, unsteady interactions and turbulent wake dynamics dominate the aerodynamic flow field.

The windmill brake state introduces significant instability in the UAV during its descent. The rapid vertical motion amplifies aerodynamic disturbances, manifesting as high-frequency oscillations in both attitude and flight path. These oscillations are clearly reflected in frequency spectra and time-domain plots presented in later sections. The correlation between high descent velocity and increased oscillatory behavior underscores the destabilizing effects of this aerodynamic regime.

In contrast to lower descent velocities like 2 m/s, where a fully formed vortex ring state facilitates smoother aerodynamic interactions and enhanced stability, a descent velocity of 10 m/s highlights critical limitations in high-speed descents. The inability of wake structures to synchronize with the UAV's motion results in increased turbulence and reduced controllability near $h^* = 0.84$. These findings emphasize that understanding flow dynamics across varying descent rates is crucial for optimizing UAV performance and ensuring stable operation during vertical maneuvers.

4.8 Flow Dynamics at Varying Descent Speeds

This subsection investigates the influence of descent rate on the fluid-structure interaction between the UAV wake and the ground vehicle (GV) surface below. To achieve a comprehensive understanding, the flow field is analyzed at selected h^* values for all considered descent rates, including two additional velocities corresponding to v_d/v_h ratios of 0.77 and 1.54. According to [2], these ratios represent the Vortex Ring State (VRS) and the Turbulent Wake State (TWS). By incorporating these cases, the analysis seeks to further explore the interaction between the UAV wake and the

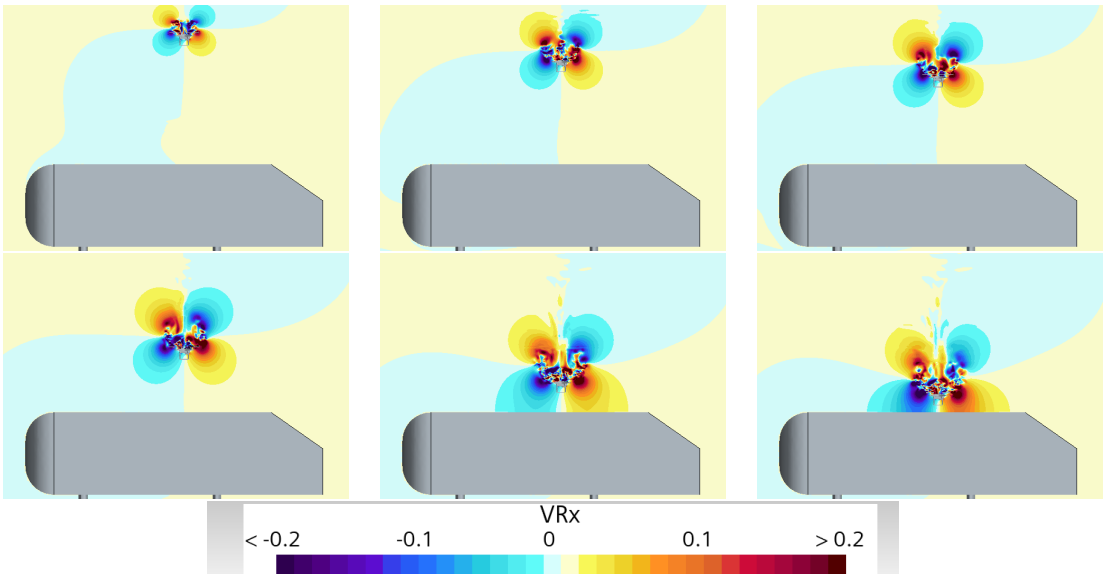

Figure 4.26: Contours of V_x for $v_d = -10$ m/s. Top row (left to right): h^*= 7.55, 5.87, and 4.87; Bottom row (left to right): h^*= 3.36, 1.26, and 0.42.

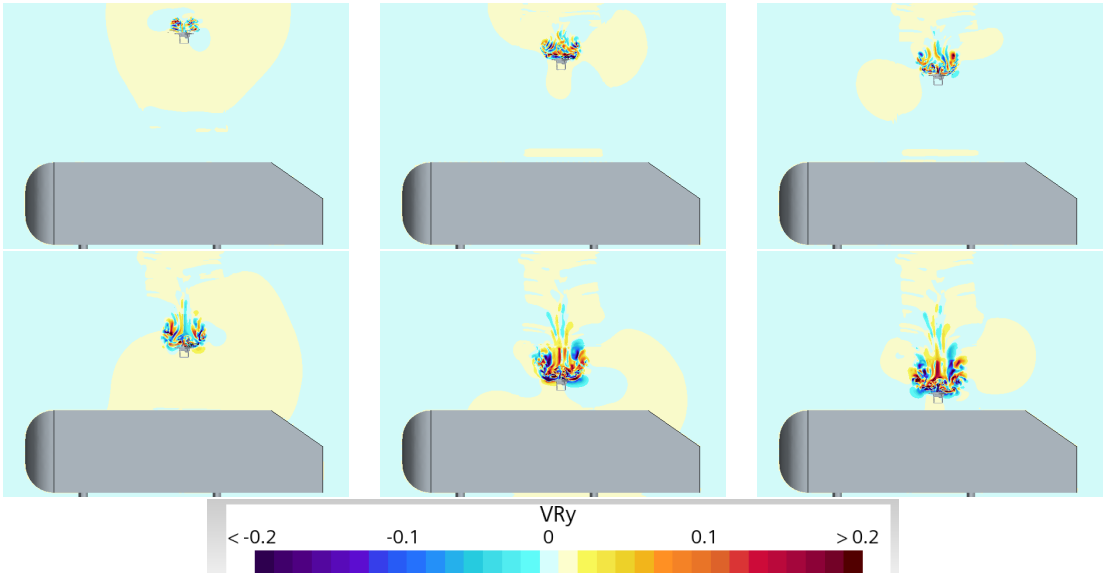

Figure 4.27: Contours of V_y for $v_d = -10$ m/s. (A–F): h^*= 7.55, 5.87, 4.87, 3.36, 1.26, and 0.42.

ground surface across a broader range of descent rates.

After conducting simulations, significant variations were observed in the fluid dynamics across different descent scenarios. The extensive dataset collected included UAV descent speeds and various scalar quantities. For comparative evaluation, three representative descent speeds- 2 m/s, 6 m/s, and 10 m/s-were selected for focused anal-

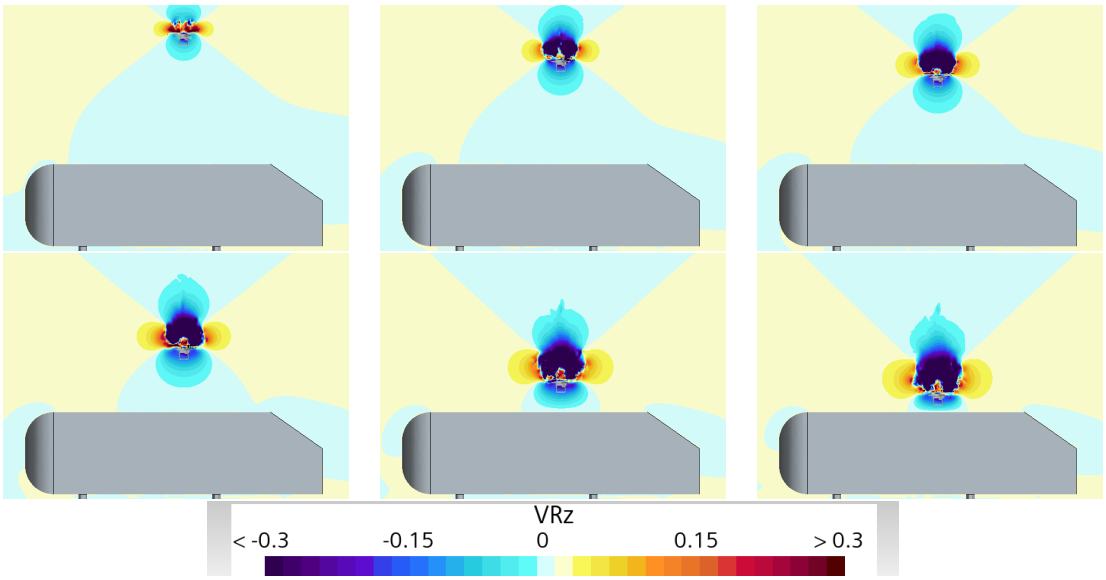

Figure 4.28: Contours of V_z for $v_d = -10$ m/s. Top row (left to right): h^*= 7.55, 5.87, and 4.87; Bottom row (left to right): h^*= 3.36, 1.26, and 0.42.

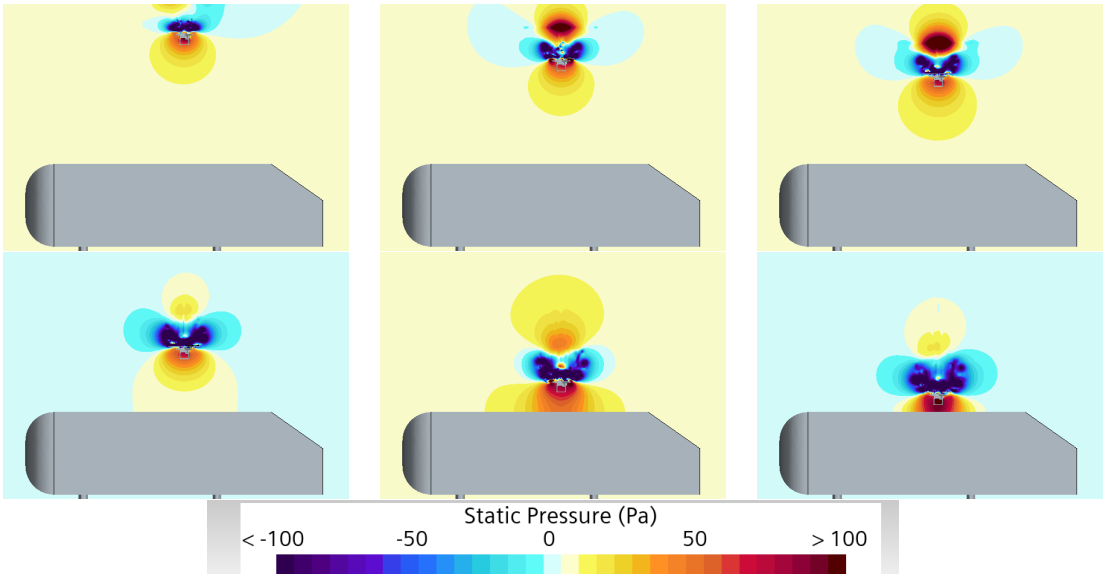

Figure 4.29: Contours of C_p for $v_d = -10$ m/s. Top row (left to right): h^*= 7.55, 5.87, and 4.87; Bottom row (left to right): h^*= 3.36, 1.26, and 0.42.

ysis. These speeds were chosen to capture distinct behaviors in vorticity dynamics and their interaction with the GV during the entire descent process, from initiation to completion.

At a descent speed of 6 m/s, notable behaviors associated with VRS were observed. At lower speeds, such as 2 m/s and 4 m/s, the vorticity fields generated beneath the

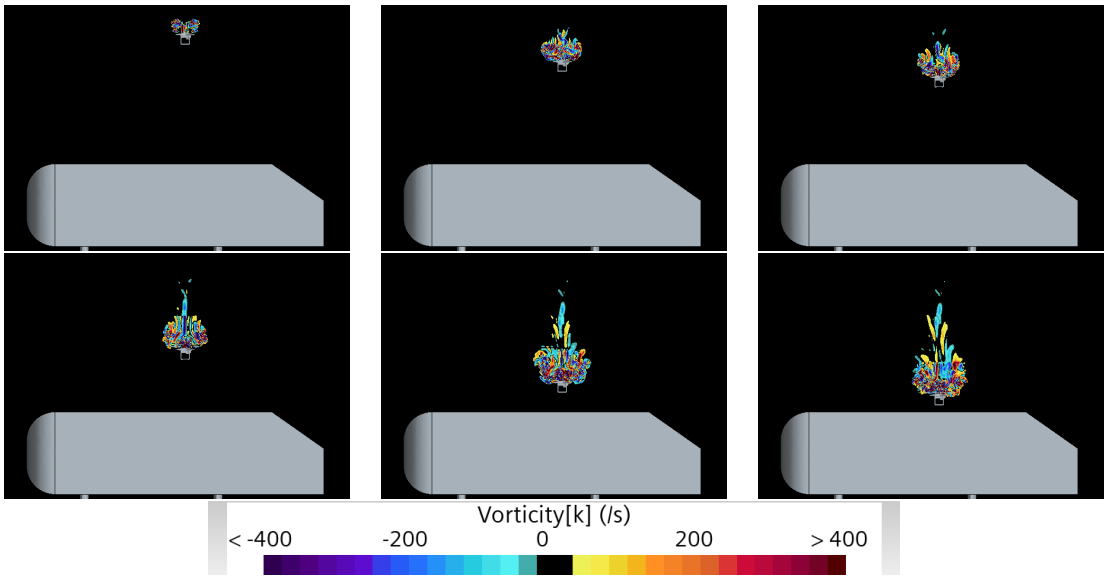

Figure 4.30: Contours of Ω for $v_d = -10$ m/s. Top row (left to right): h^*= 7.55, 5.87, and 4.87; Bottom row (left to right): h^*= 3.36, 1.26, and 0.42.

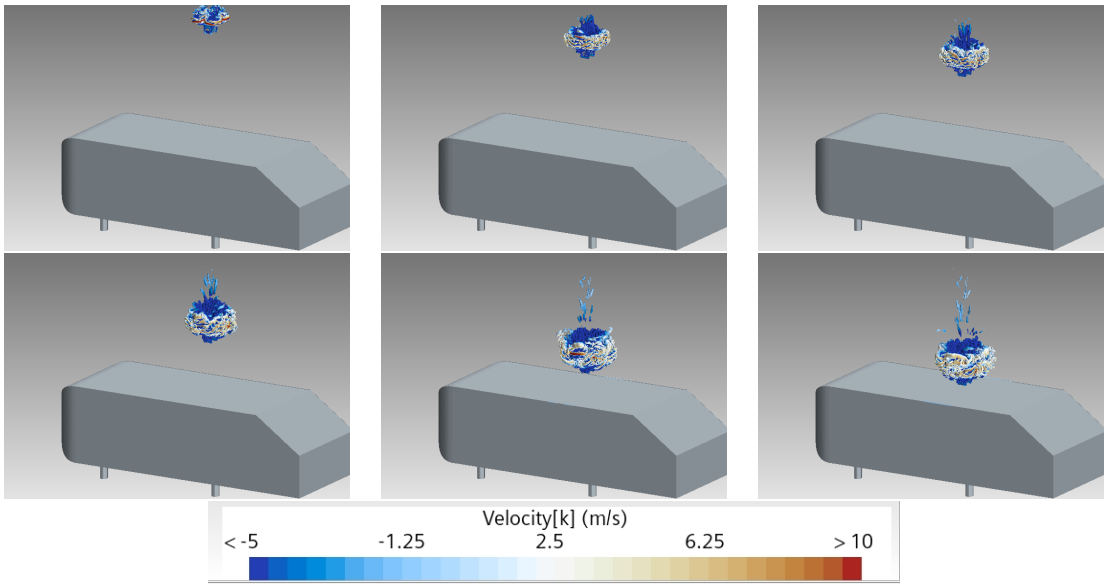

Figure 4.31: Contours of $Q-$criteria for $v_d = -10$ m/s. Top row (left to right): h^*= 7.55, 5.87, and 4.87; Bottom row (left to right): h^*= 3.36, 1.26, and 0.42.

UAV interacted with the GV before the UAV itself reached it. In contrast, at higher speeds like 8 m/s and 10 m/s, the UAV descended so rapidly that its vorticity fields remained above and behind it throughout the descent. These differences highlight how descent rate influences wake behavior and its interaction with the GV.

To provide a structured comparison across all five simulated cases, specific non-dimensional heights ($h^* = 5.87$, $h^* = 2.77$, and $h^* = 0.84$) were selected for detailed evaluation. These heights can be considered as characterizing critical phases of the UAV's landing on a GV maneuver:

- $h^* = 5.87$: The *full transition phase* where wake structures begin to form.
- $h^* = 2.77$: The *interaction phase* where vorticity fields engage with the GV.
- $h^* = 0.84$: The *final approach phase* as the UAV nears landing on the GV.

To further investigate these differences, scalar quantities such as vertical velocity (V_z), pressure coefficient (C_p), Q-criterion, and vorticity fields were analyzed in detail. The results demonstrated that at lower descent rates (2 m/s and 4 m/s), wake structures dissipated more gradually upon interacting with the GV surface. Conversely, at higher descent rates (8 m/s and 10 m/s), turbulent wake dynamics dominated due to rapid descent.

To further investigate these differences, scalar quantities such as vertical velocity (V_z), pressure coefficient (C_p), Q-criterion, and vorticity fields were analyzed in detail. The results demonstrated that at lower descent rates (2 m/s, wake structures dissipated more gradually upon interacting with the GV surface. Conversely, at higher descent rates 10 m/s), turbulent wake dynamics dominated due to rapid descent.

For future studies, particular attention will be given to aerodynamic moments-including yawing moment coefficient (C_{YM}), pitching moment coefficient (C_{PM}), and drag coefficient (C_D)-to better understand how these specific descent speeds correlate with oscillatory behaviors observed in simulations. This expanded analysis will provide deeper insights into how fluid-structure interactions evolve across varying descent rates and their implications for UAV stability during vertical maneuvers.

4.9 UAV Wake Flow Interactions with the GV at $h^* = 5.87$

In the early stages of descent, observed across all simulated velocities, the UAV begins to generate rotor-induced flow at approximately $h^* = 5.87$. This marks the onset of the descent phase, during which the UAV's aerodynamic wake begins to interact with its surrounding environment. At this critical juncture, all simulations transition into the descent phase, with the wake behavior varying significantly depending on the descent velocity.

At lower descent speeds, such as 2 m/s, the wake initiates its descent earlier compared to higher velocities like 10 m/s. This phenomenon is clearly illustrated in Figures 4.32, 4.33, and 4.34, which depict scalar fields for the velocity components (V_x, V_y, and V_z) at $h^* = 5.87$. In these figures, subfigures on the top row, from left to right, correspond to descent rates of 2, 4, and 6 m/s, respectively, while those on the bottom row, also from left to right, represent descent rates of 8 and 10 m/s, respectively. These figures demonstrates how the UK wake flow structure evolves as a function of descent velocity.

Additional scalar fields are presented in Figures 4.35, 4.36, and 4.37, which provide analogous comparisons for pressure coefficient (C_p), vorticity magnitude, and Q-criteria. Notably, at a descent speed of 2 m/s, a distinct vorticity flow is observed significantly earlier than at other speeds. This early formation of vorticity fields suggests a stronger coupling between the UAV's wake and its surrounding flow at lower speeds.

At higher descent velocities, such as 8 m/s and 10 m/s, a different dynamic emerges. The UAV progresses faster than its wake, resulting in unique wake behaviors. For instance, while at lower speeds the wake descends in close proximity to the UAV, at higher speeds it lags behind and aligns more horizontally relative to the UAV's trajectory. A transition in wake behavior is particularly evident between 6 m/s and 8 m/s. Within this range, the wake shifts from a predominantly descending pattern

to one characterized by increased horizontal alignment. Although the wake profiles at 6 m/s and 8 m/s appear relatively similar, a more pronounced distinction becomes apparent at 8 m/s and 10 m/s, where the wake closely follows the UAV during its rapid descent.

These observations underscore how increasing descent velocity alters the interaction between the UAV and its aerodynamic wake. The mechanisms underlying these differences will be examined in greater detail in subsequent sections to better understand how such variations impact UAV stability and performance during vertical maneuvers.

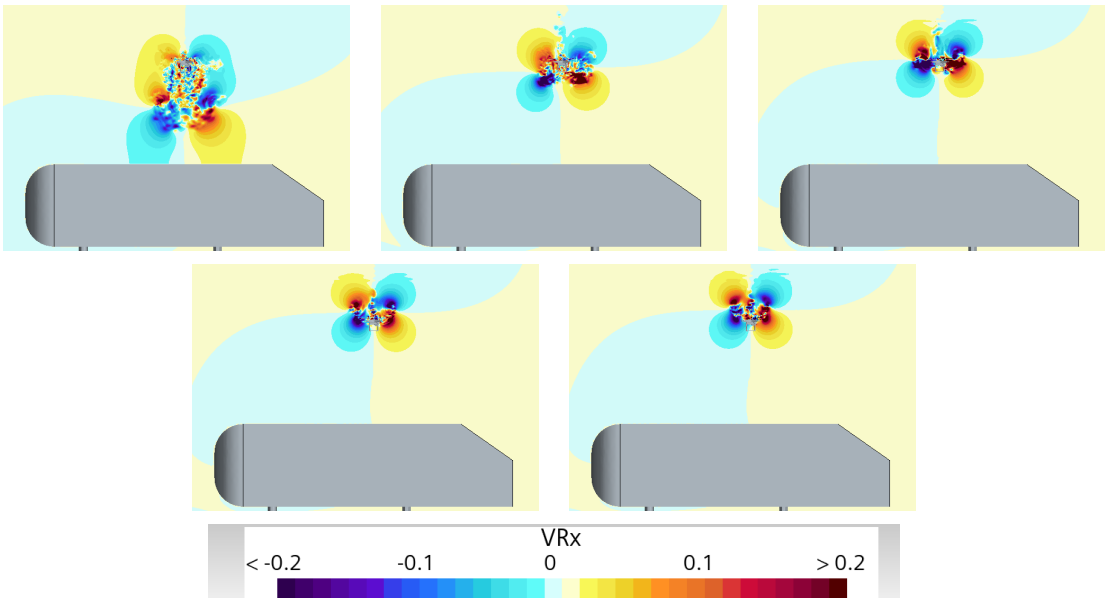

Figure 4.32: Contours of V_x corresponding the various descent rates at h^*= 5.87. Top row (left to right): $-v_d$ = 2, 4, and 6 m/s; Bottom row (left to right): $-v_d$ = 8 and 10 m/s.

4.10 UAV Wake Flow Interactions with the GV at $h^* = 2.77$

The results presented in Figures 4.38 and 4.41 for the case at $h^* = 2.77$ reaffirm the observations made at the higher height of $h^* = 5.87$. At this reduced separation distance, the influence of ground effect due to the presence of the GV surface becomes significantly more pronounced.

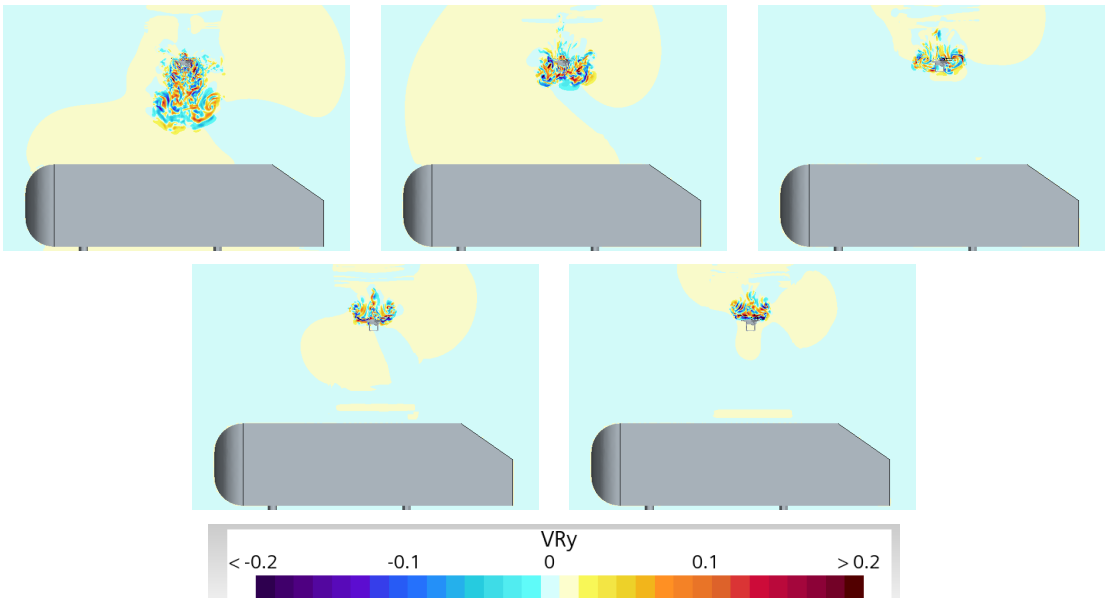

Figure 4.33: Contours of V_y corresponding the various descent rates at h^*= 5.87. Top row (left to right): $-v_d$ = 2, 4, and 6 m/s; Bottom row (left to right): $-v_d$ = 8 and 10 m/s.

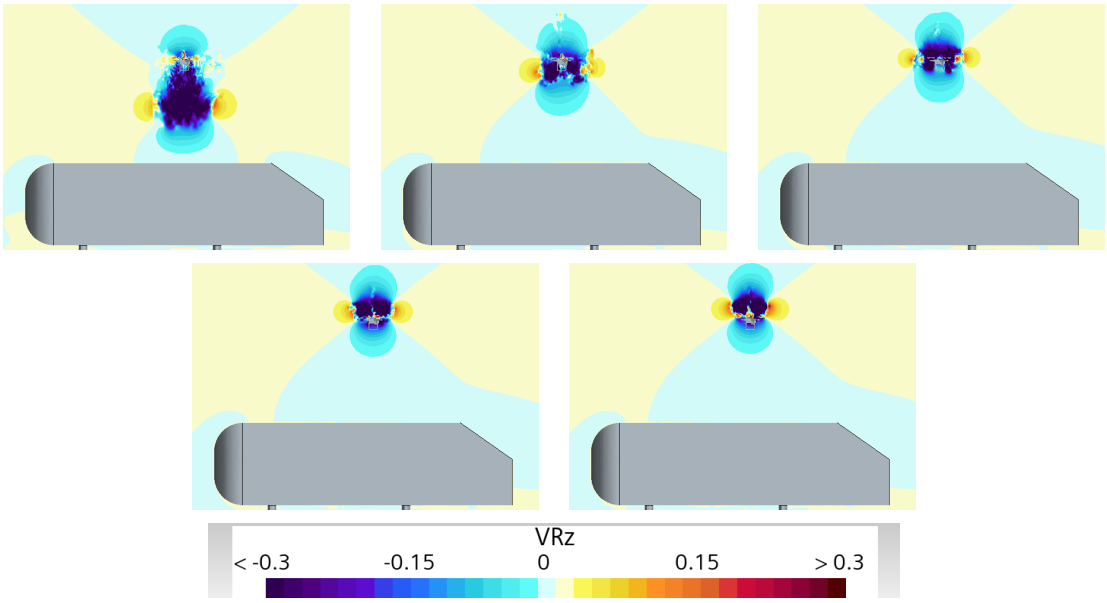

Figure 4.34: Contours of V_z corresponding the various descent rates at h^*= 5.87. Top row (left to right): $-v_d$ = 2, 4, and 6 m/s; Bottom row (left to right): $-v_d$ = 8 and 10 m/s.

Specifically, the V_x velocity component begins to exhibit clear interactions with the GV surface for descent speeds up to 6 m/s. This highlights the increasing dominance of fluid-structure interactions as the UAV approaches closer to the ground. In

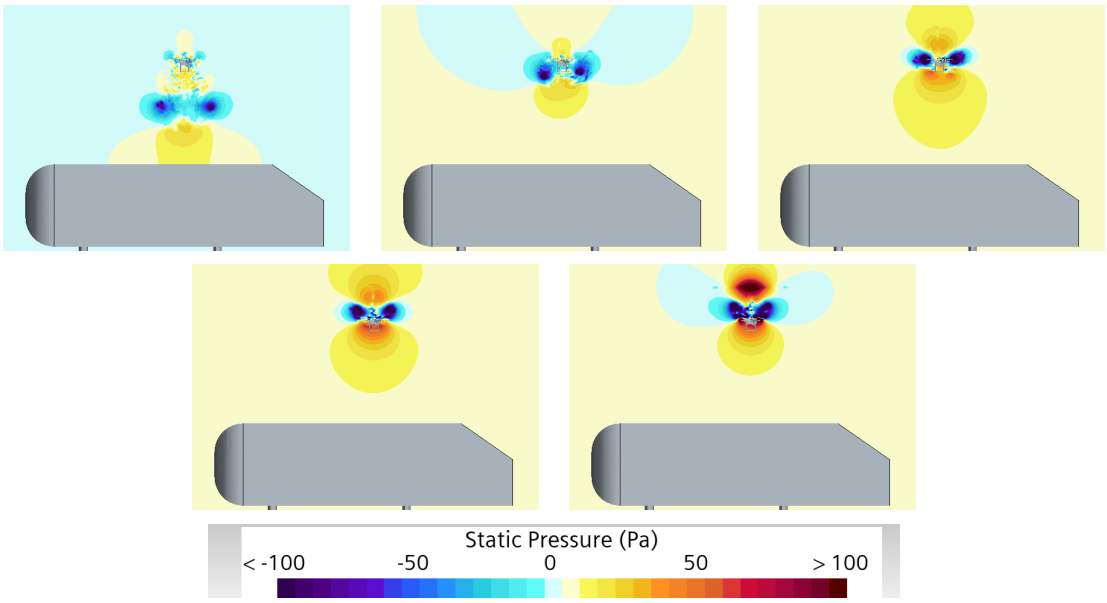

Figure 4.35: Contours of C_p corresponding the various descent rates at h^*= 5.87. Top row (left to right): $-v_d$ = 2, 4, and 6 m/s; Bottom row (left to right): $-v_d$ = 8 and 10 m/s.

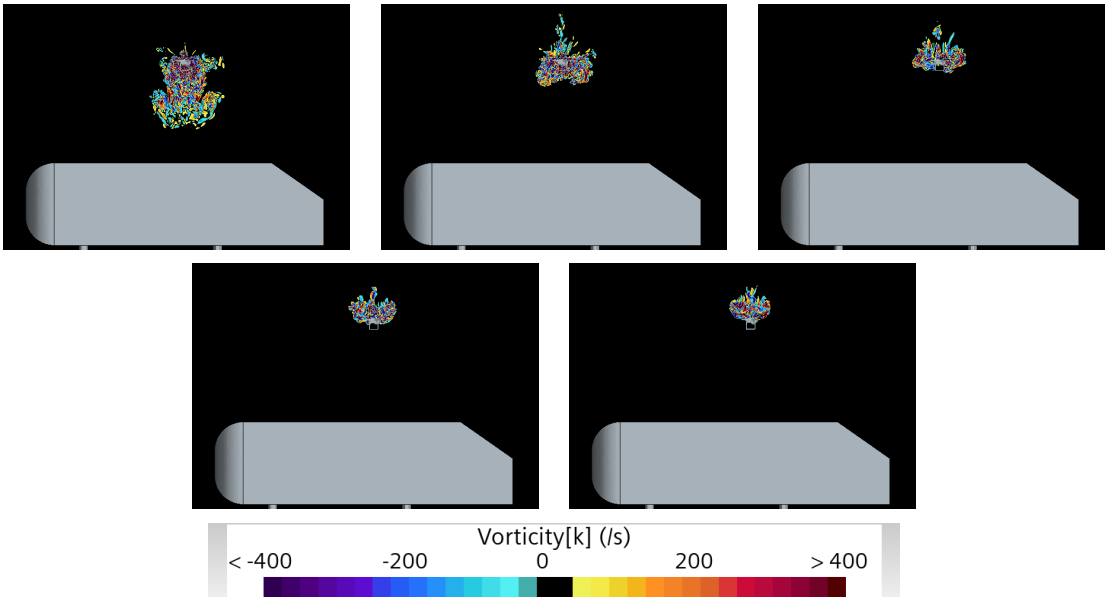

Figure 4.36: Contours of Ω corresponding the various descent rates at h^*= 5.87. Top row (left to right): $-v_d$ = 2, 4, and 6 m/s; Bottom row (left to right): $-v_d$ = 8 and 10 m/s.

contrast, the pressure field shows substantial changes across all descent rates investigated, regardless of speed. This observation suggests that the aerodynamic pressure distribution around the UAV becomes increasingly sensitive to the proximity of the

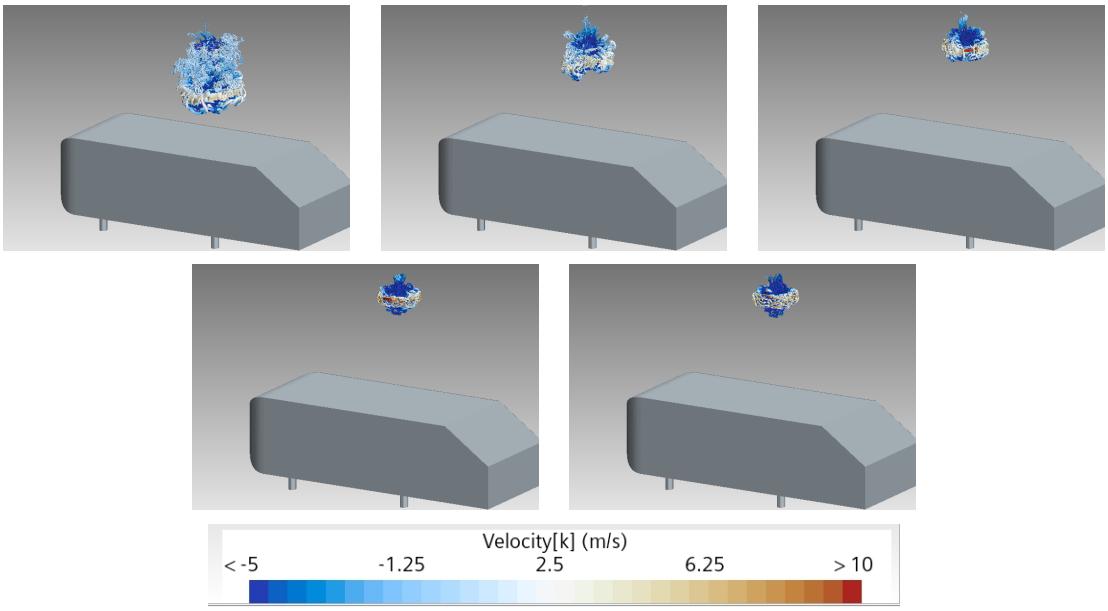

Figure 4.37: Contours of $Q-$criteria corresponding the various descent rates at $h^*=$ 5.87. Top row (left to right): $-v_d$ = 2, 4, and 6 m/s; Bottom row (left to right): $-v_d$ = 8 and 10 m/s.

GV as the separation distance decreases.

Unlike the V_x velocity component, which demonstrates ground effect interactions only at specific descent speeds, the pressure field serves as a consistent indicator of the ground's influence at this height. The results suggest that while velocity components such as V_x may selectively reflect interactions based on descent rate, the pressure field reliably captures the growing impact of ground effect at lower h^* values.

These findings reinforce two key points:

- Selective Velocity Component Interactions:** The behavior of velocity components like V_x is more dependent on descent rate and may not consistently reflect ground effect interactions across all speeds.

- Pressure Field as a Reliable Indicator:** The pressure field provides a robust and consistent measure of ground effect influence as separation distance decreases, irrespective of descent velocity.

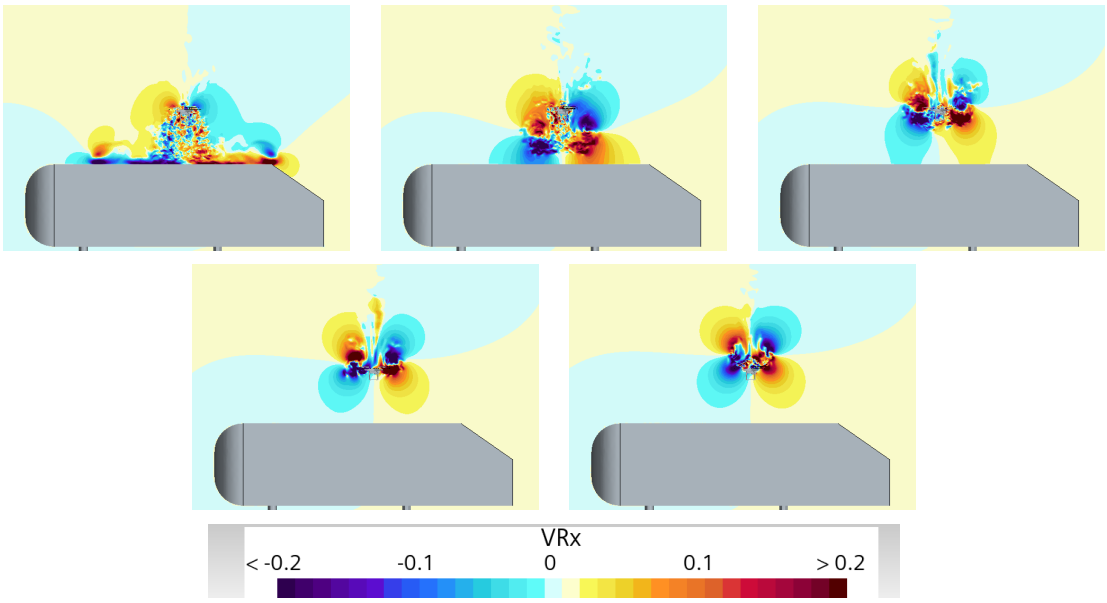

Figure 4.38: Contours of V_x corresponding the various descent rates at h^*= 2.77. Top row (left to right): $-v_d$ = 2, 4, and 6 m/s; Bottom row (left to right): $-v_d$ = 8 and 10 m/s.

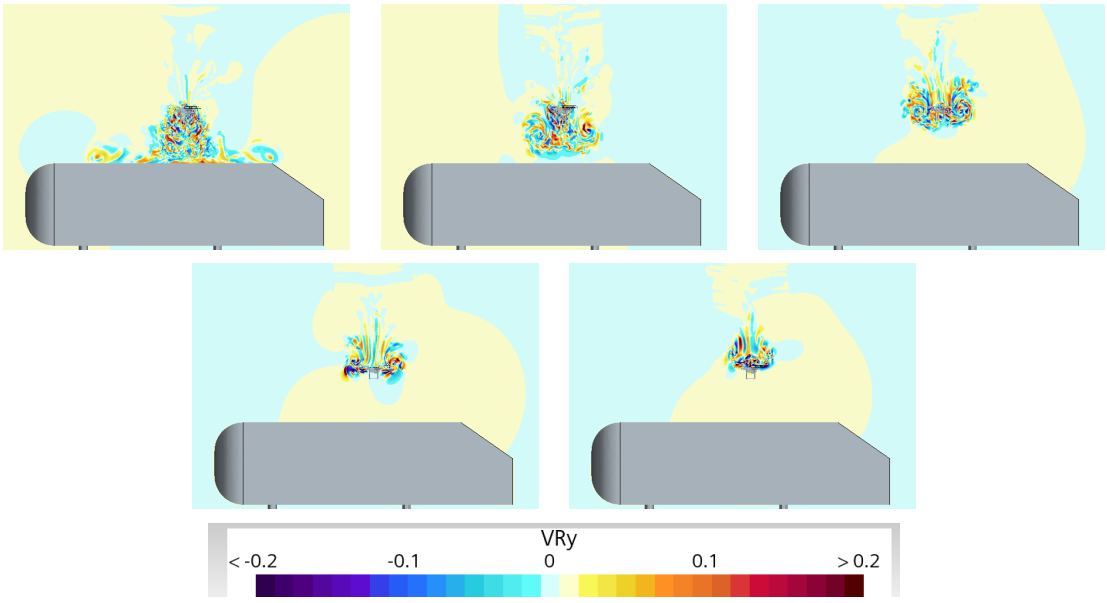

Figure 4.39: Contours of V_y corresponding the various descent rates at h^*= 2.77. Top row (left to right): $-v_d$ = 2, 4, and 6 m/s; Bottom row (left to right): $-v_d$ = 8 and 10 m/s.

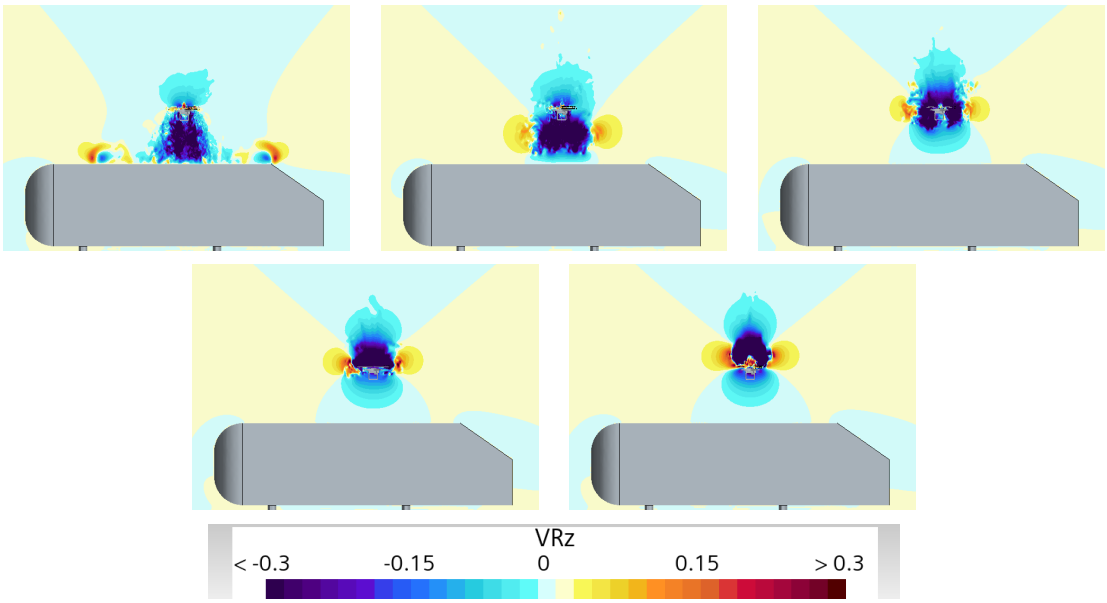

Figure 4.40: Contours of V_z corresponding the various descent rates at h^*= 2.77. Top row (left to right): $-v_d$ = 2, 4, and 6 m/s; Bottom row (left to right): $-v_d$ = 8 and 10 m/s.

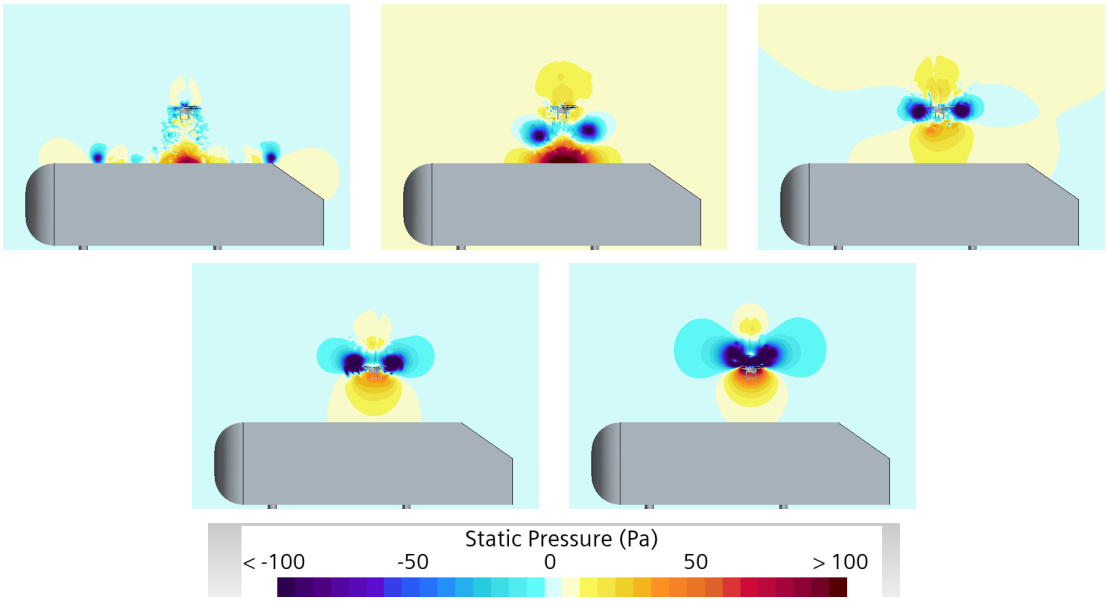

Figure 4.41: Contours of C_p for corresponding the various descent rates at h^*= 2.77. Top row (left to right): $-v_d$ = 2, 4, and 6 m/s; Bottom row (left to right): $-v_d$ = 8 and 10 m/s.

4.11 UAV Wake Flow Interactions with the GV at $h^* = 0.84$

The final non-dimensional height (h^*) analyzed to investigate the interaction between the UAV wake flow and the ground vehicle (GV) is $h^* = 0.84$. At this height,

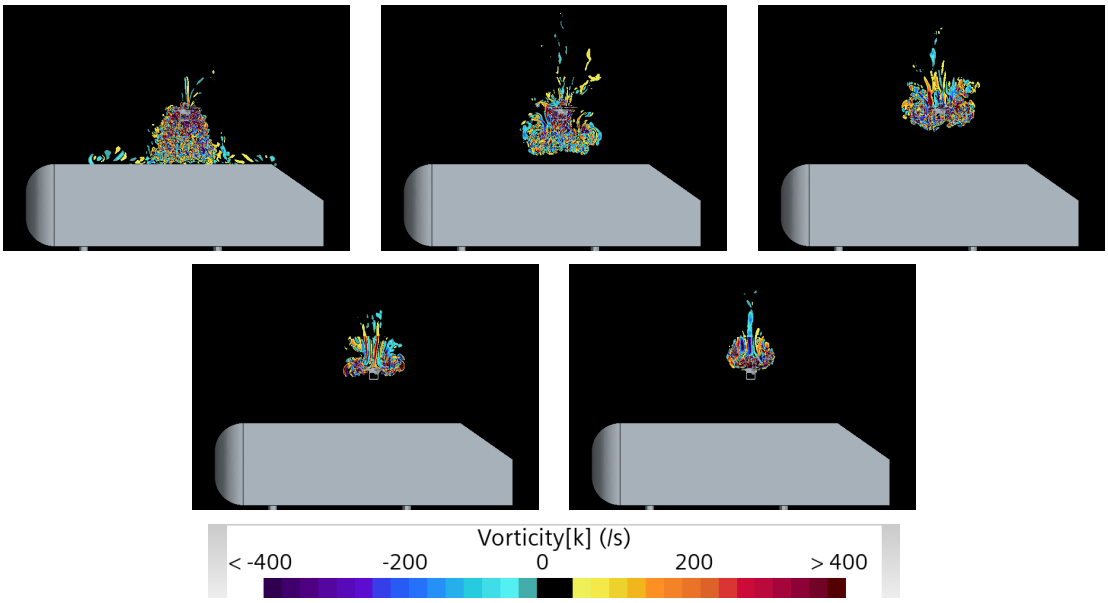

Figure 4.42: Contours of Ω corresponding the various descent rates at h^*= 2.77. Top row (left to right): $-v_d$ = 2, 4, and 6 m/s; Bottom row (left to right): $-v_d$ = 8 and 10 m/s.

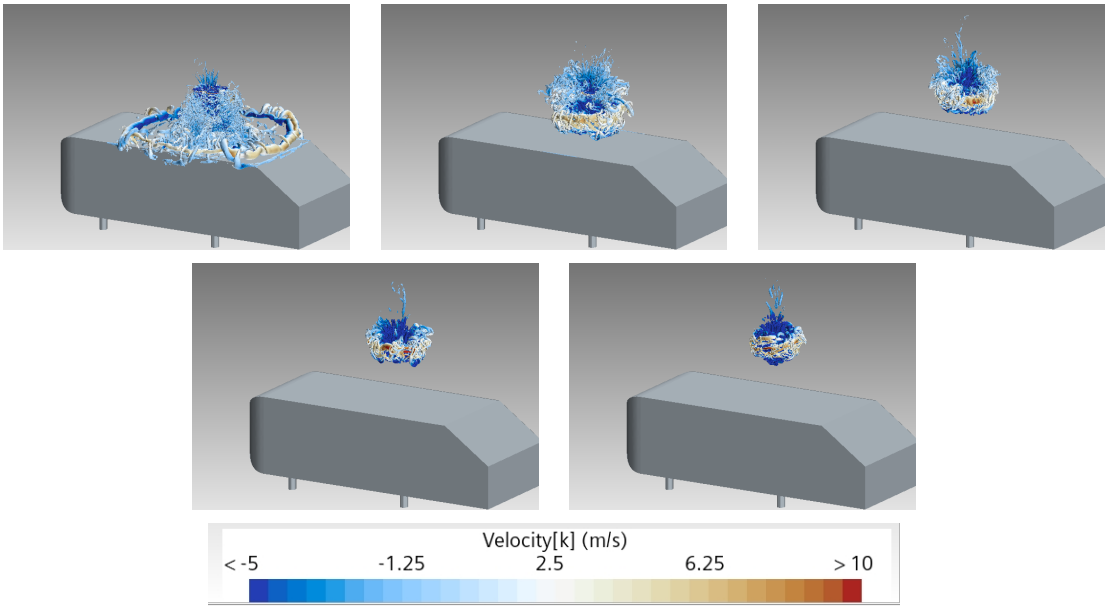

Figure 4.43: Contours of $Q-$criteria corresponding the various descent rates at h^*= 2.77. Top row (left to right): $-v_d$ = 2, 4, and 6 m/s; Bottom row (left to right): $-v_d$ = 8 and 10 m/s.

the bottom of the UAV is approximately one rotor diameter above the GV. This specific separation distance was selected because it represents a critical phase where the vorticity fields from lower descent rates begin to dissipate, while those from higher

descent rates remain active and initiate contact with the GV surface.

Similar to observations made at $h^* = 2.77$, most of the vorticity fields at $h^* = 0.84$ are significantly ahead of the UAV's descent velocity. However, due to the reduced height, the wake and vorticity fields do not expand or dissipate across the UAV as they do at earlier phases of descent with slower velocities. This behavior highlights a transition in wake dynamics as the UAV approaches closer to the GV. Scalar field analyses suggest that for higher descent velocities, the wake and flow fields have moved beyond the vortex ring state (VRS) and now exhibit characteristics consistent with the windmill brake state (WBS).

- Ground Effect Across All Descent Rates: At $h^* = 0.84$, ground effect becomes evident for all descent rates, irrespective of the descent velocity (v_d). This effect is most pronounced in the pressure field, followed by noticeable changes in the V_x velocity field.

- Formation of a Ring-Like Vortex Structure:A prominent, large ring-like vortex structure emerges on the upper surface of the GV. This phenomenon is similar to what was observed for $v_d = 2\,\mathrm{m/s}$ at $h^* = 2.77$. The formation and dynamics of this ring-like vortex are complex and not yet fully understood, leaving significant opportunities for further investigation in future studies.

- These findings underscore how wake dynamics evolve as a function of both descent velocity and proximity to the GV. The interplay between ground effect, vorticity field behavior, and wake structure formation at this critical height provides valuable insights into UAV-GV interactions during vertical maneuvers.

4.12 Comparing the Flow Dynamics at Descent Velocities of 2, 6, and 10 m/s

Following an evaluation of descent rates at various non-dimensional heights, h^*, the velocities of 2, 6, and 10 m/s are chosen as the best candidates for detailed comparison and further investigation. For this purpose, scalar plots of key aerodynamic

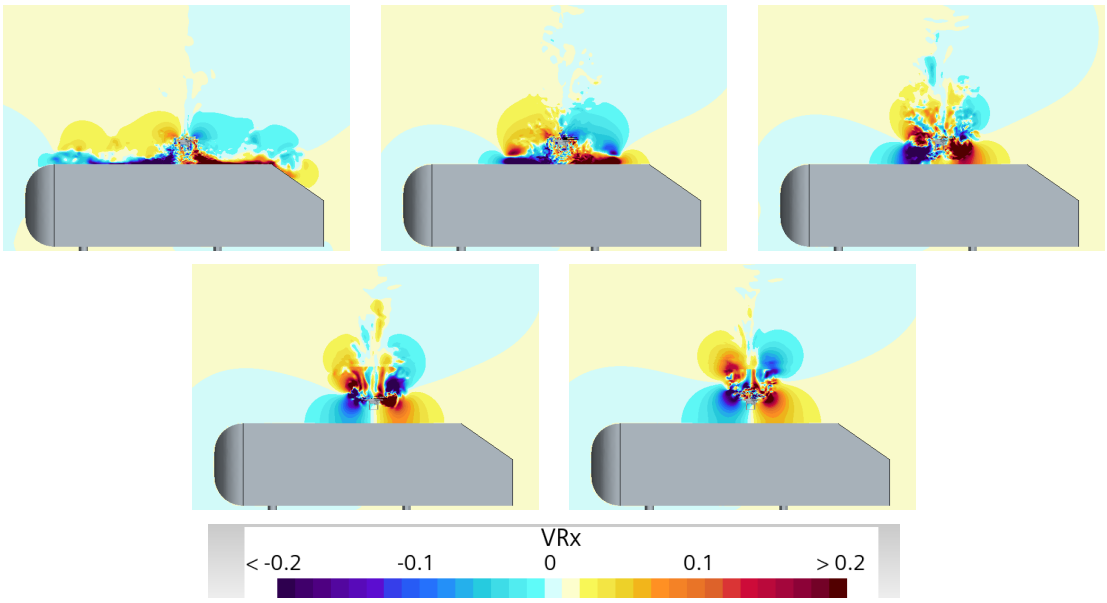

Figure 4.44: Contours of V_x corresponding the various descent rates at h^*= 0.84. Top row (left to right): $-v_d$ = 2, 4, and 6 m/s; Bottom row (left to right): $-v_d$ = 8 and 10 m/s.

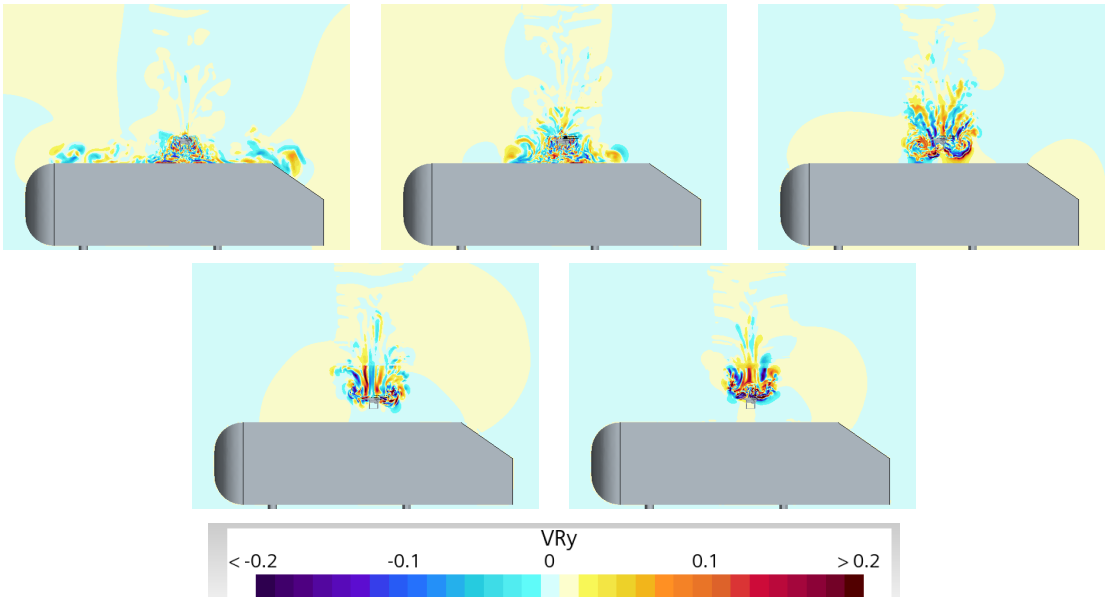

Figure 4.45: Contours of V_y corresponding the various descent rates at h^*= 0.84. Top row (left to right): $-v_d$ = 2, 4, and 6 m/s; Bottom row (left to right): $-v_d$ = 8 and 10 m/s.

parameters are shown, including velocity components (V_x, V_y, V_z), pressure coefficient, and Q-criteria. These scalar plots are organized in a structured layout where each column corresponds to one of the selected velocities (2, 6, and 10 m/s), and each

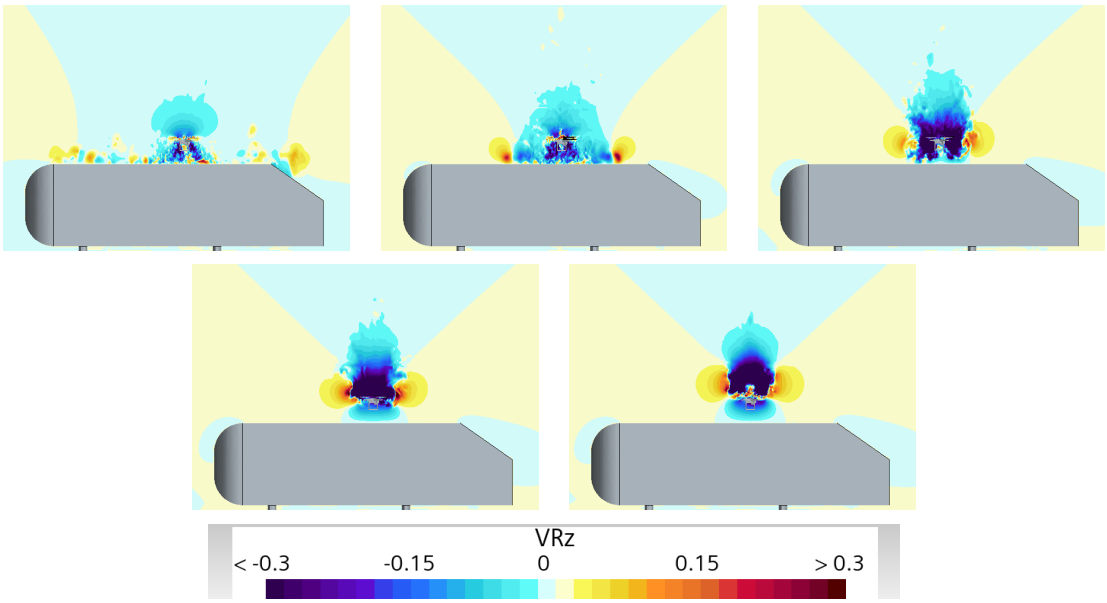

Figure 4.46: Contours of V_z corresponding the various descent rates at h^*= 0.84. Top row (left to right): $-v_d$ = 2, 4, and 6 m/s; Bottom row (left to right): $-v_d$ = 8 and 10 m/s.

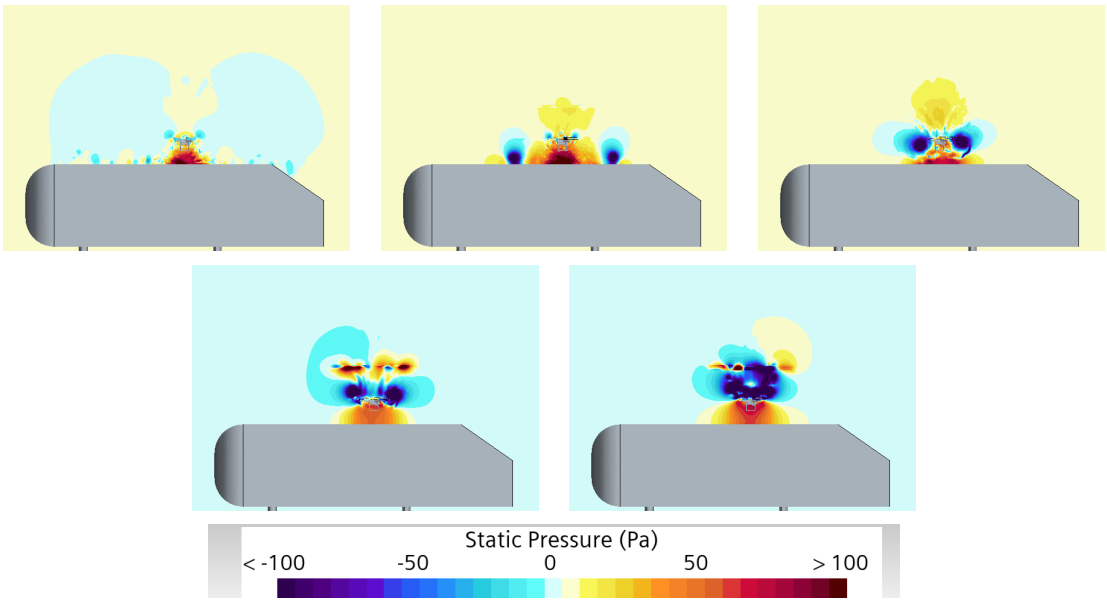

Figure 4.47: Contours of C_p corresponding the various descent rates at h^*= 0.84. Top row (left to right): $-v_d$ = 2, 4, and 6 m/s; Bottom row (left to right): $-v_d$ = 8 and 10 m/s.

row represents a distinct h^* value. The h^* values are categorized as follows:

- A: $h^* = 7.55$

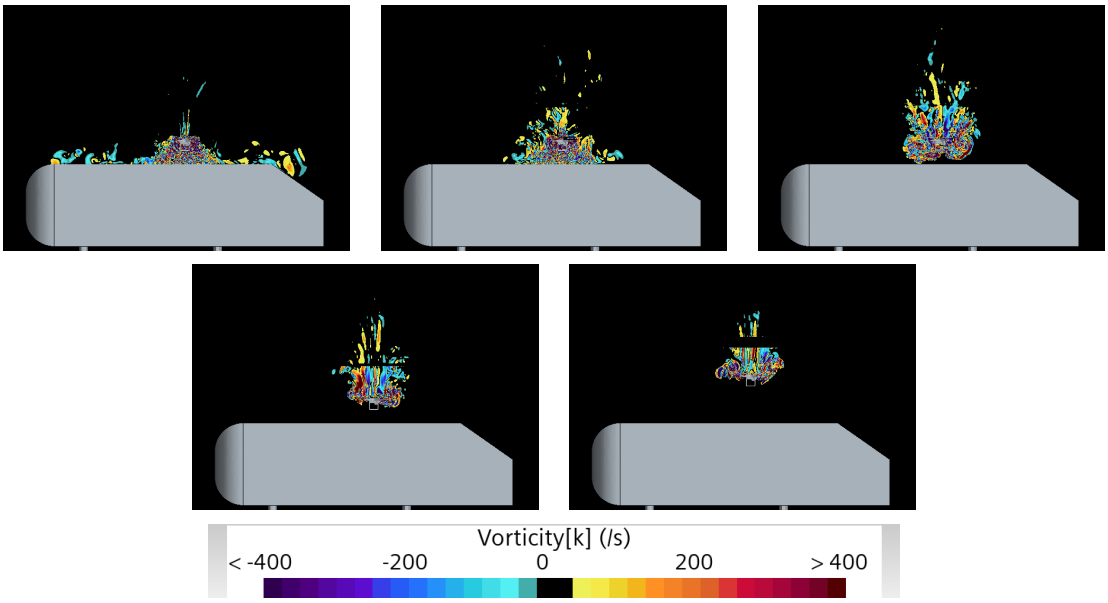

Figure 4.48: Contours of Ω corresponding the various descent rates at h^*= 0.84. Top row (left to right): $-v_d$ = 2, 4, and 6 m/s; Bottom row (left to right): $-v_d$ = 8 and 10 m/s.

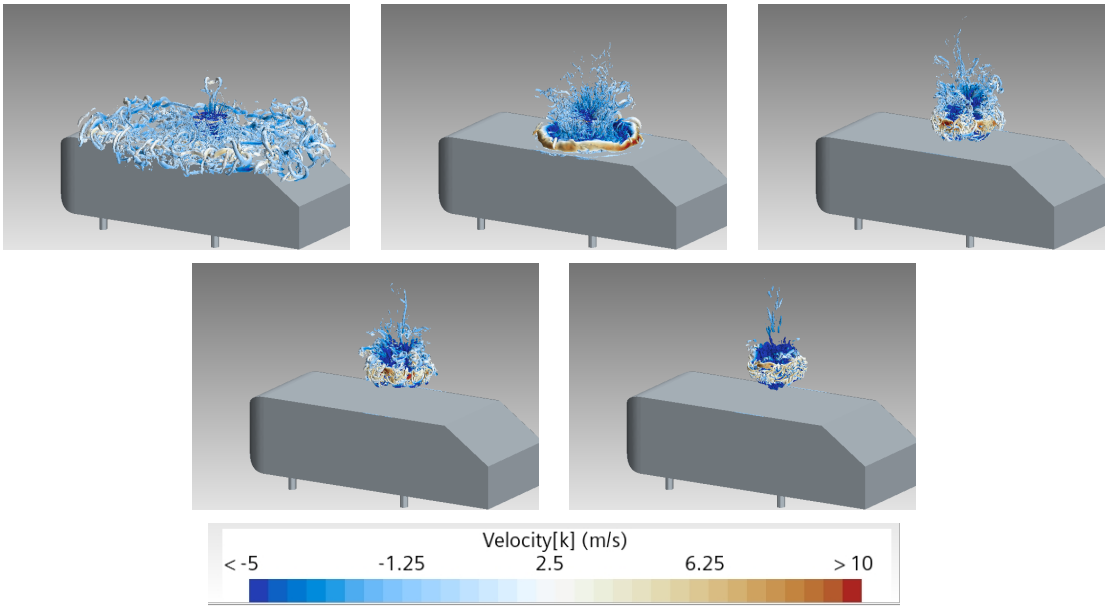

Figure 4.49: Contours of $Q-$criteria corresponding the various descent rates at h^*= 0.84. Top row (left to right): $-v_d$ = 2, 4, and 6 m/s; Bottom row (left to right): $-v_d$ = 8 and 10 m/s.

- B: $h^* = 5.87$
- C: $h^* = 3.36$

- D: $h^* = 0.84$
- E: $h^* \approx 0.02$

While descent rates of 4 and 8 m/s offer smoother transitions across all five height levels, the descent rate of 6 m/s is particularly significant as it distinctly enters and resides within the VRS. This phenomenon is critical for understanding the aerodynamic behavior during descent, as it highlights the onset of instability caused by recirculating flow patterns. By focusing on these velocities and height levels, the most relevant flow characteristics are captured providing deeper insights into the transition to VRS and its associated aerodynamic effects.

The results presented for descent velocities $v_d = 2\,\mathrm{m/s}$, $v_d = 6\,\mathrm{m/s}$, and $v_d = 10\,\mathrm{m/s}$ provide a detailed understanding of how wake-ground interactions evolve with increasing descent speed. The velocity components V_x, V_y, and V_z exhibit distinct interaction patterns across these descent rates, revealing the critical influence of descent velocity on the wake dynamics and fluid-structure interactions with the ground vehicle (GV).

At $v_d = 2\,\mathrm{m/s}$, the V_x velocity field exhibits significant dissipation along the Ahmed body. The slower descent allows for greater wake expansion and interaction with the GV surface over a broader area. This behavior aligns with the NWS, where reduced wake energy facilitates widespread aerodynamic effects across the GV. Unlike higher velocities, where interactions are concentrated near specific regions, at $v_d = 2\,\mathrm{m/s}$, these interactions are more evenly distributed along both lateral (V_y) and vertical (V_z) directions.

At $v_d = 6\,\mathrm{m/s}$, the V_x velocity component begins to exhibit more pronounced interactions with the GV surface. The wake starts to expand laterally and vertically, resulting in moderate coupling with the GV. This intermediate descent velocity corresponds to a transitional regime such as the VRS, where both wake confinement and dispersion contribute to fluid-structure interactions. The increased lateral spread of V_x at this speed enhances its influence on aerodynamic forces acting on the GV.

At $v_d = 10\,\mathrm{m/s}$, the V_x velocity field shows a tightly confined wake that closely follows the UAV without significant lateral or vertical dispersion. This behavior indicates that at higher descent velocities, the UAV operates in a state resembling the WBS, where the wake is highly energetic and remains aligned with the UAV trajectory. The rapid descent limits wake expansion and interaction with the GV surface, resulting in localized but intense aerodynamic effects near the UAV's path. Minimal dissipation of the wake occurs along the Ahmed body, as most of the flow energy remains concentrated behind the UAV.

The lateral velocity component (V_y) plays a critical role in determining how wake dynamics propagate horizontally across the GV surface. At $v_d = 2\,\mathrm{m/s}$, V_y reaches its maximum influence as slower wake propagation allows for significant lateral dispersion, leading to broader aerodynamic coupling with the GV. At $v_d = 6\,\mathrm{m/s}$, however, V_y begins to intensify as lateral interactions become more prominent. This marks a transitional phase where horizontal spreading of aerodynamic effects becomes noticeable. At $v_d = 10\,\mathrm{m/s}$, V_y remains relatively weak due to limited lateral dispersion of the wake; most of its energy is concentrated directly behind the UAV.

The vertical velocity component (V_z) reflects how wake dynamics propagate vertically towards or away from the GV surface. At $v_d = 2\,\mathrm{m/s}$, vertical dispersion dominates; V_z exhibits widespread interaction with the Ahmed body as slower descent speeds allow for greater vertical propagation of wake-induced forces. At $v_d = 6\,\mathrm{m/s}$, vertical interactions intensify as V_z begins to spread more significantly towards the GV surface, contributing to enhanced fluid-structure coupling. At $v_d = 10\,\mathrm{m/s}$, V_z remains confined near the UAV due to limited vertical expansion of the wake. This results in strong but localized downward aerodynamic forces acting on specific regions of the GV.

The comparison of velocity components across these three descent velocities highlights distinct trends:

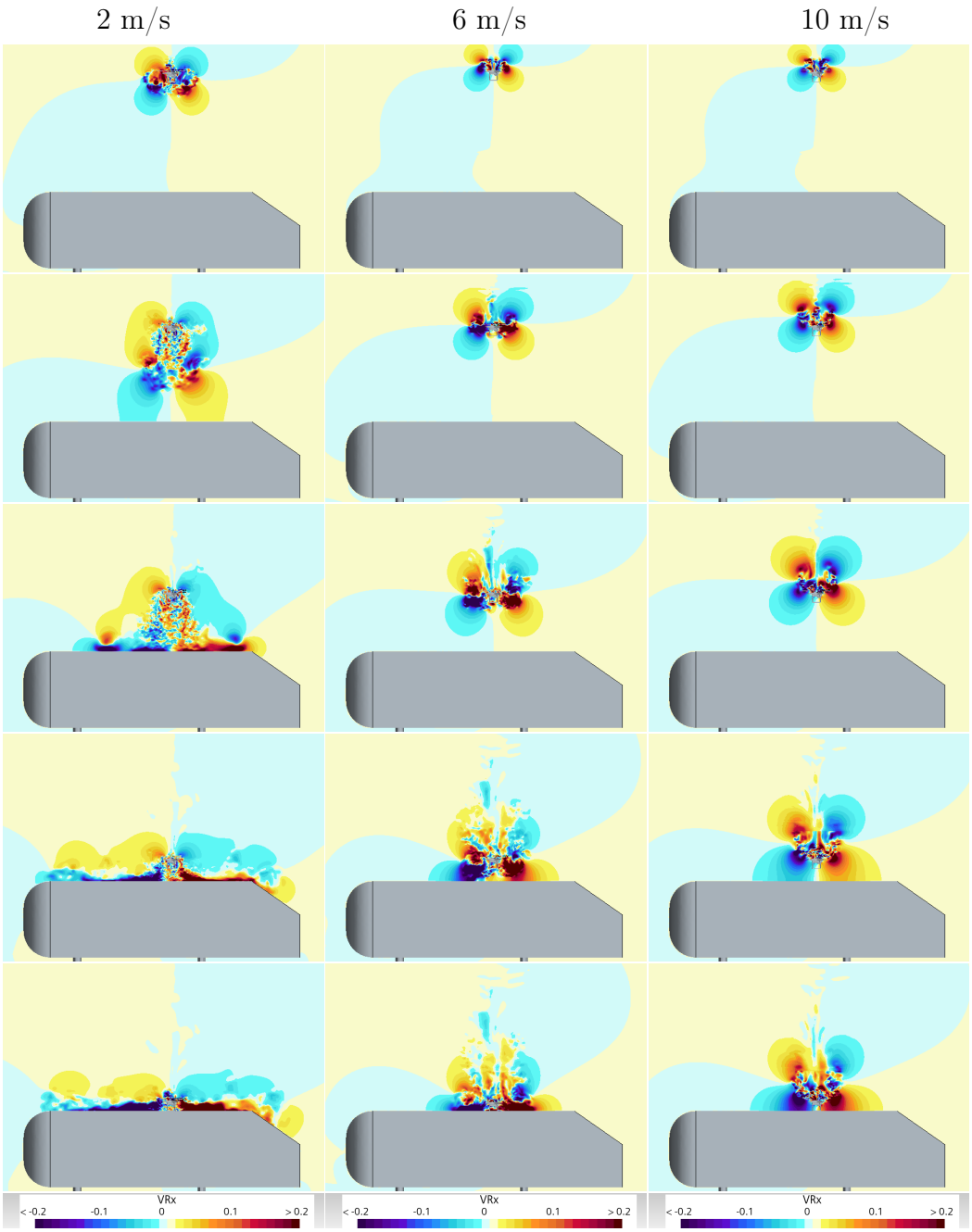

Figure 4.50: Comparison of V_x^* contours for descent velocities of 2, 6, and 10 m/s at nondimensional heights $h^* = 7.55$, 5.87, 3.36, 0.84, and 0.02 (arranged from top to bottom).

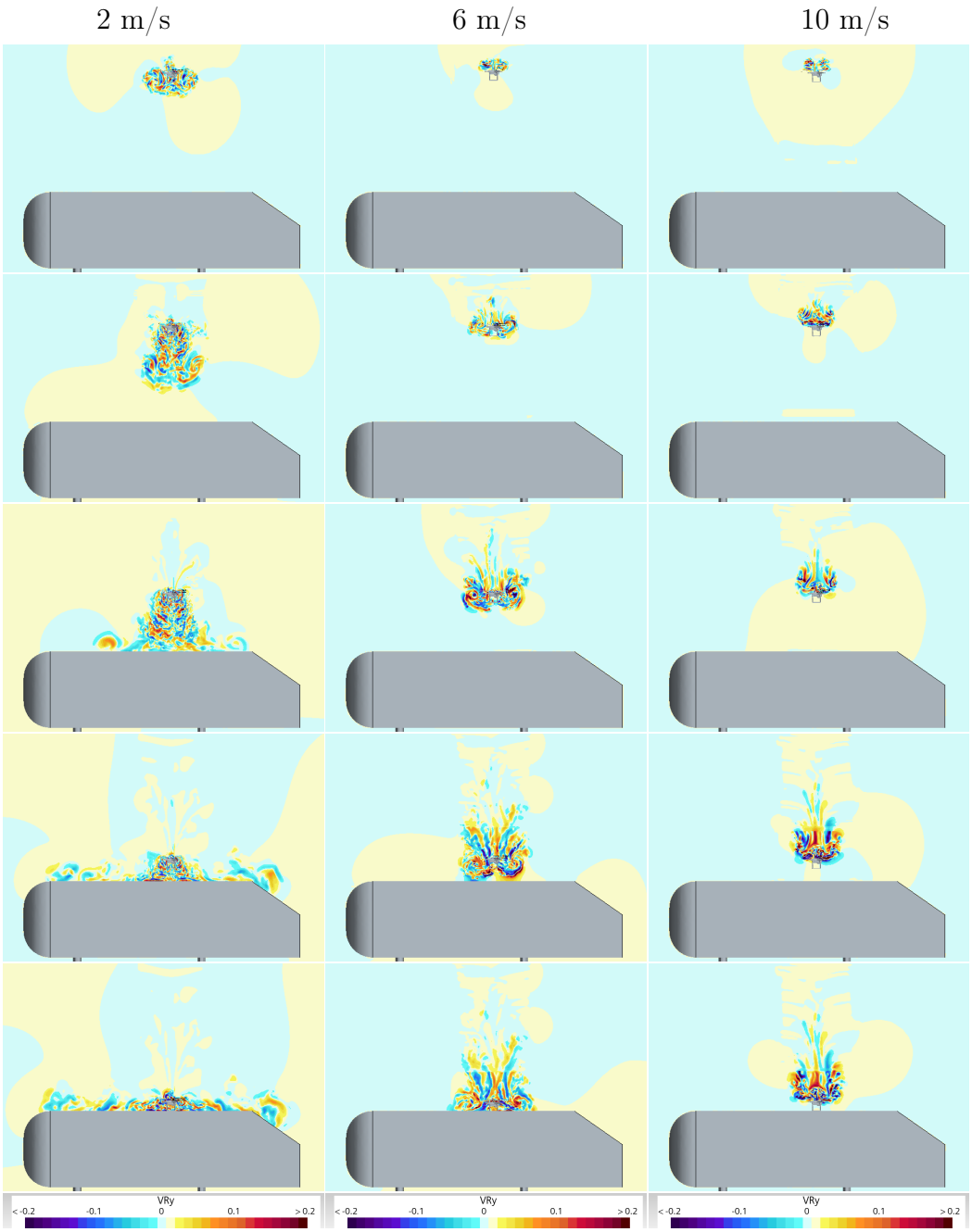

Figure 4.51: Comparison of V_y^* contours for descent velocities of 2, 6, and 10 m/s at nondimensional heights $h^* = 7.55$, 5.87, 3.36, 0.84, and 0.02 (arranged from top to bottom).

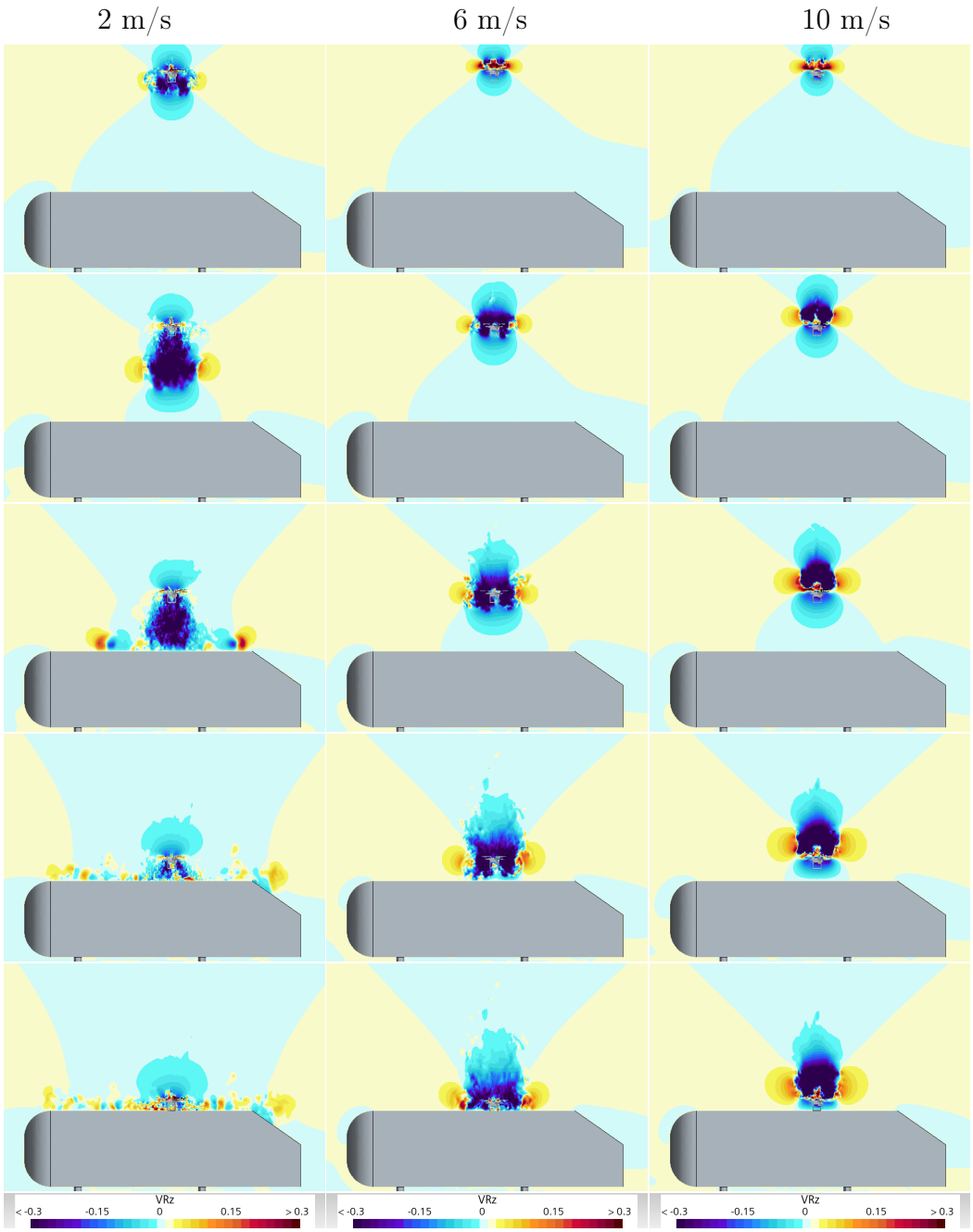

Figure 4.52: Comparison of V_z^* contours for descent velocities of 2, 6, and 10 m/s at nondimensional heights $h^* = 7.55$, 5.87, 3.36, 0.84, and 0.02 (arranged from top to bottom).

- At higher velocities ($v_d = 10\,\mathrm{m/s}$), all components (V_x, V_y, V_z) exhibit confined behavior with minimal dispersion due to rapid descent and high-energy wakes.
- At intermediate velocities ($v_d = 6\,\mathrm{m/s}$), moderate expansion occurs in all components, marking a balance between confinement and dispersion.
- At lower velocities ($v_d = 2\,\mathrm{m/s}$), significant dispersion is observed in all components, resulting in widespread aerodynamic effects across both lateral and vertical directions.

These findings emphasize that higher descent velocities result in concentrated and intense wake ground interactions near specific regions of the GV. In comparison, lower velocities promote greater dispersion and broader aerodynamic coupling across its surface.

The aerodynamic pressure field (C_p) demonstrates significant variations across all descent velocities, regardless of speed, highlighting its sensitivity to the influence of the ground. Unlike velocity components such as V_x, V_y, and V_z, which exhibit selective interactions depending on specific descent rates, C_p provides a consistent and robust measure of ground effects. This consistency arises because the pressure field is directly influenced by the proximity of the UAV to the ground vehicle (GV), capturing subtle changes in aerodynamic interactions as the separation distance decreases.

At lower descent velocities, the pressure field shows a more gradual response to ground effects, with smoother distributions across the GV surface. However, as descent velocity increases, the pressure field becomes more dynamic, with sharper gradients and localized regions of high and low pressure forming near the GV. These variations indicate stronger aerodynamic coupling between the UAV wake and the GV surface at higher speeds. The ability of C_p to consistently reflect these interactions makes it a critical parameter for evaluating fluid-structure interactions in ground-effect conditions.

The pressure field also plays a pivotal role in identifying transitional states of UAV operation, such as shifts between the NWS, VRS, and WBS. For example, at lower descent velocities, C_p distributions are relatively uniform, reflecting stable wake behavior. In contrast, higher velocities lead to more pronounced pressure fluctuations, signaling intensified wake-GV interactions and transitions into more dynamic operational states.

The Q-criteria and vorticity dynamics provide deeper insights into the wake behavior and its interaction with the GV surface under varying descent velocities as shown in Figure 4.54. At lower descent rates, vorticity fields tend to disperse over a broader area as they interact with the GV. This dispersion reflects weaker aerodynamic coupling, where wake structures lose coherence and spread laterally and vertically along the Ahmed body. The resulting flow patterns are characterized by diminished rotational energy and reduced aerodynamic impact on the GV.

In contrast, at higher descent velocities, vorticity fields remain concentrated and energetic as they propagate toward the GV surface. These fields maintain their coherence for longer distances, leading to stronger localized interactions with the GV. The Q-criteria analysis reveals that at these higher speeds, vortex structures form closer to the UAV and exhibit greater rotational strength. This behavior aligns with operational states such as WBS, where wake dynamics are dominated by high-energy interactions with both the UAV and the GV surface.

One notable phenomenon observed is that vortex structures begin to make direct contact with the GV surface earlier than at lower speeds. These interactions generate complex flow patterns on and around the GV, including ring-like vortices that form on its upper surface. Such structures are indicative of intensified aerodynamic coupling between UAV wakes and ground surfaces under high-speed conditions.

Additionally, as descent velocity increases, wake structures show reduced lateral and vertical expansion compared to lower speeds. This confinement results in concentrated

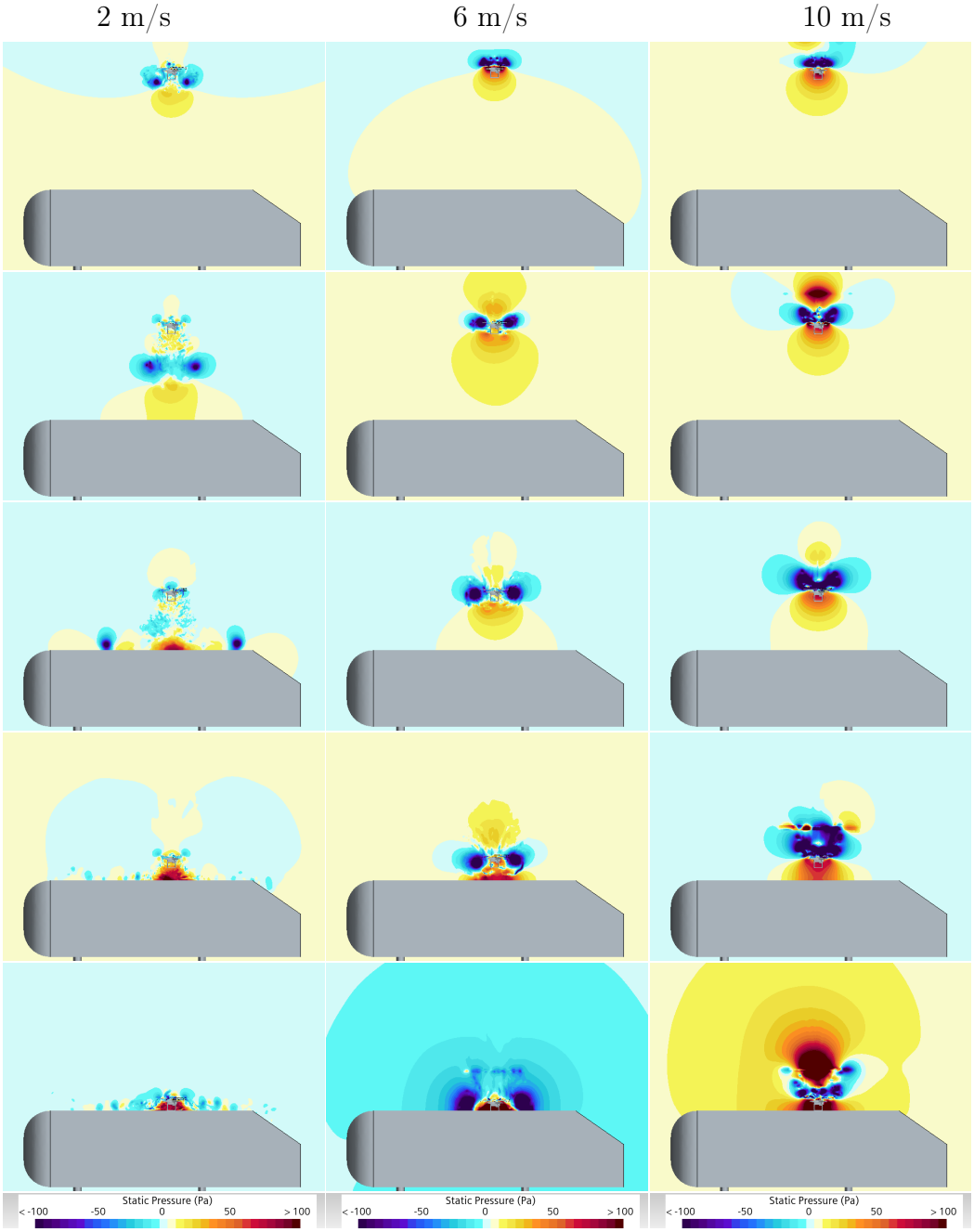

Figure 4.53: Comparison of C_p contours for descent velocities of 2, 6, and 10 m/s at nondimensional heights $h^* = 7.55$, 5.87, 3.36, 0.84, and 0.02 (arranged from top to bottom).

aerodynamic forces acting on specific regions of the GV rather than being distributed across its surface. These findings suggest that vorticity dynamics are highly sensitive to both descent velocity and proximity to the ground vehicle.

4.13 Influence of Descent Velocity on Headline Aerodynamic Coefficients

To comprehensively evaluate the selection of images of h^* at various spatial locations, a detailed analysis was conducted on several aerodynamic coefficients, including the yawing moment coefficient (C_{YM}), rolling moment coefficient (C_{RM}), pitching moment coefficient (C_{PM}), drag coefficient (C_D), and lift coefficient (C_L) at each discrete time step. These aerodynamic moment coefficients are fundamental in assessing the stability and control characteristics of UAVs, optimizing their aerodynamic performance, and improving the fidelity of advanced computational models.

The influence of vortex dynamics on aerodynamic forces and moments is particularly critical, as these vortices significantly affect the UAV's behavior during maneuvers. This interaction directly impacts the stability and control responses of the aircraft, underscoring the importance of understanding vortex-induced effects on aerodynamic parameters [39].

In the analysis, the drag coefficient (C_D) exhibited consistent oscillatory behavior across descent rates. At lower descent velocities of 2 m/s and 4 m/s, the oscillations remained relatively stable. However, at a descent velocity of 6 m/s, a pronounced peak in oscillation amplitude was observed, suggesting that the UAV entered a VRS at this speed. At higher descent velocities of 8 m/s and 10 m/s, significant oscillations persisted; however, they were less pronounced compared to those at 6 m/s due to the vortices being displaced further downstream.

Conversely, the lift coefficient (C_L) demonstrated minimal oscillatory changes under varying descent velocities. Nonetheless, as velocities increased, a notable reduction in lift was observed. This reduction can be attributed to the influence of vortex structures disrupting the aerodynamic flow over lifting surfaces. The precise mechanisms

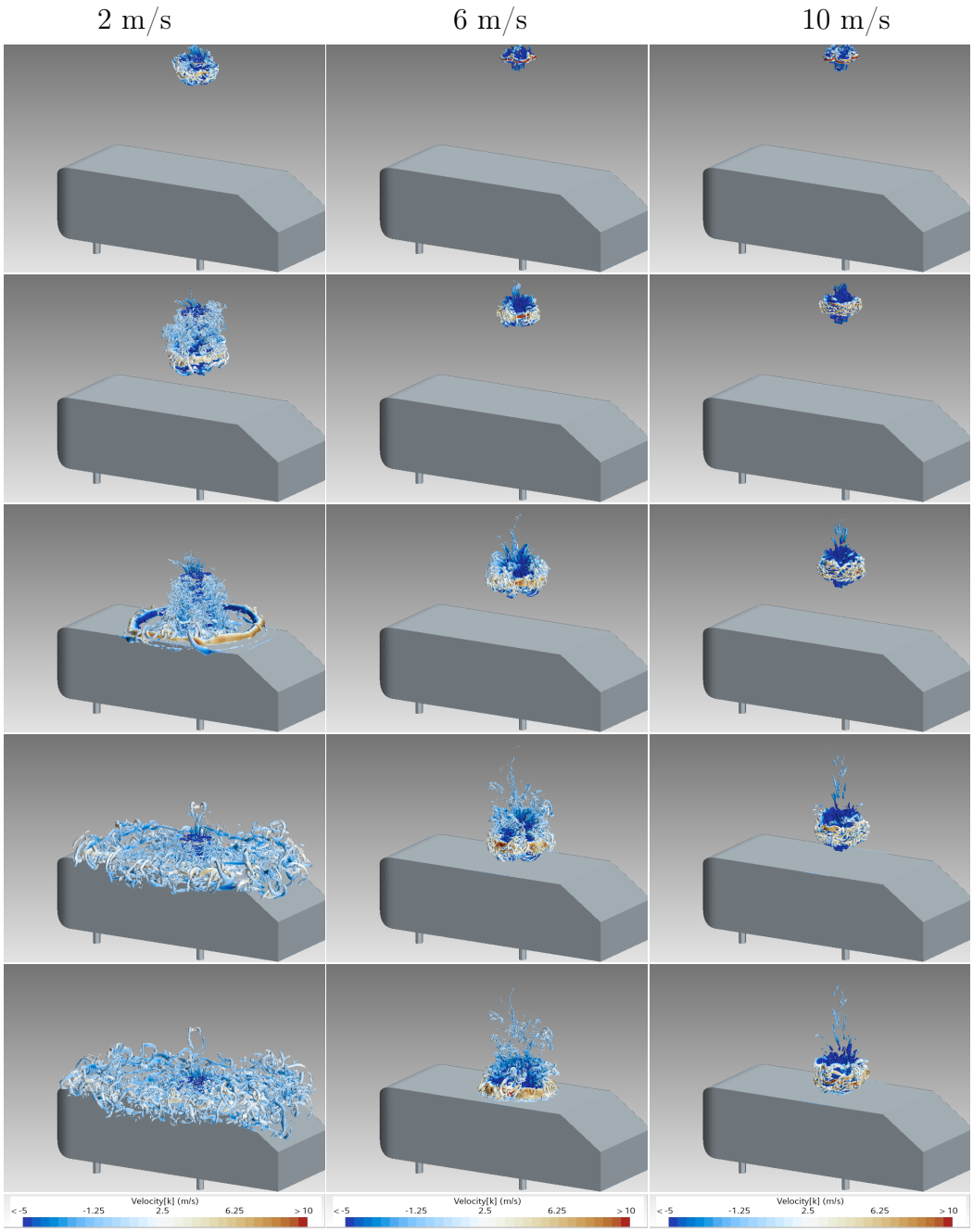

Figure 4.54: Comparison of isosurfaces of Q-criterion for descent velocities of 2, 6, and 10 m/s at nondimensional heights $h^* = 7.55$, 5.87, 3.36, 0.84, and 0.02 (arranged from top to bottom).

behind these changes will be further analyzed in subsequent sections to elucidate their relationship with vortex dynamics and their implications for UAV performance.

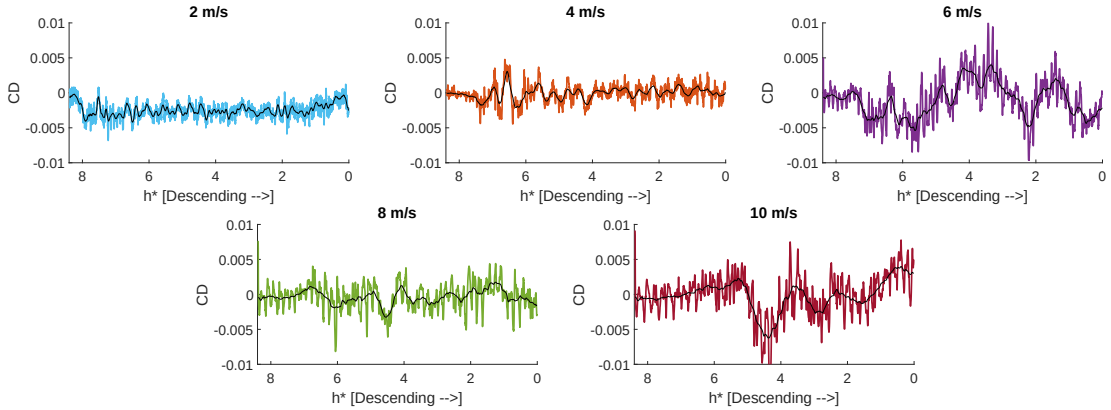

Figure 4.55: Variation of UAV drag coefficient (C_D) during landing on the GV for descent velocities (v_d) of 2, 4, 6, 8, and 10 m/s. Note that h^* decreases as the UAV approaches landing.

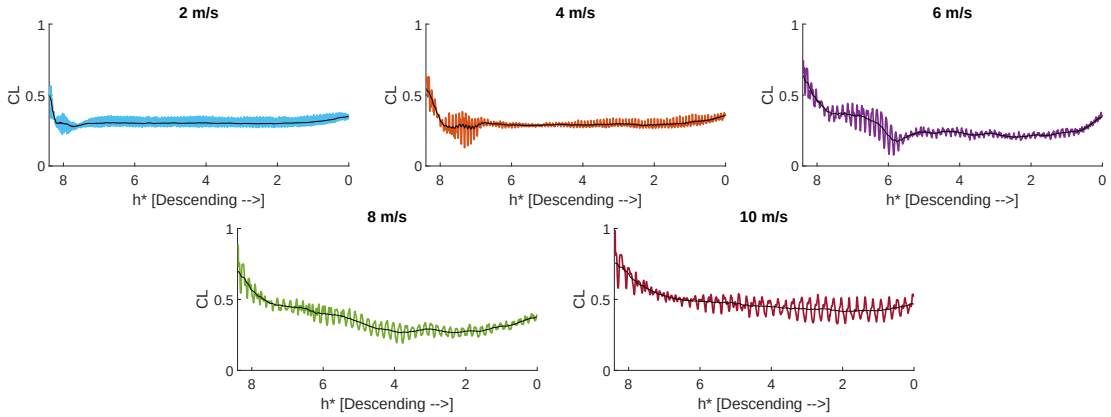

Figure 4.56: Variation of UAV Lift coefficient (C_L) during landing on the GV for descent velocities (v_d) of 2, 4, 6, 8, and 10 m/s. Note that h^* decreases as the UAV approaches landing.

The analysis of yawing moments in the UAV reveals that these moments play a pivotal role in influencing the deformation and displacement of the vortex ring structure. Such disturbances can disrupt the coherence of the vortex system, thereby impacting its ability to sustain a stable trajectory. Understanding these yawing moments, along with their associated instabilities, is crucial as they directly affect the aerodynamic force distribution, particularly drag and lift. These effects are essential for evaluating

the UAV's stability and control performance during various flight conditions.

From the analysis of the figures, it was observed that descent rates of 6 m/s, 8 m/s, and 10 m/s exhibited significant fluctuations in yawing moments. These fluctuations were more pronounced compared to descent rates of 2 m/s and 4 m/s, where oscillations occurred only intermittently-approximately one or two times throughout the simulation. The increased fluctuations at higher descent rates can be attributed to nonlinear aerodynamic phenomena such as VRS and wake interactions, which become more dominant as velocity increases.

Nonlinearity in aerodynamic responses are particularly evident in rotorcraft and multirotor UAVs during rapid descent maneuvers. At higher velocities, these nonlinear effects lead to greater variations in lift and control authority due to vortex-induced thrust losses and oscillatory behavior in vehicle attitude. Such dynamics are critical for understanding the stability challenges faced by UAVs during rapid descents, where interactions between wake structures and aerodynamic forces amplify instabilities. Further investigation into these phenomena will provide deeper insights into mitigating these effects and improving UAV performance under complex flight conditions.

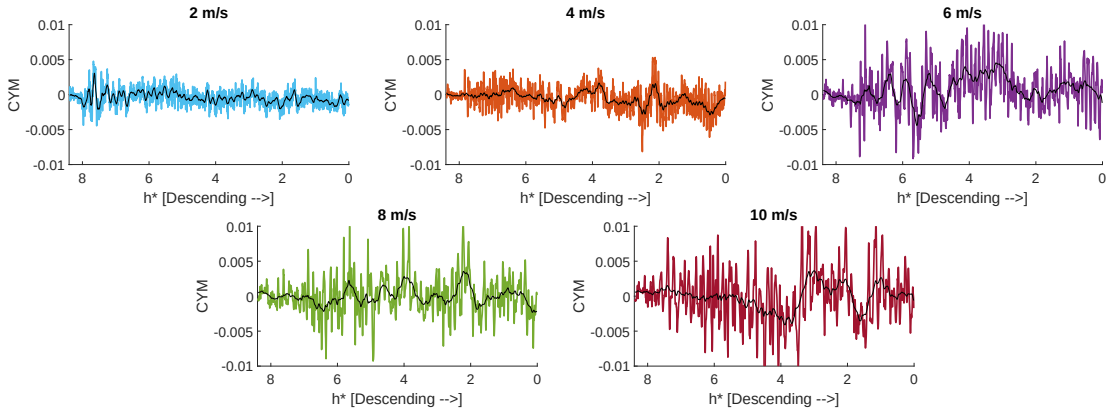

Figure 4.57: Variation of UAV yaw-moment coefficient (C_{YM}) during landing on the GV for descent velocities (v_d) of 2, 4, 6, 8, and 10 m/s. Note that h^* decreases as the UAV approaches landing.

The rolling moment of the UAV is intrinsically linked to the rolling moment coeffi-

cient, C_L, which arises from asymmetries in lift distribution or external aerodynamic forces, such as wind gusts. These asymmetries can significantly influence the UAV's flight dynamics by altering key parameters, including drag and descent rate. For instance, an imbalance in lift—where one propeller generates more lift than another—can reduce airspeed on one side of the UAV, thereby affecting its overall descent trajectory and stability.

An analysis of the rolling moment graphs indicates a relatively stable behavior across all five descent phases for most of the simulation duration. However, larger oscillations are observed toward the end of the simulation, particularly during the UAV's descent and approach to the GV. These oscillations are primarily attributed to the UAV's interaction with wake turbulence and vortices generated during its descent. As the UAV encounters these aerodynamic disturbances, it must actively stabilize itself to ensure a controlled and safe landing.

As shown in Figure 4.57, the magnitude of oscillations increases with higher descent speeds. This observation suggests that rapid descents pose greater challenges for maintaining stability, likely due to a reduction in coherent vortex production and increased aerodynamic disturbances. At higher velocities, the wake interactions become more pronounced such as 6 m/s, leading to amplified rolling moments as the UAV attempts to counteract these instabilities.

These findings highlight the critical role of rolling moments in UAV flight dynamics, particularly during descent and landing phases. Understanding how these moments evolve under varying conditions is essential for optimizing control strategies and improving UAV performance in complex aerodynamic environments. Future analyses will focus on quantifying these interactions in greater detail to develop robust stabilization mechanisms for UAVs operating under challenging flight scenarios. The pitching moment plots offer a comprehensive analysis of the dynamic pressure, angle of attack (AoA), and longitudinal static stability of the UAV during descent. The

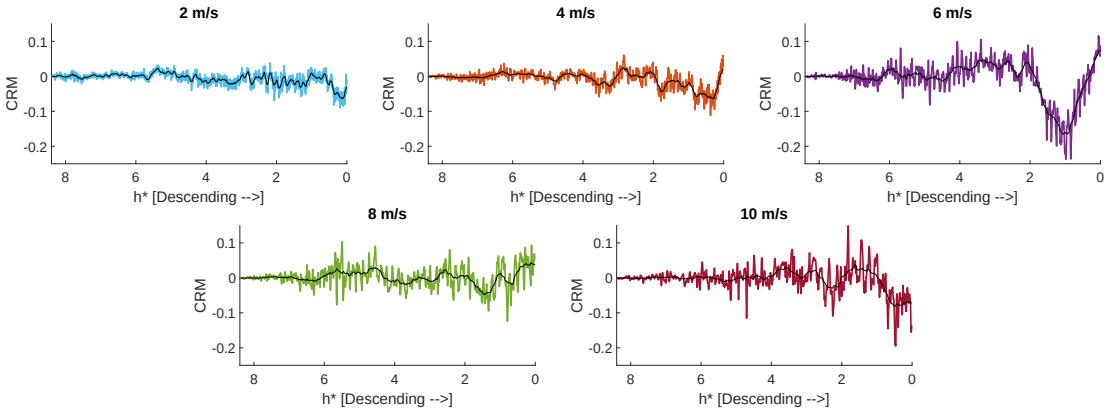

Figure 4.58: Variation of UAV rolling-moment coefficient (C_{RM}) during landing on the GV for descent velocities (v_d) of 2, 4, 6, 8, and 10 m/s. Note that h^* decreases as the UAV approaches landing.

pitching moment, which governs the UAV's rotational behavior about its lateral axis, is closely tied to the aerodynamic forces acting on the vehicle. These forces are influenced by the descent velocity, airflow conditions, and external disturbances.

The relationship between descent rate and pitching moment stability is evident in the data across various descent phases. As descent velocity increases, the pitching moment coefficient (C_{PM}) tends to stabilize more quickly but remains closer to zero for shorter durations compared to lower descent rates. For instance, at a descent rate of 2 m/s, C_{PM} begins to increase steadily around $h^* = 3.36$, indicating a gradual buildup of instability as the UAV adjusts its attitude. In contrast, at a higher descent rate of 10 m/s, significant oscillations are observed around $h^* = 5.034$, reflecting the challenges posed by rapid descents where wake interactions and vortex dynamics are more pronounced.

Future investigations will focus on quantifying these effects in greater detail by analyzing the temporal evolution of pitching moments and their relationship with other aerodynamic coefficients such as drag (C_D), lift (C_L), lyaw momemt (C_{YM}), and rolling moment (C_{RM}). These analyses will involve a deeper exploration of scalar plots and time-series data to identify trends and correlations that contribute to pitch instabilities. For instance, scalar scenes depicting pressure distribution, vorticity

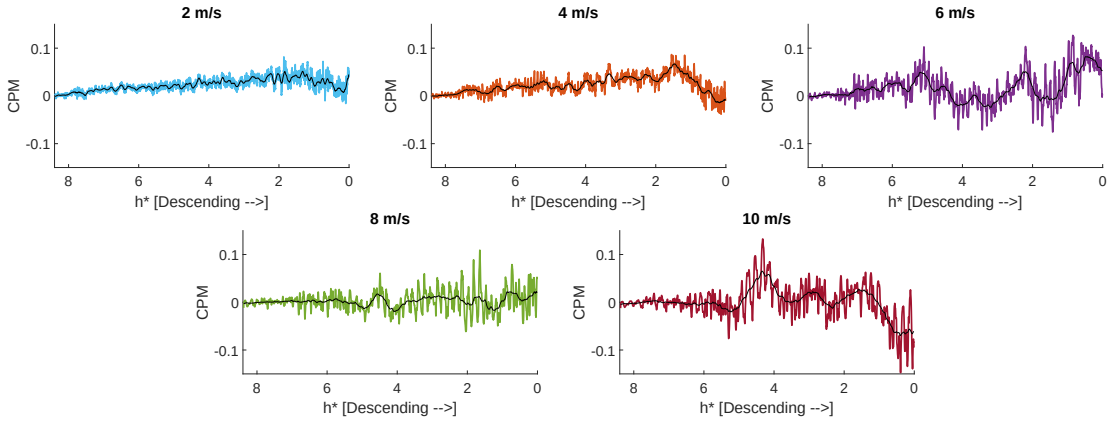

Figure 4.59: Variation of UAV pitch-moment coefficient (C_{PM}) during landing on the GV for descent velocities (v_d) of 2, 4, 6, 8, and 10 m/s. Note that h^* decreases as the UAV approaches landing.

magnitude, and Q-criteria at different non-dimensional heights (h^*) will be examined to provide further insights into how wake structures influence longitudinal stability. Additionally, advanced post-processing techniques, such as Proper Orthogonal Decomposition (POD) or Dynamic Mode Decomposition (DMD), may be employed to extract dominant flow features that impact pitching moments.

Another critical aspect of future work will involve exploring advanced control methodologies designed to enhance UAV performance during complex maneuvers. By integrating insights gained from detailed aerodynamic analyses, control strategies such as model predictive control (MPC) or adaptive neural networks can be developed to dynamically adjust UAV inputs in response to changing flight conditions. These methods will aim to counteract destabilizing effects caused by wake interactions or VRS onset, particularly at higher descent velocities.

CHAPTER 5: CONCLUSIONS

The primary objective of this study was to simulate and analyze the descent of an unmanned aerial vehicle (UAV) onto a ground vehicle (GV) at five distinct descent velocities: 2, 4, 6, 8, and 10 m/s. This research builds upon prior studies of UAV interactions with wake and flow fields around an Ahmed body by providing a comprehensive investigation into wake dynamics and their relationship to the vortex ring state (VRS). The study aimed to deepen the understanding of the aerodynamic phenomena occurring during UAV descents, with particular emphasis on identifying the onset and progression of VRS. To achieve these objectives, simulations were conducted using the Improved Delayed Detached Eddy Simulation (IDDES) turbulence model solver in conjunction with an Adaptive Mesh Refinement (AMR) scheme. This approach enabled high-resolution modeling of complex flow structures while maintaining computational efficiency. The computational domain consisted of between 63 and 95 million cells for all simulations, ensuring sufficient resolution to capture intricate wake dynamics. Post-processing techniques were employed to extract critical insights, including the generation of scalar scenes to visualize key flow parameters at various non-dimensional height values (h^*), providing a detailed representation of wake behavior and vortical structures at each descent velocity.

The analysis yielded significant findings regarding the aerodynamic behavior of UAVs during descent at varying speeds. At a descent velocity of 2 m/s, the UAV exhibited stable aerodynamic behavior with minimal wake interference and no evidence of vortex ring state formation. At 6 m/s, the simulations revealed clear indications of VRS onset, characterized by increased turbulence and wake recirculation near the rotor region. At 10 m/s, the UAV transitioned into a windmill-brake state, marked by

substantial wake disruption and aerodynamic instability. Scalar scenes and aerodynamic coefficients were analyzed to ensure consistency and accuracy in representing these results. Key coefficients included the lateral force coefficient (C_{YM}), rolling moment coefficient (C_{RM}), pitching moment coefficient (C_{PM}), drag coefficient (C_D), and lift coefficient (C_L). These metrics provided quantitative validation for observed flow patterns and aerodynamic instabilities. The findings underscore the relationship between vortical structures and pitch instabilities across varying descent velocities, offering valuable insights into UAV performance under different aerodynamic conditions.

While this study provided valuable contributions to understanding UAV descent dynamics, several limitations were identified. First, the simulations were limited to specific descent speeds (2, 4, 6, 8, and 10 m/s), without exploring intermediate or finer variations in velocity that could provide a more detailed understanding of transitional states. Second, the high-fidelity nature of the IDDES model combined with AMR resulted in significant computational demands, which restricted the scope for broader parametric studies. Finally, external influences such as crosswinds or real-world environmental conditions were not considered in this analysis. These factors could significantly impact UAV wake dynamics and stability in practical applications.

Future research will aim to address these limitations by focusing on several key areas. Conducting simulations with finer increments in descent speed will allow for a more detailed exploration of transitional states near VRS onset. Including external conditions such as crosswinds or turbulence will enhance the realism of simulations and provide insights into real world UAV operations. Expanding the scope to include variations in rotor configurations or UAV geometries could yield broader applicability for different UAV designs. Additionally, simulations closer to conditions where VRS is fully developed will help uncover additional characteristics of this phenomenon, improving understanding of its implications for UAV stability. These advancements

aim to improve the precision and safety of UAV maneuvers near ground vehicles, particularly in applications requiring close-proximity operations. The findings have potential implications for both civilian applications such as delivery systems and military operations involving autonomous aerial platforms.

REFERENCES

[1] G. Hoffmann, H. Huang, S. Waslander, and C. Tomlin, "Quadrotor helicopter flight dynamics and control: Theory and experiment," in *AIAA guidance, navigation and control conference and exhibit*, p. 6461, 2007.

[2] M. Bangura, R. Mahony, *et al.*, "Nonlinear dynamic modeling for high performance control of a quadrotor," in *Australasian conference on robotics and automation*, pp. 1–10, 2012.

[3] S. Skove, "Army puts drones front and center in unfunded wishlist," Mar 2024. Defense One `https://www.defenseone.com/technology/2024/03/army-puts-drones-front-and-center-newly-obtained-budget-docs/395182/`[Accessed: December 5, 2024].

[4] G. D. Padfield, *Helicopter flight dynamics: the theory and application of flying qualities and simulation modelling*. John Wiley & Sons, 2008.

[5] H. Van Vyve, P. Chatelain, and G. Winckelmans, *Simulation of a helicopter in vortex ring state through a coupled simulation of multi-body dynamics and aerodynamics*. PhD thesis, UCL-Ecole Polytech Louvain, Belgium, 2019.

[6] A. Talaeizadeh, D. Antunes, H. N. Pishkenari, and A. Alasty, "Optimal-time quadcopter descent trajectories avoiding the vortex ring and autorotation states," *Mechatronics*, vol. 68, p. 102362, 2020.

[7] G. Whale, "Army goes green with FED Alpha," 2013. MotorTrend `https://https://www.motortrend.com/news/163-news0603-fed-alpha/` [Accessed: December 5, 2024].

[8] S. R. Ahmed, G. Ramm, and G. Faltin, "Some salient features of the time-averaged ground vehicle wake," *SAE transactions*, pp. 473–503, 1984.

[9] J. S. Lee, S. J. Park, J. H. Lee, B. M. Weon, K. Fezzaa, and J. H. Je, "Origin and dynamics of vortex rings in drop splashing," *Nature communications*, vol. 6, no. 1, p. 8187, 2015.

[10] M. Colborn, "Airman vortex ring state part 1."

[11] P. Mullen and G. Bernini, "Vortex ring state prediction and analysis," 2016. Available online: `https://dspace-erf.nlr.nl/server/api/core/bitstreams/af36d551-a634-4788-bd3d-d0144fdc44c0/content` (accessed on 24 November 2024).

[12] W. Johnson, "Model for vortex ring state influence on rotorcraft flight dynamics," tech. rep., NASA/TP-2005-213477, 2005.

[13] J. G. Leishman, M. J. Bhagwat, and S. Ananthan, "The vortex ring state as a spatially and temporally developing wake instability," *Journal of the American Helicopter Society*, vol. 49, no. 2, pp. 160–175, 2004.

[14] J. McQuaid, A. Kolaei, G. Bramesfeld, and P. Walsh, "Early onset prediction for rotors in vortex ring state," *Journal of Aerospace Engineering*, vol. 33, no. 6, p. 04020081, 2020.

[15] V. Rimsa and M. Liugas, "Numerical investigation of the vortex ring phenomena in rotorcraft," *Aerospace*, vol. 11, no. 6, 2024.

[16] J. Wang, R. Chen, J. Lu, and Y. Zhao, "Numerical simulation of the quadcopter flow field in the vertical descent state," *Proceedings of the Institution of Mechanical Engineers, Part G: Journal of Aerospace Engineering*, vol. 236, no. 14, pp. 3019–3031, 2022.

[17] G. Throneberry, A. Takeshita, C. Hocut, F. Shu, and A. Abdelkefi, "Multi-rotor wake characterization and visualization in ascending and descending flight," *Experiments in Fluids*, vol. 63, no. 6, p. 98, 2022.

[18] J. Sun, X. Zhou, T. Ban, J. Zhao, and F. Shuang, "Energy consumption modelling of coaxial-rotor in vortex ring state for controllable high-speed descending," in *2024 IEEE International Conference on Robotics and Automation (ICRA)*, pp. 3803–3809, 2024.

[19] M. Marshall, E. Tang, J. Cornelius, F. Ruiz, and S. Schmitz, "Performance of the dragonfly lander's coaxial rotor in vortex ring state," in *AIAA Scitech 2024 Forum*, p. 0247, 2024.

[20] J. K. Cornelius, S. Schmitz, and M. P. Kinzel, "Efficient computational fluid dynamics approach for coaxial rotor simulations in hover," *Journal of aircraft*, vol. 58, no. 1, pp. 197–202, 2021.

[21] J. Cornelius, S. Schmitz, J. Palacios, B. Juliano, and R. Heisler, "Rotor performance predictions for urban air mobility: Single vs. coaxial rigid rotors," *Aerospace*, vol. 11, no. 3, p. 244, 2024.

[22] C. Paz, E. Suárez, C. Gil, and J. Vence, "Assessment of the methodology for the cfd simulation of the flight of a quadcopter uav," *Journal of Wind Engineering and Industrial Aerodynamics*, vol. 218, p. 104776, 2021.

[23] C. Paz, E. Suárez, C. Gil, and C. Baker, "Cfd analysis of the aerodynamic effects on the stability of the flight of a quadcopter uav in the proximity of walls and ground," *Journal of Wind Engineering and Industrial Aerodynamics*, vol. 206, p. 104378, 2020.

[24] E. Yilmaz and J. Hu, "Cfd study of quadcopter aerodynamics at static thrust conditions," in *Proceedings of the ASEE Northeast 2018 annual conference, West Hartford, CT, USA*, pp. 27–28, 2018.

[25] W. P. Timms, "Aerodynamics of uav ground effect interactions," Master's thesis, University of North Carolina at Charlotte, U.S.A., 2021.

[26] K. Liu, B. Zhang, Y. Zhang, and Y. Zhou, "Flow structure around a low-drag ahmed body," *Journal of Fluid Mechanics*, vol. 913, p. A21, 2021.

[27] I. Bayraktar, D. Landman, and O. Baysal, "Experimental and computational investigation of ahmed body for ground vehicle aerodynamics," *SAE transactions*, pp. 321–331, 2001.

[28] E. Guilmineau, G. Deng, A. Leroyer, P. Queutey, M. Visonneau, and J. Wackers, "Assessment of hybrid rans-les formulations for flow simulation around the ahmed body," *Computers & Fluids*, vol. 176, pp. 302–319, 2018.

[29] M. Uddin, S. Nichols, C. Hahn, A. Misar, S. Desai, N. Tison, and V. Korivi, "Aerodynamics of landing maneuvering of an unmanned aerial vehicle in close proximity to a ground vehicle," *SAE International Journal of Advances and Current Practices in Mobility*, vol. 5, no. 2023-01-0118, pp. 2029–2046, 2023.

[30] W. Zhou, Z. Ning, H. Li, and H. Hu, "An experimental investigation on rotor-to-rotor interactions of small uav propellers," in *35th AIAA applied aerodynamics conference*, p. 3744, 2017.

[31] F. R. Menter, "Two-equation eddy-viscosity turbulence models for engineering applications," *AIAA journal*, vol. 32, no. 8, pp. 1598–1605, 1994.

[32] F. Menter, "Stress-blended eddy simulation (sbes)-a new paradigm in hybrid rans-les modeling," in *Progress in Hybrid RANS-LES Modelling: Papers Contributed to the 6th Symposium on Hybrid RANS-LES Methods, 26-28 September 2016, Strasbourg, France 6*, pp. 27–37, Springer, 2018.

[33] D. C. Wilcox, "Reassessment of the scale-determining equation for advanced turbulence models," *AIAA journal*, vol. 26, no. 11, pp. 1299–1310, 1988.

[34] D. C. Wilcox, "Formulation of the kw turbulence model revisited," *AIAA journal*, vol. 46, no. 11, pp. 2823–2838, 2008.

[35] B. E. Launder and B. I. Sharma, "Application of the energy-dissipation model of turbulence to the calculation of flow near a spinning disc," *Letters in heat and mass transfer*, vol. 1, no. 2, pp. 131–137, 1974.

[36] M. L. Shur, P. R. Spalart, M. K. Strelets, and A. K. Travin, "A hybrid rans-les approach with delayed-des and wall-modelled les capabilities," *International journal of heat and fluid flow*, vol. 29, no. 6, pp. 1638–1649, 2008.

[37] C. P. Bounds, S. Rajasekar, and M. Uddin, "Development of a numerical investigation framework for ground vehicle platooning," *Fluids*, vol. 6, no. 11, 2021.

[38] A. R. Schenk, *Computational Investigation of the Effects of Rotor-on-Rotor Interactions on Thrust and Noise*. Brigham Young University, 2020.

[39] W. F. Phillips, *Mechanics of flight*. John Wiley & Sons, 2004.